3-11-2011

Characterization of Neutron-Induced Defects in Isotopically Enriched Lithium Tetraborate

Brant E. Kananen

Recommended Citation

Kananen, Brant E., "Characterization of Neutron-Induced Defects in Isotopically Enriched Lithium Tetraborate" (2011). *Theses and Dissertations*. 1460.
https://scholar.afit.edu/etd/1460

CHARACTERIZATION OF NEUTRON-INDUCED DEFECTS IN ISOTOPICALLY ENRICHED LITHIUM TETRABORATE

THESIS

Brant E. Kananen, Major, USA

AFIT/GNE/ENP/11-M12

DEPARTMENT OF THE AIR FORCE
AIR UNIVERSITY

AIR FORCE INSTITUTE OF TECHNOLOGY

Wright-Patterson Air Force Base, Ohio

APPROVED FOR PUBLIC RELEASE; DISTRIBUTION UNLIMITED.

AFIT/GNE/ENP/11-M12

CHARACTERIZATION OF NEUTRON-INDUCED DEFECTS IN ISOTOPICALLY ENRICHED LITHIUM TETRABORATE

THESIS

Presented to the Faculty
Department of Engineering Physics
Graduate School of Engineering and Management
Air Force Institute of Technology
Air University
Air Education and Training Command
In Partial Fulfillment of the Requirements for the
Degree of Master of Science in Nuclear Science

Brant E. Kananen, BS
Major, USA

March 2011

APPROVED FOR PUBLIC RELEASE; DISTRIBUTION UNLIMITED.

AFIT/GNE/ENP/11-M12

CHARACTERIZATION OF NEUTRON-INDUCED DEFECTS IN ISOTOPICALLY ENRICHED LITHIUM TETRABORATE

Brant E. Kananen, BS
Major, USA

Approved:

LTC John McClory (Chairman) Date

Nancy Giles, PhD (Member) Date

Robert Hengehold, PhD (Member) Date

AFIT/GNE/ENP/11-M12

Abstract

Lithium tetraborate ($Li_2B_4O_7$) is assessed for use as a material for neutron detection. $Li_2B_4O_7$ isotopically enriched in either ^{6}Li or ^{10}B provides a medium that efficiently captures and transmutes neutrons into more readily detected forms of material or energy. Neutron detection is desirable to detect elicit movement of special nuclear material or nuclear weapons. Single crystals of $Li_2B_4O_7$, ^{6}Li or ^{10}B enriched, were neutron irradiated, and electron paramagnetic resonance was used to detect point defects induced by the neutrons. Multiple defects were noted in the irradiated crystals. Two particular defects, perturbed lithium vacancies and lithium clusters are proposed as induced by thermal neutrons. Parallel experiments on silver doped $Li_2B_4O_7$ indicated that fast neutrons induce interstitial defects including interstitial oxygen, lithium, and silver atoms in Ag doped crystals. Electron paramagnetic resonance, electron-nuclear double resonance, pulsed anneal, and thermoluminescence studies prior to neutron irradiation concluded that Ag doped $Li_2B_4O_7$ crystals contain Ag point defects that trap both electrons and holes. Pulsed anneal and thermoluminescence studies of all crystal types prior to neutron irradiation suggest neutron induced defects are significantly more stable than as-grown defects. Thermoluminescence may be a viable technique to detect neutron interactions in the crystals. Lastly, 511 keV gamma radiation observed after neutron irradiation of all crystals is attributed to positron annihilation in the crystals. The ^{6}Li(^{7}Li,2n)^{11}C reaction is suggested as the responsible mechanism for positron production. The resulting ^{11}C nucleus radio actively decays via emission of a positron with a half life of 20.39 minutes.

Acknowledgements

I would like to acknowledge my family for their significant support throughout this process. I would like to thank my advisor, LTC John McClory, for his assistance and advice. Additionally, I would like to thank Mr. Joe Talnagi of the Ohio State University (Columbus, OH), and Mr. Adam Brant and Dr. Larry Halliburton, of West Virginia University (Morgantown, WV), who all helped me greatly with the experimental techniques and concepts. Data referenced as personal communication from M.J. Swinney was obtained from Mr. Swinney in March, 2010. He obtained the data during work at the Air Force Institute of Technology (Dayton, OH).

Brant E. Kananen

Table of Contents

Page

List of Figures

Figure Page

List of Tables

Table Page

CHARACTERIZATION OF NEUTRON-INDUCED DEFECTS IN ISOTOPICALLY ENRICHED LITHIUM TETRABORATE

I. Introduction

1.1 Purpose

The post-cold-war emergence of asymmetric threats has heightened the need for reliable detection of Special Nuclear Materials (SNM) as a means of detecting proliferation activities and potential nuclear/radiological threats. Furthermore, ascendancy of the global economy in this unstable environment has left industrialized nations at risk of attack via the shipping containers and cargo vessels critical to prosperity. The magnitude of the task of monitoring all cargo containers for special nuclear material at sea, land, and air ports of entry is a task of staggering proportions that demands a reliable, inexpensive method to detect potential threats. Exacerbating the magnitude of the detection task, the time available to detect SNM in a port facility is on the order of hours to days. Monitoring emissions of SNM from any significant percentage of the total number of cargo containers is exceedingly difficult on such a short time-line. In contrast to the relatively short period of time cargo containers remain in port, they remain in transit for times on the order of days to weeks. Leveraging this longer time to detect SNM enroute to an entry port gives time to integrate relatively low intensity signals from the SNM. Furthermore, detection/interdiction of special nuclear materials prior to reaching ports of entry could provide a significant geographic buffer between populated areas and any detonation event.

Detection of special nuclear materials can be accomplished via several methods. Radioactive decay and spontaneous fission processes in special nuclear materials leave distinct signatures in their immediate environment. Some of these signatures such as alpha, beta, gamma, and x-ray radiations are easily shielded. Appropriate shielding can make the detection of these signatures impractical as a detection method. On the other hand, neutron radiation is not as easily shielded, and can be used as a signature of these controlled materials. Neutrons are relatively uncommon in the natural environment which should result in improved signal to noise in comparison to other detectable signals.

The drive to detect small quantities of the neutron by-products of fission motivates the exploration of boron and lithium containing compounds such as lithium tetraborate ($Li_2B_4O_7$). In addition to containing Li-6 and B-10, compounds with relatively high probabilities of neutron interaction, $Li_2B_4O_7$ in single crystal form may provide a medium in which to time integrate neutron induced defects. Potential signal integration over time leverages the time available in route to port to detect SNM. In addition, the thermoluminescent (TL) and optical properties of $Li_2B_4O_7$ may provide inexpensive methods of assessing the number of neutron interactions in a single crystal sample. Any inexpensive, ready method of assessing neutron interactions would yield a lower cost detector in turn facilitating fielding detectors in greater numbers.

1.2 Research Goals

The primary goal of this research was to characterize point defects in as-grown isotopically enriched $Li_2B_4O_7$ crystals, and compare those defects with defects induced by neutron interactions. This comparison was intended to demonstrate that defects induced by neutron interactions are unique and constitute definitive proof of neutron absorption within the crystal volume. In addition to defect characterization, thermal stability determination of various charge traps associated with defects was a secondary goal of this research. TL was used to determine the thermal stability of charge traps related to both as-grown and neutron induced defects. If neutron induced trap sites are particularly stable or unstable, they may be distinguishable from other as-grown trap sites.

A tertiary goal of this research was to characterize as-grown point defects in silver doped $Li_2B_4O_7$ ($Li_2B_4O_7$:Ag), and to suggest recombination mechanisms based on the thermal stability of charge traps associated with those defects. As an aside to this tertiary goal, the relative anisotropic nature of as-grown defects in $Li_2B_4O_7$:Ag was evaluated in order to determine the associated spin Hamiltonian parameters. The author gathered the required data to determine the spin Hamiltonian parameters in conjunction with Dr. Larry Halliburton and Mr. Adam Brant of West Virginia University. However, calculation of the spin Hamiltonian parameters was the work of Dr. Halliburton and Mr. Brant, not the author. The work associated with the tertiary goal is being prepared for publication in the Journal of Applied Physics.

A fourth goal which developed during the course of this research was to characterize the mechanism responsible for production of 511 keV gamma radiations emanating from neutron irradiated $Li_2B_4O_7$. 511 keV gamma radiations are normally indicative of positron annihilation, and are unique signals not observed prior to neutron irradiation. Characterization of the responsible mechanism was undertaken as another possible method of definitively demonstrating neutron interaction in the crystal volume. Characterization included studies of the half-life of the radioactive nuclide responsible for the annihilating positrons, as well as a modified activity analysis to determine the mechanism responsible for radio-nuclide production and the efficiency of the responsible mechanism.

Neutrons are expected to produce defects in $Li_2B_4O_7$ crystals through three basics mechanisms. First, fast neutrons make produced interstitial defects through knock-on damage. These defects would most likely be neutrally charged atoms. Second, thermal neutrons may induce Li or B vacancies in the crystals through the ^{6}Li,n and ^{10}B,n reactions. Lastly, ^{3}H or ^{4}He products of the ^{6}Li,n and ^{10}B,n reactions may become trapped in the crystals. Thermal stability of these defects is not anticipated. If unique neutron induced defects can be detected, their thermal stability might be very similar to as-grown defects, or they may be unique.

Ag is expected to substitute for Li in the $Li_2B_4O_7$ crystal lattice. Ag has common oxidation states of 0, +1 and +2. Substituting for Li^{1+}, Ag should be present in the crystal in the +1 oxidation state. Therefore, Ag could readily trap both electrons and holes. The thermal stability of as-grown Ag related defects is expected to be greater than that of defects in undoped crystals. Neutron interaction in the $Li_2B_4O_7$:Ag crystals is expected to produce the same types of defects as in crystals without doping.

The number of isotopes in $Li_2B_4O_7$ is few. Therefore, the number of nuclear reactions for production of short lived positron emitting isotopes is also small. There is likely a nuclear reaction involving some combination of the naturally occurring isotopes of Li, B, and O, and the reaction products of the ^{6}Li,n or ^{10}B,n reactions that will yield a short lived positron emitter. Evaluation of the decay half life of the positron emitting isotope should identify the decaying isotope, and yield the reaction responsible for its production.

II. Theory

2.1 General

$Li_2B_4O_7$ is a tetragonal crystal in the space group $I4_{1cd}$ (Adamiv 2009, 870). Being tetragonal, $Li_2B_4O_7$ is axially symmetric, or the [100] and [010] directions show crystallographic equivalence. The [001] direction is unique, and the simplest direction regarding crystal orientation. Due to the axial symmetry, the [110] direction also shows unique crystal symmetry.

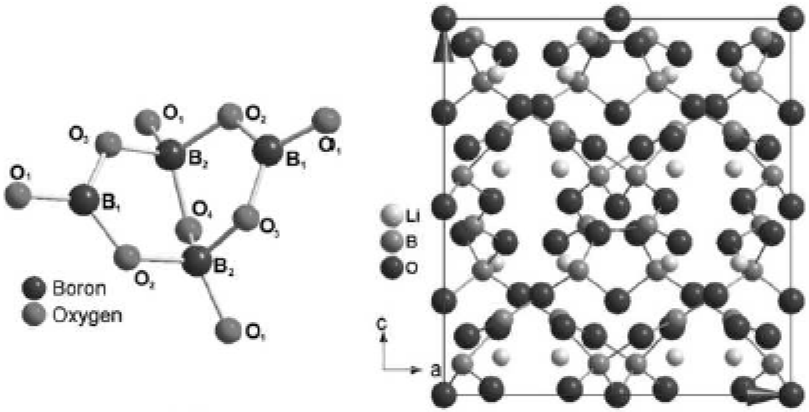

Figure 1. Basic B_4O_9 structural unit of $Li_2B_4O_7$ (left); orientation of B_4O_9 structural units and Li^+ ions in the crystal lattice (right) (M. Swinney 2009).

Like the high symmetry directions, the (100) plane and the (010) plane are equivalent, and high symmetry planes. The (001) plane is also a high symmetry plane. Figure 1 shows the basic building block of the $Li_2B_4O_7$ crystal, the B_4O_9 unit. Two of the O_1 atoms in the B_4O_9 structural unit belong to adjacent $Li_2B_4O_7$ molecule units. The crystals used in this study were grown by the Czochralski technique at the Institute of Physical Optics (L'viv, Ukraine) (M. W. Swinney et al. 2010, 2).

All Li^+ ions hold equivalent positions within the crystal. However, under an applied magnetic field, not all Li^+ ions sites are energetically equivalent depending on the orientation of the magnetic field vector and the crystallographic axis. Under rotation, all Li^+ ion sites are equivalent even in an applied magnetic field. Figure 2 shows the Li^+ ion within the molecule.

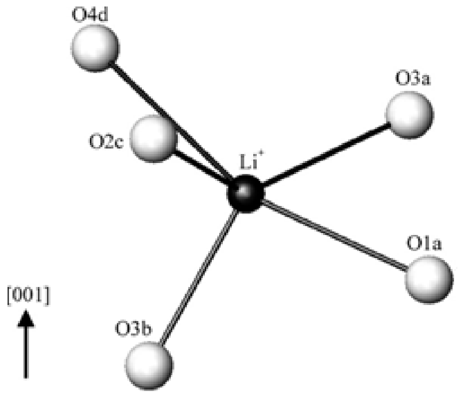

Figure 2. The orientation of the Li^+ ion reference nearest neighbor oxygen atoms in the $Li_2B_4O_7$ crystal (Adamiv 2009, 872).

Note that all O^{2-} ions have a nearest neighbor Li^+ ion, and the O in position three, reference Figure 2, has two nearest neighbor Li^+ ions. The Li^+ ions provide charge compensation within the crystal for the O^{2-} ions. In the event of O^{2-} vacancies in the as-grown crystal, two Li^+ vacancies must be present to compensate charge. Furthermore, most metal ion impurities or dopants will occupy interstitial sites or substitute for Li^+ ions (M. W. Swinney et al. 2010, 1)

2.2 Neutron Detection

Lithium and boron can be used to transmute neutrons into a more readily detectable particle or energy. Upon absorbing a thermal neutron, ^{6}Li undergoes the reaction,

$$ {}^{6}_{3}Li + {}^{1}_{0}n \rightarrow {}^{3}_{1}H + {}^{4}_{2}\alpha + 4.78MeV. \tag{1} $$

^{10}B undergoes a similar nuclear reaction,

$$ \begin{gathered} {}^{10}_{5}B + {}^{0}_{1}n \rightarrow {}^{7}_{3}Li + {}^{4}_{2}\alpha + 2.8MeV \\ {}^{10}_{5}B + {}^{0}_{1}n \rightarrow {}^{7}_{3}Li* + {}^{4}_{2}\alpha + 2.3MeV. \end{gathered} \tag{2} $$

^{6}Li is 7.5% abundant in nature and ^{10}B is 19.9% abundant in nature (Parrington 1996, 18). $Li_2B_4O_7$ contains both ^{6}Li and ^{10}B in natural abundances unless deliberately enriched. In addition to the direct reactions, ^{6}Li or ^{7}Li and ^{16}O can transmute neutrons indirectly in the $Li_2B_4O_7$ lattice as follows,

$$\begin{aligned} &{}^{6}Li\left(n,\alpha\right){}^{3}H \rightarrow {}^{16}O\left({}^{3}H,n\right){}^{18}F + 1.26MeV \rightarrow {}^{18}F\left(\beta^{+}\right){}^{18}O \\ &{}^{6}Li\left({}^{7}Li,2n\right){}^{11}C + 2.199MeV \rightarrow {}^{11}C\left(\beta^{+}\right){}^{11}B \end{aligned} \tag{3}$$

The ^{16}O(^{3}H,n)^{18}F and ^{6}Li(^{7}Li,2n)^{11}C reactions are energetically possible (TUNL Nuclear Data Project 2010). Furthermore, ^{6}Li + ^{7}Li reactions have been studied at length at higher energy producing B, C and Be isotopes by the emission of protons, deuterons, tritons, α particles, neutrons, and He nuclei (Berkowitz et al. 1962, 249). The known reaction cross-sections range from μb to tens of μb (Kibler 1967, 156). These reactions are analyzed by collection of the smaller of the charged emitted particles or γ radiation emitted by excited product nuclei (Kibler 1967, 156). ^{14}N can also transmute neutrons indirectly in the $Li_2B_4O_7$ lattice as follows,

$$\begin{aligned} &{}^{6}Li\left(n,\alpha\right){}^{3}H \rightarrow {}^{14}N\left({}^{3}H,2n\right){}^{15}O - 1.29MeV \rightarrow {}^{15}O\left(\beta^{+}\right){}^{15}N \\ &{}^{14}N\left(\alpha,\gamma\right){}^{18}F + 4.42MeV \rightarrow {}^{18}F\left(\beta^{+}\right){}^{18}O \end{aligned} \tag{4}$$

The ^{14}N in the second reaction in equation 4 would be an impurity introduced to the crystal from the atmosphere during growth. The, ^{14}N(^{3}H,2 n)^{15}O reaction is energetically possible with the 2.78 MeV ^{3}H nuclei produced in the ^{6}Li(n,α)^{3}H reaction.

In addition to a viable reaction mechanism to transmute neutrons, the absorption cross-section for the absorbing species is critically important to neutron detection. The absorption cross-section, σ_a, is a measure of the probability for the target nucleus to undergo the reactions outlined above. The larger the absorption cross-section, the greater the probability of reaction. The probability of reaction for a bombarding nucleus in a target medium is described by $e^{-\Sigma_a x}$. Where x is the distance traveled in the target medium, and Σ_a is the macroscopic absorption cross-section. The macroscopic absorption cross-section is the product of the microscopic absorption cross-section, σ_a, and the number density of the target nuclei, N. Therefore, the larger the σ_a, the smaller the required N to achieve the same probability of reaction. In turn, detectors can be made smaller and more useful in real world applications. At 3845.24 barns and 955.47 barns for thermal neutrons (0.025 eV), the microscopic cross-sections for absorption for ^{10}B and ^{6}Li are among the largest known (Bruker Corporation n.d.). Figure 3 shows the cross-section for nuclei present in $Li_2B_4O_7$ crystals and ^{157}Gd for comparison. The cross-sections for ^{6}Li + ^{7}Li reactions are not known at energies below 1 MeV.

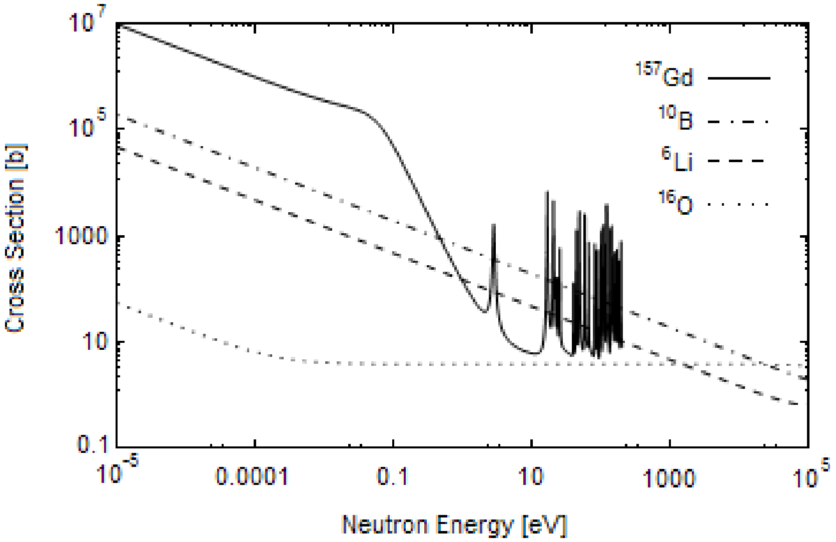

Figure 3. Neutron absorption cross-sections for selected isotopes. ^{157}Gd is not present in the $Li_2B_4O_7$ crystals. It is included for comparison. ^{6}Li and ^{11}B have similar cross-sections as ^{16}O. Plot data taken from ENDF data from the NNDC (Brookhaven National Laboratory 2006).

2.3 Electron Paramagnetic Resonance (EPR)

Electron paramagnetic resonance is the detection of the absorption spectrum of a paramagnetic species in an applied magnetic field. A class of paramagnetic species is one which has a permanent magnetic dipole that is randomly oriented in the absence of an applied magnetic field. The application of an external magnetic field can order the otherwise randomly oriented magnetic dipole (Abragam and Bleaney 1970, 1).

A common paramagnetic species is an unpaired electron. The magnetic dipole of the paired electron is offset by its pair. Therefore, it has only one spin state available to occupy and only one available energy state. The unpaired electron has two available spin states, and therefore at least two available energy states. One energy state has the magnetic dipole parallel to the applied magnetic field, and one anti-parallel. Much like a simple pendulum has two equilibrium positions, a free electron in a magnetic field also has two available states. The simple pendulum equilibrium are one stable, with the center of mass below the pivot point, and one unstable with the center of mass above the pivot point. The unstable equilibrium is also higher in energy, because the center of mass is in a higher potential state. Similarly, the two spin states of the free electron differ in energy. The lower energy spin state is preferred, but the higher energy spin state can be achieved with sufficient energy. EPR orients the paramagnetic species with an applied magnetic field, and microwave radiation excites the species from the low energy state to the high energy state (Weil, Bolton and Wertz 1994, 20). This absorption is indirectly measured. EPR spectra are generally taken at low temperatures, because at higher temperatures, the population of paramagnetic species in the higher energy state reduces the absorption signal. Additionally, at very low temperatures, saturation of the low energy states prevents relaxation after excitation.

In single-crystal samples, point defects can be paramagnetic. Examples of defects that can be paramagnetic are:

a) Point defect in crystals such as nitrogen atoms in diamond, or transition metal doping ions in $Li_2B_4O_7$.

b) Localized donor and acceptor states produced by doping of semiconductors.

c) Point defects produced by electromagnetic or particle irradiation, or chemical treatment such as color additive; these may be neutral atoms, an electron occupying a negative ion vacancy (F centers), a positive ion vacancy with an electron missing from an adjacent ion (V_1 centers), and similar defects more complicated in nature.

d) Stable free radicals, a few gaseous stable molecules, and many unstable free radicals.

e) Conduction electrons in metals and semiconductors (Abragam and Bleaney 1970, 39).

Of these defect types, the transition metal ions, F centers, and V_1 centers are important to understanding the hyperfine spectra observed from $Li_2B_4O_7$. In addition, the origin of the observed centers: as-grown defects; defects produced by electromagnetic radiation; or defects produced by particle radiation, is critical to understanding the hyperfine spectra. The hyperfine spectrum for a defect is the microwave radiation absorption spectrum for that defect. The spectrum shape is commonly a Gaussian centered on the difference in energy between energy states available to the defect. Transitions must obey quantum mechanics selection rules. The spectrum is normally displayed as a first derivative for more precise identification of the zero cross over. The amplitude of each spectrum peak is related to the number of the responsible transition(s) (Abragam and Bleaney 1970, 119).

The oxidation state of transition metal ions doped in $Li_2B_4O_7$, and the ion concentration within the crystal determine whether or not the ion will be distinguishable in the hyperfine spectrum. Although most bonds within the crystal are covalent, the ionic bonding image of transition metal ions is instructive to understanding the paramagnetic nature of doping ions. Ag^{1+} ions are not paramagnetic; they do not contain an unpaired electron. Neutral Ag atoms and Ag^{2+} ions both contain an unpaired electron, and they are paramagnetic. Ag^{1+} ions substitute Li^{1+} ions in the crystal lattice, and therefore they must be induced into an alternate oxidation state to be observed in the hyperfine spectrum. In contrast to Ag, Mn has only one common oxidation state, Mn^{2+}. Mn^{2+} ions substitute for Li^{1+} ions in the crystal. Mn^{2+} contains five unpaired electrons and is paramagnetic when present in as-grown crystals (Bruker Corporation n.d.).

The character of the hyperfine spectrum for defects, magnitude, and number of peaks as well as the energy splitting between peaks, often makes EPR a definitive analytical technique in identifying those defects. In addition to the two energy levels of the unpaired electron, J-I coupling between the nuclear magnetic moment and the electric magnetic moment further split those energy levels (Weil, Bolton and Wertz 1994, 15). The number of energy levels available is (2* I +1)*(2*J + 1).

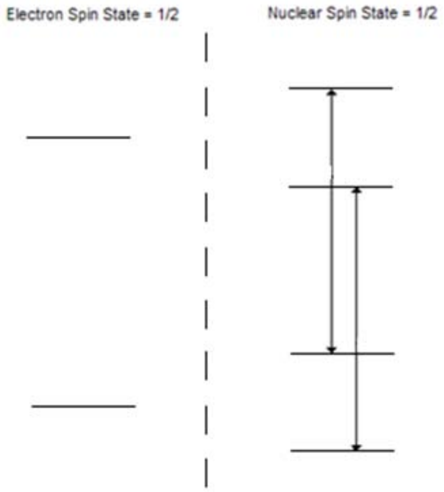

Figure 4. The available energy levels and strongly allowed transitions, ΔM = ±1, Δm = ±0, of an unpaired electron on a spin ½ nucleus.

Figure 4 shows the number of energy levels available to an unpaired electron interacting with a spin ½ nucleus. The two naturally occurring isotopes of Ag are spin ½ nuclei. The energy level of a paramagnetic species in a strong magnetic field is (Abragam and Bleaney 1970, 28),

$$W = g\beta HM + AMm - g_n\beta_n m\,. \tag{5}$$

Where W is energy, g is the magnitude of the electronic Zeeman factor, β is the Bohr magneton, H is the magnetic field strength, A is the magnitude of the hyperfine coupling tensor, M is the electronic magnetic quantum number, g_n is the nuclear g factor, and m is the nuclear magnetic quantum number. A strong magnetic field is when A « gβH (Abragam and Bleaney 1970, 28). For a free electron $g = g_e = 2.002319$ (Weil, Bolton and Wertz 1994, 17). For strongly allowed EPR transitions, ΔM = ±1 and Δm = ±0, where M is the electronic magnetic moment, and m is the nuclear magnetic moment, the energy difference between available states is (Abragam and Bleaney 1970, 28),

$$W = g\beta H + Am. \tag{6}$$

Equation 7 shows that EPR hyperfine spectra for a paramagnetic species will be centered at energy $g\beta H$, and splitting between peaks is A. The available values of *m* are separated by the integer value 1. For weakly allowed EPR transitions, ΔM = ±1 and Δm = ±1, the energy difference between available states is,

$$W = \left| g\beta H - \frac{1}{2}A + g_n\beta_n H \right|. \tag{7}$$

The weakly allowed transitions require changes in the nuclear and electronic magnetic moments, and are therefore less intense (Abragam and Bleaney 1970, 30).

The dependence of the hyperfine spectrum on the nuclear spin allows differentiation between different isotopes of the same atom. For instance, the nuclear spin of ^{11}B is 3/2, while the nuclear spin of ^{10}B is 3. These two isotopes will produce distinctly different hyperfine spectra, and therefore will be distinguishable through EPR. Additionally, the nuclear magnetic moment of the nearest neighbors of a paramagnetic species in a single crystal may further split the energy levels available to the unpaired electron. Figure 5 shows the number of energy levels available to an unpaired electron interacting with a spin ½ nucleus additionally interacting with a nearest neighbor nucleus of spin ½ . A practical example would be an Ag^{2+} ion with a nearest neighbor Ag^{1+} ion. Each available energy transition corresponds to a peak in the EPR or ENDOR hyperfine spectrum.

In some cases, the g and/or g_n factors of different isotopes are sufficiently close in magnitude, that hyperfine spectra overlap. In practice this has the effect of obscuring hyperfine spectra. The spectra can sum both constructively and destructively to yield hyperfine spectra significantly different than that of an isolated isotope. This can be either helpful or problematic in analyzing hyperfine spectra depending on the level of overlap. In other cases differences on the magnitude of hyperfine spectra can arise from differences in the isotopic abundances of various isotopes of the same atom. In this case, the magnitude of the hyperfine spectra will correlate directly to the level of isotopic enrichment. In this scenario the number of peaks in the hyperfine spectrum, and their relative intensities can give definitive proof of the responsible atomic species. In still other cases, the level of hyperfine interference is too complex to leave any of the individual components recognizable.

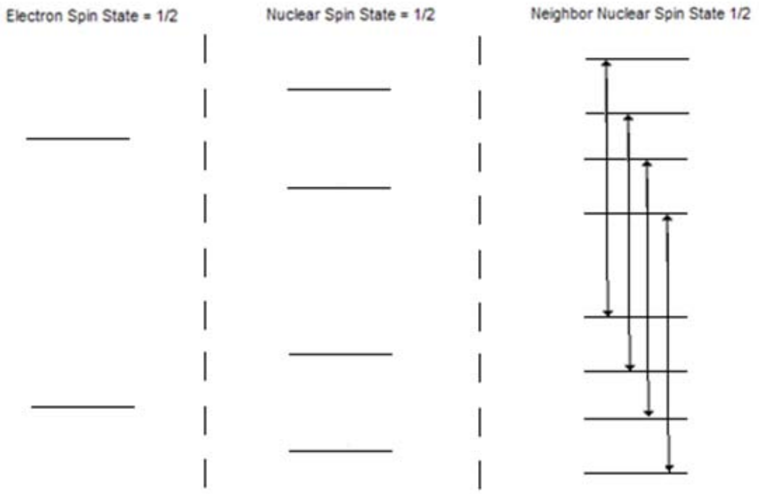

Figure 5. The available energy levels and strongly allowed transitions, $\Delta M = \pm 1$, $\Delta m = \pm 0$, of an unpaired electron on a spin ½ nucleus interacting with a nearest neighbor spin ½ nucleus.

Figure 6 shows a system diagram for a typical EPR spectrometer. The resonant cavity is flanked by two large electromagnets. These provide the time varying magnetic field necessary to align the otherwise randomly oriented paramagnetic species. The intensity of the magnetic field is commonly measured with an NMR probe not shown in the diagram (Weil, Bolton and Wertz 1994, 474).

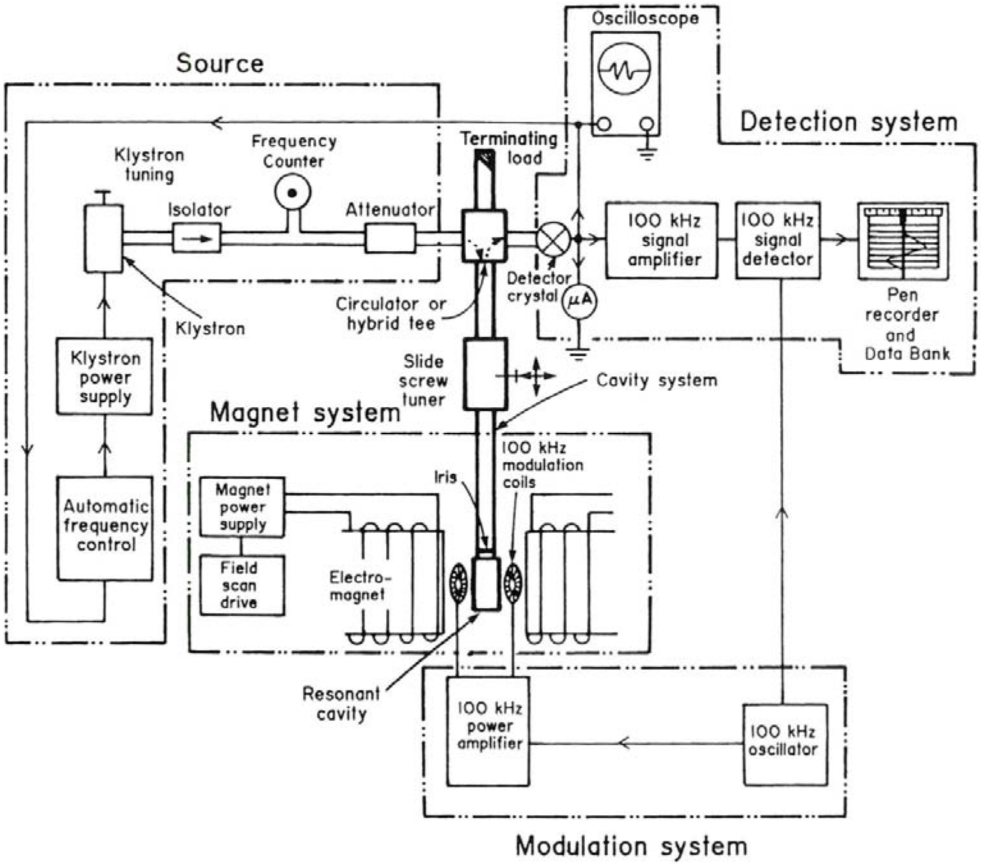

Figure 6. EPR system diagram. This diagram is taken directly from the Weil text (Weil, Bolton and Wertz 1994, 473).

Above the resonant cavity in the diagram is a rectangular wave guide referred to as the cavity system. This provides a path for microwave radiation to enter the resonant cavity and excite the paramagnetic defects in the sample. The wave guide also provides a pathway for reflected microwave radiation to exit the resonant cavity after it is partially absorbed by the paramagnetic defects in the sample (Weil, Bolton and Wertz 1994, 476). The inbound and outbound microwave radiations are separated by the circular or hybrid tee located in the diagram atop the cavity system. The circulator is a four point nonreciprocal device. It permits transmission of microwave radiation in only one direction depending on the polarization plane of the microwaves (Weil, Bolton and Wertz 1994, 477).

The circulator functions somewhat like a traffic circle (see Figure 7). Microwaves can only travel one direction around the circle, and exit at the first possible path after entering the circle. Microwaves from the source enter at position 1, and exit to the cavity at position 2. Microwaves reflected from the cavity enter at position 2 and exit to the detector at position 3. Lastly, microwaves reflected from the detector enter at position 3, and exit at position 4 where they are stopped with the terminating load. The terminating load functions to prevent reflection of microwaves back into the detector arm (Weil, Bolton and Wertz 1994, 477).

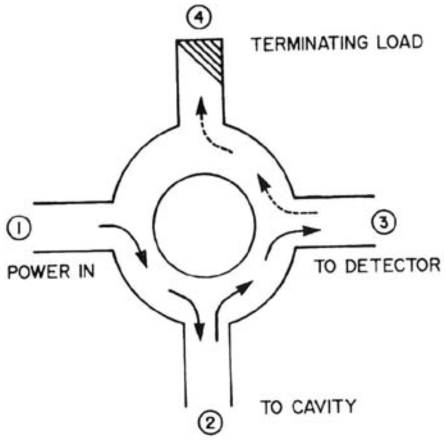

Figure 7. Circulator or hybrid tee. This diagram is taken directly from the Weil text (Weil, Bolton and Wertz 1994, 477).

The source of microwave radiation is the Gunn diode. The Gunn diode energy is variable over a band of frequencies, but is held constant during spectrum acquisition. The Gunn diode energy is held constant during spectrum acquisition, and the magnetic field strength is varied because the magnetic field can be varied with much greater accuracy than the Gunn diode energy (Weil, Bolton and Wertz 1994, 472). The microwave energy is measured very accurately by a frequency counter, and the microwave power is lowered as desired by an attenuator (Weil, Bolton and Wertz 1994, 476).

The detector system is typically a silicon crystal in contact with a tungsten wire which acts as a microwave rectifier (Weil, Bolton and Wertz 1994, 483). The signal is electronically converted to a first derivative and displayed via a computer console. Figure 6 shows a pen recorder which would now be replaced by the computer console. The first derivative output displays the position in the spectrum of magnetic field strength that paramagnetic defects absorbs and re-emits incident microwave radiation. The zero crossover of the first derivative locates the maximum absorption field strength accurately, and the peak to trough distance accurately locates the full width at half the absorption maximum. By comparing the intensity, position and number of absorption peaks with the known nuclei in a sample, the nature and location of paramagnetic defects can be determined.

2.4 Electron-Nuclear Double Resonance (ENDOR)

Electron-nuclear double resonance is similar to EPR. Where EPR primarily excites the strongly allowed transitions electronic transitions, $\Delta M = \pm 1$ and $\Delta m = \pm 0$, ENDOR excites the nuclear transitions, $\Delta M = \pm 0$ and $\Delta m = \pm 1$. In strong magnetic fields, the energy difference between available states is

$$W = \left| AM - g_n \beta_n H \right| . \tag{8}$$

This energy difference, which results from changing the nuclear magnetic moment, is orders of magnitude less than the energy difference that results from changing the electronic magnetic moment (Abragam and Bleaney 1970, 31). As a result, ENDOR excites the paramagnetic species with radio waves as opposed to the microwaves required with EPR. Figure

8 shows the nuclear transitions of an unpaired electron on a spin ½ nucleus. Since the ENDOR spectrum depends on g_n instead of g and g_n, it is possible to separate the spectra of ions such as $^{107}Ag^{2+}$ and $^{109}Ag^{2+}$ which overlay almost exactly in the EPR spectrum. In the case of the two Ag isotopes, the g_n values are ^{107}Ag: 0.227249 and ^{109}Ag: 0.2261743, providing enough separation in the ENDOR spectrum to be distinguishable (Bruker Corporation n.d.). Equation 9 shows that hyperfine ENDOR hyperfine spectra for a paramagnetic species will be centered at energy $g_n \beta_n H$, and energy splitting between peaks will be A. The available values for M are ± ½ .

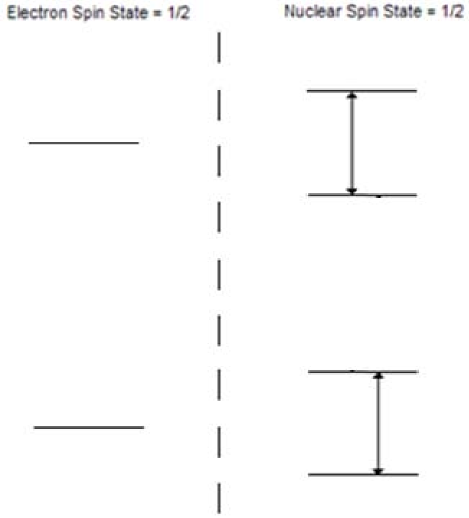

Figure 8. The available energy levels and allowed transitions, $\Delta M = \pm 0$, $\Delta m = \pm 1$, of an unpaired electron on a spin ½ nucleus.

The ENDOR system is largely the same as an EPR. An EPR spectrum is used to fix the magnetic field to the zero crossover of an absorption maximum, and a radio frequency generator is used to create variable excitation radiation. The absorption spectrum is presented in a first derivative format like the EPR spectrum, and like EPR, the position, number and relative intensity of absorption maxima can identify the nature and location of paramagnetic defects. ENDOR can differentiate similar isotopes that go unresolved in EPR spectra.

2.5 Thermoluminescence (TL)

Thermoluminescence is the radiative recombination of electrons and hole subsequent to thermal excitation of trapped electrons and/or holes from shallow traps. Figure 9 shows the various excitation and recombination routes available during the TL process. Excitation of holes to the valence band and/or excitation of electrons to the conduction band is a non radiative process. Defects trapping charges must be relatively shallow with respect to either the conduction or valence bands to allow excitation by thermal energy. Deep traps will not release trapped charges readily prior to thermal damage to the host material. Recombination of electron/hole pairs can occur along four separate routes after excitation: conduction band to valence band; conduction band to hole trap; electron trap to valence band; or electron trap to hole trap.

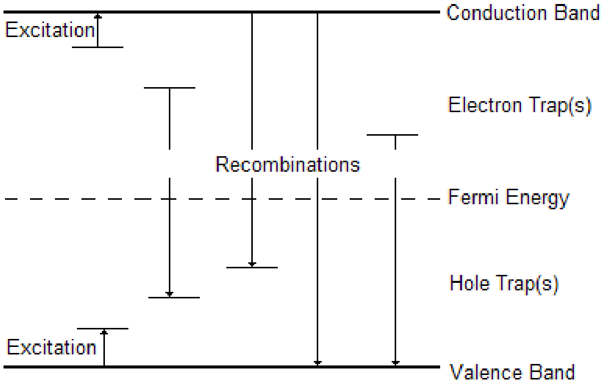

Figure 9. Thermoluminescence mechanism: excitation is a non-radiative process while recombination is radiative.

Each of these recombination mechanisms will have a different energy, radiating a different photon wavelength. The radiated light is captured and analyzed. Conventional TL measurements simply measure the bulk intensity of light radiated. This bulk light measurement is called a TL glow curve or bulk glow curve. This method can determine the total number of charges trapped in the material that radiatively recombined. By utilizing a CCD spectrometer to capture the radiated light as a function of wavelength, both the total number of charges, and the different recombination mechanisms can be determined.

2.6 Neutron Activation (nA)

Knowledge of impurities not apparent in EPR spectra because they are non-paramagnetic or due to low number density can aid in understanding the charge annealing process, and recombination mechanisms/sites. Defects visible in the EPR hyperfine spectrum are largely due to charge trapped at those defects. Trapped charges that are not paramagnetic and therefore do not appear in the EPR spectrum cannot be accounted for in PA or TL studies. Neutron activation is a powerful method of identifying trace or non-paramagnetic impurities in crystals. Knowledge of trace and non-paramagnetic impurities could suggest mechanisms for charge trapping and recombination not suggested by EPR spectra alone. Neutron activation is the process of converting a stable isotope into an unstable isotope through neutron absorption. The process is initiated by placing an isotope into a neutron flux. The isotope may absorb a neutron thus converting it to another isotope with one additional neuton. The absorption of a neutron by ^{109}Ag to form ^{110}Ag is an example of neutron activation. The resulting ^{110}Ag is radioactive, and can be detected by gamma ray spectroscopy (Glascock 2010).

Two limitations of neutron activation are production of stable isotopes or radioactive isotopes with extremely long half lives, or production of radioactive isotopes from a trace impurity producing an extremely low intensity spectrum, or a spectrum poorly resolved from other spectrum features. An example of the first limitation would be Fe. Through neutron absorption, Fe largely produces other stable Fe isotopes, and is therefore difficult to identify via neutron activation. An example of the second limitation would be coexisting Cu and La impurities. La and Cu have similar half lives, and the presence of one in high intensity may obscure or totally overwhelm the other. Either of these limitations could hide significant impurities from discovery through neutron activation analysis.

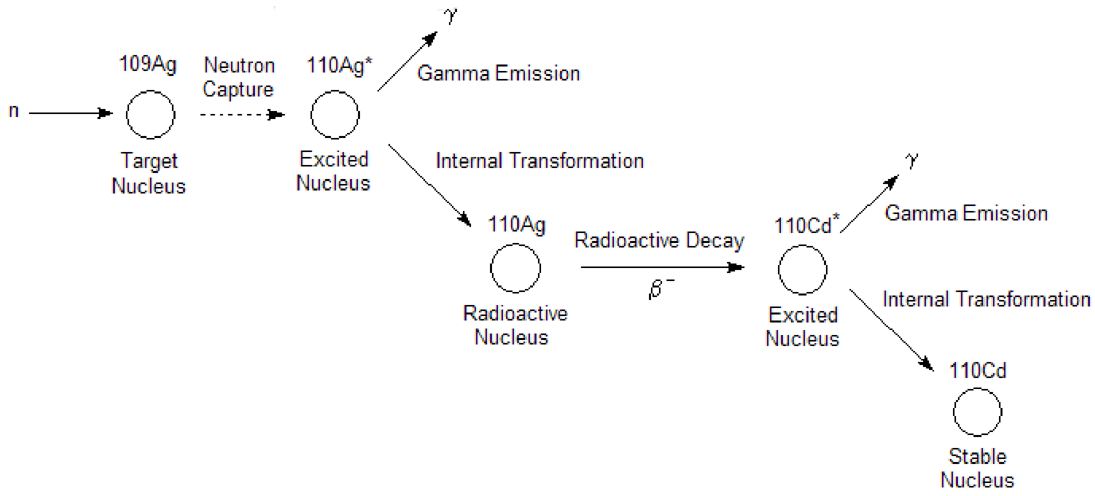

Figure 10. Neutron capture and gamma ray emission for ^{109}Ag. Image adapted from one in the reference (Glascock 2010).

Gamma ray spectroscopy (GRS) can positively identify radioactive isotopes. Most radioactive isotopes emit characteristic gamma radiation during decay. The energy and probability of emission of gamma radiation is unique to each radioactive isotope. These gamma rays amount to a fingerprint of radioactive decay of the radioactive isotope. Furthermore, matching several different energy gamma ray emissions from a single radioactive isotope increases confidence in the identity of the radionuclide (Glascock 2010).

2.7 Pulsed Anneal (PA)

Pulsed anneal is the sequencing of annealing steps and EPR spectrometry. An annealing step consists of rapidly heating a crystal to an annealing temperature, and holding it at that temperature for a relatively short period of time. After the annealing step, the crystal is rapidly cooled to cease any charge trap annealing, and an EPR spectrum is obtained. The annealing temperature in then slightly increased, and the process repeated. The annealing temperature of charge traps in the material can be determined comparing EPR spectrum subsequent to each annealing step. Comparison of the various charge trap annealing temperatures in similar crystals with different doping can illuminate the recombination mechanism responsible for TL.

2.8 Literature Review

In 2010 a series of EPR studies of as-grown defects in $Li_2B_4O_7$ was conducted. In that work, it was noted that Li vacancy V_1 centers and O vacancy F centers were present (M. J. Swinney 2010, 1). Figure 11 shows the EPR spectra of the as-grown defects noted by Swinney. The top spectrum shows the four peak hyperfine structure of the O vacancy F center that surround the seven peak hyperfine structure of the Li vacancy V_1 center. The Li vacancy V_1 center can be seen well in the bottom spectrum. The bottom spectrum was taken at 40 K to resolve the Li vacancy center. At 20 K, the Li vacancy V_1 center is saturated. Swinney also noted that both charge traps annealed at a temperature of approximately 100 K (M. Swinney 2009, 57).

Since 2000 Burak, Matkowski, and Skvortsova conducted a series of experiments on defects induced in isotopically enriched $Li_2B_4O_7$. He studied EPR spectra of neutron irradiated crystals of various isotopic enrichments, as well as optical absorption measurements of those same crystals (Burak et al. 2004; Buraket al. 2002; Matkovski et al. 1994; and Skvortsova et al. 2000). Burak concluded that amongst other defects, Li clusters were formed in the crystals as a result of the neutron irradiation (Burak, Padlyak and Shevel 2002, 1103).

Since 2005, Kelemen and Ignatovych performed a series of studies on doped $Li_2B_4O_7$ crystals including optical absorption, EPR, and TL both before and after β^- irradiation (M. Ignatovych et al. 2005; M. Ignatovych et al. 2007; Kelemen, Holovey and Ignatovych 2008; and Kelemen et al. 2007). They conclude that amongst other defects, knock-on damage results in Ag clusters in $Li_2B_4O_7$:Ag crystals (Kelemen, Holovey and Ignatovych 2008, 377).

Between 1962 and 1967, Berkowitz and Kibler separately studied Li + Li reactions including ^{6}Li + ^{7}Li and ^{7}Li + ^{7}Li reactions (Berkowitz et al. 1962, Kibler 1967).

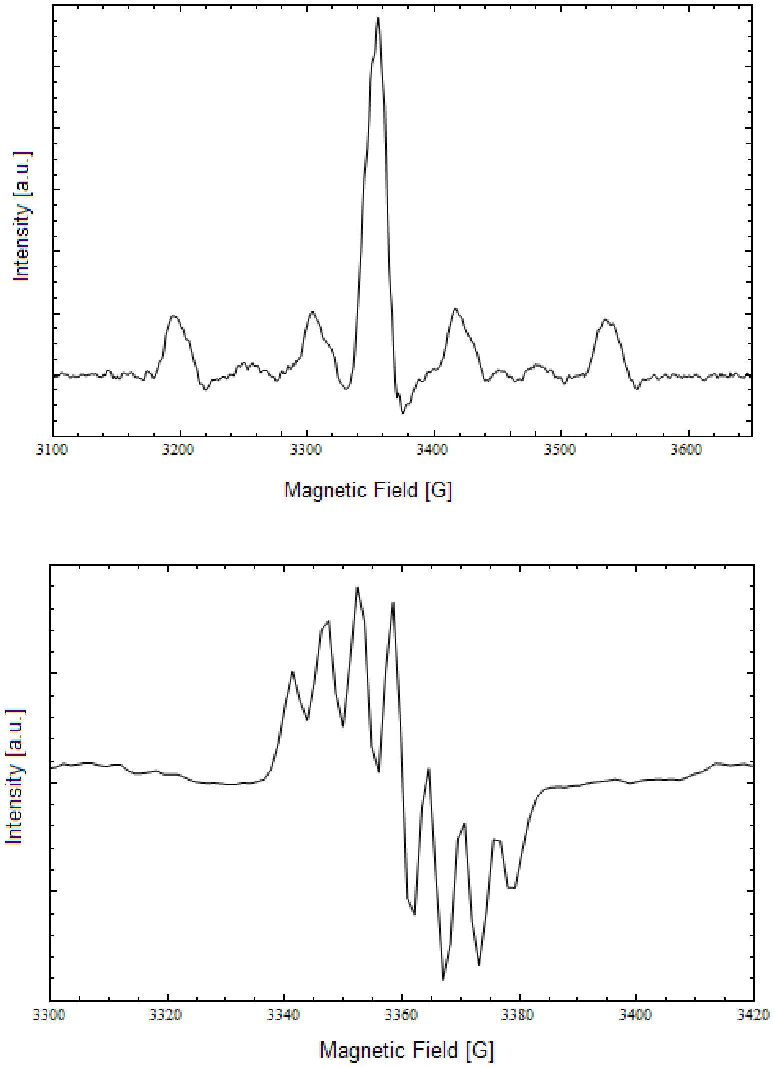

Figure 11. EPR spectra of as-grown defects in $Li_2B_4O_7$. The top spectrum was obtained at 20 K, and the bottom spectrum was obtained at 40 K. The magnetic field was aligned with the [001] direction.

Berkowitz noted that in the ^{6}Li + ^{7}Li reaction, ^{11}C a positron emitter is produced. Also noted was that the ^{7}Li + ^{7}Li reaction did not produce ^{11}C (Berkowitz et al. 1962, 251). Kibler conducted his experiments at higher energy than Berkowitz, and noted absorption cross-sections for the ^{6}Li + ^{7}Li reaction in the 1 to 10 μb range (Kibler 1967, 1115).

III. Experimental Concept

3.1 Primary Goal: Characterization of Neutron-Induced Defects

Characterization of neutron induced defects in $Li_2B_4O_7$ consisted of three steps: pre-characterization of as-grown defects in $Li_2B_4O_7$ crystals, neutron irradiation, and characterization of defects in neutron irradiated $Li_2B_4O_7$ crystals. Four types of $Li_2B_4O_7$ crystals were examined. First $Li_2B_4O_7$ with a natural abundance of ^{6}Li and ^{10}B ($Li_2B_4O_7$), second $Li_2B_4O_7$ enriched in ^{10}B ($Li_2B_4O_7$:^{10}B), $Li_2B_4O_7$ enriched in ^{6}Li ($Li_2B_4O_7$:^{6}Li), and Ag-doped $Li_2B_4O_7$ ($Li_2B_4O_7$:Ag).

Defect pre-characterization was conducted with EPR, ENDOR, TL, pulsed anneal, neutron activation, and gamma ray spectrum analysis. Post-neutron irradiation characterization was conducted by EPR, TL and limited pulsed anneal. EPR and ENDOR were conducted at West Virginia University with a Bruker EMX spectrometer and a Bruker Elexsys E-500 spectrometer respectively. EPR/ENDOR was conducted with Adam T. Brant under the supervision of Dr. Larry E. Halliburton between March 2010 and November 2010. The EPR microwave source was operated near 9.47 GHz to excite paramagnetic species, and a pair of electromagnets on either side of the sample chamber was operated from 1 to 13,000 G. Precise measurement of the microwave frequency was accomplished by a frequency counter. Fine measurement of the magnetic field was accomplished by an NMR gauss-meter near the sample position. Precise determination of the magnetic field at the sample position was determined by replacing the sample with a sample of Cr doped MgO, and correcting the magnetic field from the isotropic g value of 1.9800 for the Cr^{3+} ion in MgO.

Excitation in the ENDOR spectra was accomplished via a radio frequency generator operating from 30 – 50 MHz. The temperature in the sample chamber of the EPR/ENDOR was controlled via He gas evolved from liquid He pumped by an Oxford system. EPR/ENDOR spectra were taken at temperatures ranging from 3-100K. Some crystals were exposed to x-ray radiation from a Varian OEG-76H x-ray tube to populate charge traps. X-ray exposure was conducted at either room temperature or 77 K. Immersion in liquid nitrogen provided 77 K temperatures during x-ray exposure. Rapid movement of samples from liquid nitrogen immersion to a cooled sample chamber kept them below 90 K throughout x-ray exposure and EPR/ENDOR spectroscopy.

Table 1. EPR/ENDOR Spectra Obtained

$Li_2B_4O_7$

Neutron Energy	Neutron Interaction Density [cm-3]	X-ray Irradiation Temperature [K]	Magnetic Field Alignment	EPR Spectrum Temperature(s) [K]	PA* Temperatures [K]
None	None	77	[001]	20	50, 70, 90
None	None	77	[001]	40	None
None	None	77	[100]	20, 40	None
Fast	10^{15}	None	[001]	12, 20, 25, 30, 40	None
Thermal	10^{15}	None	[001]	40	None
Thermal	10^{15}	77	[001]	25, 40	None
Thermal	10^{17}	None, 77	[001]	12	None

$Li_2B_4O_7$:^{10}B

Neutron Energy	Neutron Interaction Density [cm-3]	X-ray Irradiation Temperature [K]	Magnetic Field Alignment	EPR Spectrum Temperature(s) [K]	PA* Temperatures [K]
None	None	77	[001]	40	None
None	None	77	[100]	22, 40	None
Fast	10^{15}	None	[001]	10	None
Thermal	10^{15}	None	[001]	12, 25, 40, 78	None
Thermal	10^{17}	None	[001]	10	None

$Li_2B_4O_7$:^{6}Li

Neutron Energy	Neutron Interaction Density [cm-3]	X-ray Irradiation Temperature [K]	Magnetic Field Alignment	EPR Spectrum Temperature(s) [K]	PA* Temperatures [K]
None	None	77	[001]	12, 35	None
Fast	10^{15}	None, 77	[001], [100]	12	None
Thermal	10^{15}	None	[001], [100]	12	None
Thermal	10^{17}	None, 77	[001], [100]	12	None
Thermal	10^{17}	77	[100]	12	None

$Li_2B_4O_7$:Ag EPR

Neutron Energy	Neutron Interaction Density [cm-3]	X-ray Irradiation Temperature [K]	Magnetic Field Alignment	EPR Spectrum Temperature(s) [K]	PA* Temperatures [K]
None	None	293	[001]	13, 20, 30, 50	348, 373, 398, 423, 448, 473, 498
None	None	293	[001], [100], [101], [110]	15	None
None	None	77	[001]	4, 15, 30, 35, 40, 45	77, 90, 105, 293, 348, 373, 398, 423, 448, 473, 498
Thermal	10^{15}	None	[001]	40 K	423, 453, 478

$Li_2B_4O_7$:Ag ENDOR

Neutron Energy	Neutron Interaction Density [cm-3]	X-ray Irradiation Temperature [K]	Magnetic Field Alignment	EPR Spectrum Temperature(s) [K]	PA* Temperatures [K]
None	None	293	[001], [100], [101], [110]	15	None

$Li_2B_4O_7$:Mn

Neutron Energy	Neutron Interaction Density [cm-3]	X-ray Irradiation Temperature [K]	Magnetic Field Alignment	EPR Spectrum Temperature(s) [K]	PA* Temperatures [K]
None	None	None	~[001]	10	None

$Li_2B_4O_7$:Cu

Neutron Energy	Neutron Interaction Density [cm-3]	X-ray Irradiation Temperature [K]	Magnetic Field Alignment	EPR Spectrum Temperature(s) [K]	PA* Temperatures [K]
None	None	77, 293	[001]	9, 11, 15	None

*PA is pulsed anneal

Neutron irradiation and activation was accomplished at the Ohio State University Research Reactor (OSURR). Mr. Joe Talnagi assisted with activation and irradiation, and gamma ray spectroscopy subsequent to activation. A sample reactor spectrum is described in Appendix A. Gamma ray spectra were obtained using a 3” x 3” High Purity Germanium (HPGe) semiconductor detector. Irradiation times for samples were adjusted to produce n,^{10}B and n,^{6}Li interaction densities of ~10^{15} cm^{-3} or ~10^{17}cm^{-3}. Samples were irradiated in the “rabbit tube”, central irradiation facility (CIF), and 7” dry tube depending on crystal composition, desired interaction density, and desired irradiation time.

The CIF is a 1.5” diameter steel pipe running into the center of the fuel assembly of the OSURR from the top. This provides the largest fluxes available in the OSURR. Samples are lowered into and taken out of the CIF is a crystal basket attached to a cotton cord by an aluminum wire. The aluminum wire activates significantly during neutron irradiation, and time must be allowed to pass prior to retrieving the basket after reactor shut down. The 7” dry tube is a 7” diameter aluminum tube fixed outside the fuel assembly of the OSURR. The 7” dry tube position provides a greater thermal to fast neutron ratio in the neutron flux, and a lower total flux than the CIF. The “rabbit tube” is a mechanism for fast insertion and retrieval of samples from a position just outside the fuel assembly. Samples are rapidly inserted and extracted via a pneumatic system. The flux in the “rabbit tube” is greater than that of the 7” dry tube, but less than the CIF.

Some crystals were Cd wrapped to harden the reactor flux to investigate the effects of fast neutron interactions. Cd has a relatively large cross-section for capture of thermal neutrons. The corresponding cross-section for high energy neutrons is much smaller. As such, a Cd wrap attenuates thermal neutron flux much greater than fast neutron flux. Therefore, the energy spectrum of the flux that survives passing through a Cd wrap is hardened or the low energy flux is reduced relative the high energy flux. Work at the OSURR was conducted from 5 – 12 November, 2010. Additional neutron irradiations were conducted using the AFIT subcritical pile in drawer three. These irradiations and subsequent gamma ray spectroscopy were conducted in order to determine the source of positron annihilation radiation in the crystals. These investigations were conducted from 13 – 19 December, 2010.

The AFIT subcritical pile is a graphite pile with a PuBe neutron source. Figure 12 shows a diagram of the AFIT subcritical pile, and indicates the location of the drawer three position.

Drawer three provides the largest thermal flux available in the subcritical pile. The neutron energy spectrum for drawer three of the AFIT pile can be seen in Appendix A.

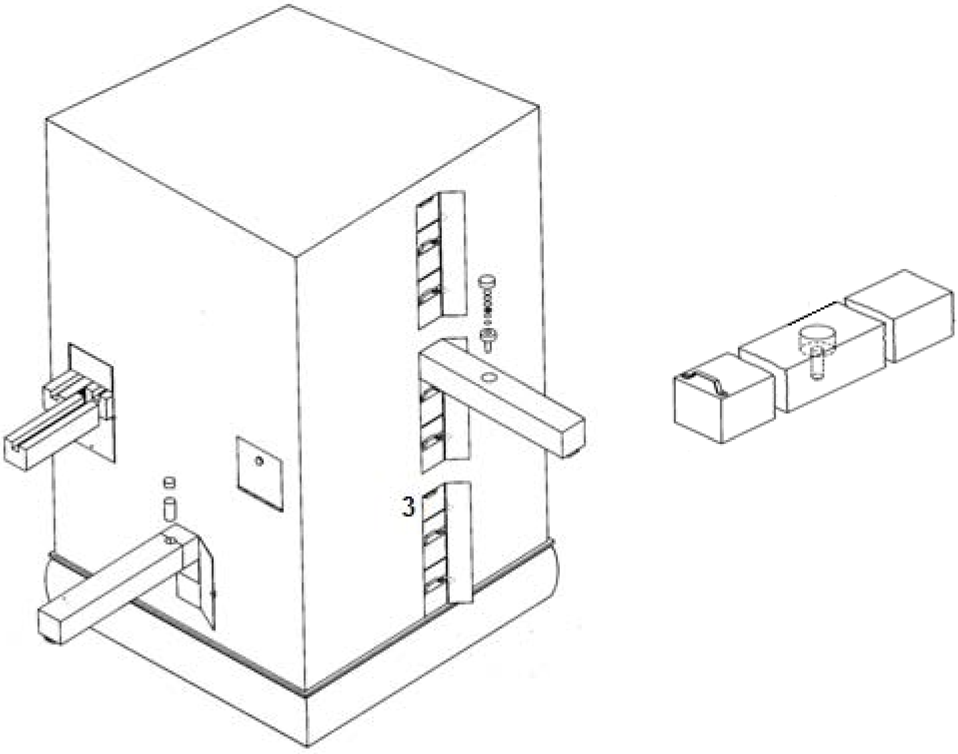

Figure 12. Schematic of the AFIT subcritical pile. Drawer three is indicated in the diagram with the 3 notation. The stringer sketch to the right shows the type of cylindrical cutout samples were placed in for irradiation. These diagrams were taken directly from the Airf Force technical documentary (Nuclear Engineering Test Facility Directorate of Engineering Test Aeronautical Systems Division 1962, 10,13).

3.2 Secondary Goal: Thermal Stability of Neutron Induced Defects

Paramagnetic defects unique to the neutron irradiated crystals were observed in all the neutron irradiated crystals. EPR spectra and limited pulsed anneal of the neutron irradiated $Li_2B_4O_7$:^{6}Li sample and $Li_2B_4O_7$:Ag sample indicated the presence of possible neutron induced defects of unique thermal stability. A limited pulsed anneal (PA) follows the same procedure as a

PA study, except that anneal temperatures are selected to minimize the number of annealing steps, and only rough estimates can be made of the annealing temperatures of charge traps. Full pulsed anneal studies require multiple annealing steps, and multiple x-ray irradiations to repeat the studies. This process had the potential to permanently anneal the possible neutron induced defects and prohibit further TL study. Therefore, limited pulsed annealing was conducted.

TL glow curves of these crystals were obtained using the Harshaw TLD-3500 and compared to glow curves from crystals before neutron irradiation. No preheat was used during TL measurement. The heating rate during glow curve acquisition was set to 1ºC per second, for a total acquisition time of 600 seconds. The maximum temperature reached was 300 ºC, sufficient to study the defects of interest as indicated by the limited pulsed anneals. Furthermore, 300 ºC is not known to permanently anneal any interstitial defects. No annealing was accomplished after the acquisition of the TL glow curve. The limited pulsed anneal consisted of determining a rough temperature at which the suspected neutron induce defects annealed. Samples irradiated to higher interaction densities generally had too many overlaying hyperfine spectra to discern the source of the defects. These samples were annealed until hyperfine structure(s) in the magnetic field region of neutron irradiation induced defects observed in other crystals were no longer detected. This provided a rough annealing temperature for the defects of interest, and facilitated acquisition of TL glow curves.

3.3 Tertiary Goal: Ag-Doped $Li_2B_4O_7$

The tertiary goal of characterizing the as-grown defects in Ag doped LTB, determining the thermal stability of these defects, and identifying the recombination site(s) associated with the TL of this crystal was accomplished by EPR, ENDOR, PA, TL, a production study, and a limited angular dependence study of paramagnetic defects. EPR was conducted in the same manner as for the primary research goal. ENDOR was conducted to verify the ion(s) responsible for paramagnetic defects, and to validate EPR angular dependence measurements. The ENDOR technique mirrored that used in for the primary research goal. PA of the Ag related charge traps was conducted with annealing steps of 25 ºC and 3 minutes duration. EPR spectra between annealing steps were obtained with the magnetic field aligned with (001). After obtaining EPR spectra, line widths were normalized to a 5 G line width for each paramagnetic species. The 5 gauss line width was selected for normalization because it provided a width similar to all lines being normalized. The method of normalization was,

$$\left(\frac{S}{N}\right)=\left(\frac{S}{N}\right)_0\left(\frac{w^2}{5^2}\right). \tag{9}$$

Where $\left(\frac{S}{N}\right)$ is the signal to noise ratio normalized to a 5 G line width, $\left(\frac{S}{N}\right)_0$ is the signal to noise ratio prior to normalization, 5^2 is the squared line width of the normalized line, and w is the peak line width in gauss. The normalized signal to noise ratio was then multiplied by the number of peaks in the hyperfine spectra for the species. This total intensity was taken to be directly related to the total number of the paramagnetic species. Thus, different species intensities could be compared directly.

The TL of the $Li_2B_4O_7$:Ag sample was accomplished and compared to the PA study. The comparison was intended to show the correlation between the thermal stability of various charge traps and the temperature dependence of the bulk glow curve. TL bulk glow curves were obtained in the same manner as for the primary research goal. A production study was accomplished to determine the relative rate at which charge traps populate within the $Li_2B_4O_7$:Ag crystal during x-ray irradiation. The production studies were accomplished by irradiating the $Li_2B_4O_7$:Ag sample with x-rays for short periods of time and obtaining EPR spectra in between x-ray irradiations. The EPR spectra were obtained with the magnetic field aligned along the (001). Line widths for the hyperfine spectra were normalized in the same manner described for the PA studies, and again the normalized signal to noise ratio was multiplied by the number of peaks in the hyperfine spectrum for each paramagnetic species to facilitate species to species comparisons. Production studies were accomplished at both 77 K and room temperature.

A limited angular dependence study was accomplished in order to determine the g tensor and A tensor values for the Ag^{2+} hole trap. EPR and ENDOR spectra were obtained with the magnetic field aligned with (001), (100), (110), and ~ (001). All other EPR variables were held constant. Determining the values of the g and A tensors for the Ag^{2+} species allows for definition of the spin Hamiltonian. These studies were conducted at the same time as similar studies for the primary research objective.

3.4 Fourth Goal: Positron Annihilation

The fourth research goal of identifying the source of positron annihilation gamma radiation was formulated after nA of various samples. Subsequent to neutron activation (nA), all $Li_2B_4O_7$ samples showed strong production of 511 keV gamma radiation. Determination of the source of the 511 keV gamma radiations was accomplished by nA and gamma ray spectroscopy. $Li_2B_4O_7$ with all types of doping ions and isotopic enrichments showed positron annihilation gamma radiation after nA. Gamma ray spectroscopy of samples never irradiated with neutrons was accomplished to determine the amount of 511 keV gamma radiations present in the crystals prior to nA, and to determine what radioactive impurities were present in the crystals. The nA analysis was accomplished to determine the effect of neutron irradiation on the amount of positron annihilation radiation, as well as the effect of different isotopic enrichments of ^{6}Li or ^{10}B on the production of positron annihilation gamma radiation. Gamma ray spectroscopy and nA was conducted in conjunction with the same studies for the primary research objective.

IV. Results

4.1 Primary Goal: Characterization of Neutron-Induced Defects

Characterization of neutron induced defects included both pre-characterization of crystals prior to neutron irradiation and characterization of crystals after neutron irradiation. $Li_2B_4O_7$, $Li_2B_4O_7$:^{6}Li, $Li_2B_4O_7$:^{10}B, and $Li_2B_4O_7$:Ag crystals were all characterized. Three crystals of each type were neutron irradiated to 10^{15} cm^{-3} and 10^{17} cm^{-3} thermal neutron interaction densities and 10^{15} cm^{-3} fast neutron interaction densities. Neutron interaction density was calculated by,

$$I_d = \frac{t}{V}\sum_j \sum_i \varphi A_j \left(1 - e^{N_i \sigma_i T_j}\right). \tag{10}$$

Where I_d is the total neutron interaction density (fast or thermal), t is the irradiation time, V is the crystal volume, j is the three principle directions ([100], [010], and [001]), i is the number of isotopes in the crystal, φ is the neutron flux (thermal or fast), A_j is the cross-sectional area of the crystal perpendicular to direction j, N_i is the number density of the i^{th} isotope, σ_i is the neutron absorption cross-section for the i^{th} isotope, and T_j is the thickness of the crystal in the j^{th} direction. One additional crystal of each type was kept for reference without neutron interaction. During some characterization steps, $Li_2B_4O_7$:Mn, and $Li_2B_4O_7$:Cu crystals were characterized outside the scope of this research. Those results are also presented here.

4.1.1 Electron Paramagnetic Resonance Pre-Neutron Irradiation

The paramagnetic defects observed in the $Li_2B_4O_7$, $Li_2B_4O_7$:^{6}Li, and $Li_2B_4O_7$:^{10}B crystals were the same as previously observed by Swinney in 2009. EPR spectra were obtained with the magnetic field aligned near [001]. The [001] alignment was approximate due to the lack of the Cu impurity used in previous work to align the [001] precisely. The Li vacancy V_1 center, seven peak hyperfine structure at 3360 G, and the O vacancy F center, four peak, broadly spaced, hyperfine structure at 3360 G were all noted by Swinney in 2010 (M. J. Swinney 2010). The as-grown defects in the $Li_2B_4O_7$:Ag crystal are outlined in the results and discussion for the tertiary research goal. The $Li_2B_4O_7$:Mn crystal was briefly characterized with the EPR to validate the presence of the Mn dopant. The expected 30 plus hyperfine structure of the Mn^{2+} ion was evident in the crystal (Lipinski 2006, 151). See Figure 13 for the $Li_2B_4O_7$:Mn spectra, with the magnetic field aligned near [001]. Additional characterization of this spectrum could be completed, however this complex spectrum would require a significant effort and time investment.

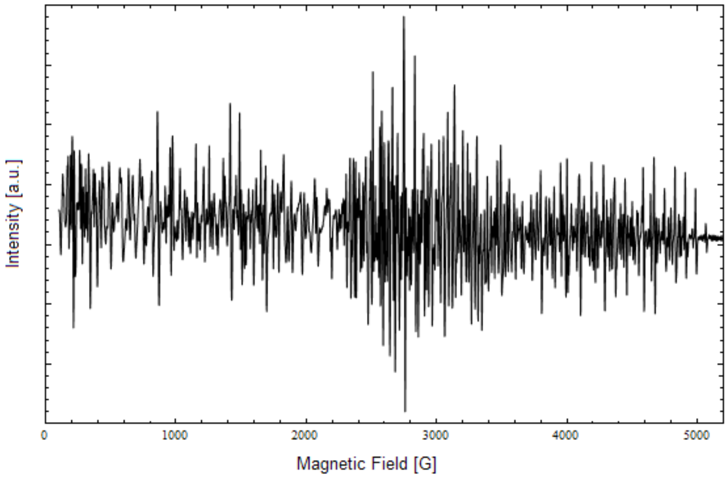

Figure 13. EPR spectra of $Li_2B_4O_7$:Mn. The magnetic field is aligned near the [001], the spectra were taken at 10 K. Mn is in the 2+ oxidation state in the crystal no x-ray irradiation is required to produce a paramagnetic state. Note Podgorska obtained similar spectra (Podgorska et al. 2004,202).

4.1.2 Pulsed Anneal Pre-Neutron Irradiation

Swinney observed the thermal stability of the Li vacancy V_1 centers in 2009; no Li vacancy V_1 centers were observed after the crystals was warmed to 90K (M. J. Swinney 2010). The thermal stability of Ag related defects are in chapter 4.3 along with other items concerning the tertiary research goal. The thermal stability of the O vacancy F center is not as clear. The O vacancy F center recombines at less than ~90 K in crystals with only the Li vacancy V_1 center. In crystals with other hole traps, the O vacancy shows much higher thermal stability.

4.1.3 Thermoluminescence Pre-Neutron Irradiation

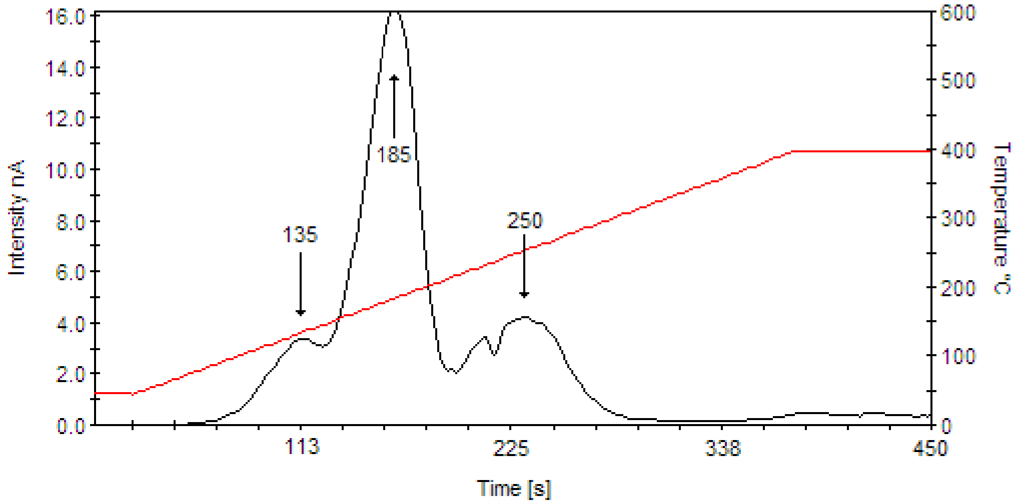

Figure 14. TL glow curve for $Li_2B_4O_7$:^{6}Li above room temperature prior to neutron irradiation. The crystal was not exposed to any x-ray radiation or other ionizing radiation deliberately.

In 2009 the TL response was demonstrated below 90 K in un-doped $Li_2B_4O_7$ regardless of Li or B enrichment (M. Swinney 2009, 57). Figure 14 shows the above room temperature bulk glow curve for $Li_2B_4O_7$:^{6}Li. The crystal was not deliberately exposed to x-ray or other ionizing radiation. Three glow peaks at 135, 185, and 250 ºC with relative intensities of 1:4.5:1.2 are observed. Figure 15 shows the above room temperature bulk glow curve for $Li_2B_4O_7$:^{10}B. The crystal was not deliberately exposed to x-ray or other ionizing radiation. Two peaks are visible at 185 and 250 ºC with relative intensities of 1:11. After anneal at room temperature, no defects are visible in the hyperfine EPR spectrum. Therefore, the defects responsible for these peaks are not observed in the EPR hyperfine spectrum.

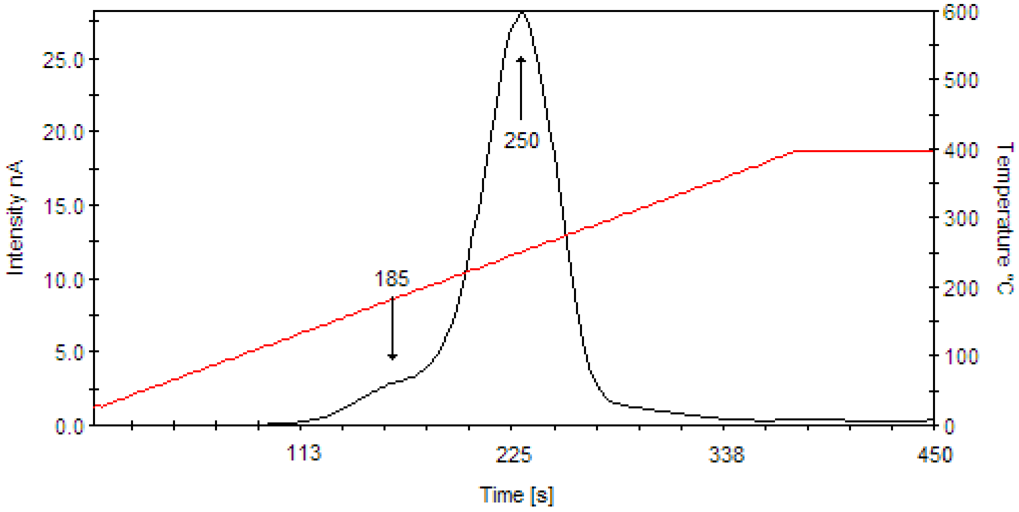

Figure 15. TL glow curve for $Li_2B_4O_7$:^{10}B above room temperature prior to neutron irradiation. The crystal was not exposed to any x-ray radiation or other ionizing radiation deliberately.

4.1.4 Gamma Ray Spectroscopy (GRS) Pre-Neutron Irradiation

Gamma-ray spectroscopy of the pre-neutron irradiated crystals yielded a wealth of information on radioactive impurities. The $Li_2B_4O_7$:Mn and $Li_2B_4O_7$:Ag crystals had been previously neutron irradiated, although at least a month had passed since irradiation. Table 2 shows the impurities noted in each type of crystal. The only crystal that showed activity was the $Li_2B_4O_7$:Ag crystal which showed ^{110m}Ag a long lived meta-stable product of nA.

4.1.5 Neutron Activation

Neutron activation yielded additional information on crystal impurities not previously known to be present in the crystal. Most crystals showed a Sodium-23 impurity. ^{23}Na is likely incorporated into the crystal as Na^{1+} substituting for Li^{1+}. Manganese-55 was noted in the $Li_2B_4O_7$, and $Li_2B_4O_7$:Ag crystals. Platinum was noted in the $Li_2B_4O_7$, and $Li_2B_4O_7$:Ag crystals, and Iridium-191 and 193 was noted in the $Li_2B_4O_7$:Ag crystal. The Pt isotopes were deduced from the presence of ^{198}Au gamma rays. The Pt isotopes can undergo an α capture reaction and yield ^{198}Au. The Pt and Ir impurities are likely due to incorporation of a small amount of crucible material into the crystal during growth. Pt crucibles are used during the growth process, and Ir is a common crucible impurity. The positron annihilation radiation activities were counted for 60 seconds after removal from the nuclear reactor. The 511-keV-gamma-radiation activities are greater than that measured in the same type crystals type prior to neutron irradiation by approximately 200%, while the $Li_2B_4O_7$:^{6}Li crystal yielded 1 million percent more activity (this count include 50% dead time in the detector due to activity level). Note that the crystals used for nA were less than half the size used for GRS. Table 2 shows the impurities noted in each type of crystal.

Table 2. Crystal impurities, bold entries have been identified in both GRS and nA. Star indicates crystals neutron irradiated one month prior to GRS.

Crystal	Impurities GRS	Impurities nA
$Li_2B_4O_7$	None	^{23}Na, ^{55}Mn, ^{195,196}Pt or ^{197}Au 511-keV-gamma 1.5 Bq
$Li_2B_4O_7$:^{6}Li	None	^{23}Na, 511-keV-gamma 500 Bq (50% dead time)
$Li_2B_4O_7$:^{10}B	None	N/A
$Li_2B_4O_7$:Ag*	**^{110M}Ag**	^{23}Na, ^{55}Mn, ^{107}Ag, **^{109}Ag**, ^{191,192}Ir, ^{195,196}Pt or ^{197}Au 511-keV-gamma 1.2 Bq
$Li_2B_4O_7$:Mn*	None	^{23}Na, ^{27}Al, ^{55}Mn, 511-keV-gamma 1 Bq
$Li_2B_4O_7$:Cu	None	^{27}Al, ^{139}La

4.1.6 Electron Paramagnetic Resonance Post-Neutron Irradiation

The EPR spectra collected after neutron irradiation of the crystals was initially conducted without any x-ray radiation. After investigating the crystals without x-ray irradiation, some were x-ray irradiated to determine if other charge traps would populate. All neutron irradiated crystals were investigated with EPR spectroscopy. Most of the crystals showed either little change in the

EPR spectrum, or a very complex post-irradiation spectrum. Those crystals with a very complex post-irradiation spectrum had multiple defects in the same area of the spectrum, and overlaid too much to separate.

Figure 16 shows the EPR spectra of the $Li_2B_4O_7$:^{6}Li crystal after fast neutron irradiation to an interaction density of 10^{15} cm^{-3}. The magnetic field was aligned near the [001] (top spectrum), and the temperature of the spectrum was 12 K. The 7 peak hyperfine structure is centered at 3355 G, with line widths of ~8 G. Other paramagnetic defects were noted in the same area; temperature and orientation were optimized for the best image of the 7 peak hyperfine structure centered at 3355G. The magnetic field was aligned near [100] in the bottom spectrum. The 7 peak hyperfine structure has shifted in the magnetic field to center at 3325 G, line widths are still ~8 G. Also clearly visible in this spectrum is a single broad peak centered at 3370 G. This peak underlies the 7 peak structure when the magnetic field is aligned with the [001]. This single broad peak is also highly temperature sensitive, and grows too much larger intensity at higher temperatures.

Figure 17 shows the EPR spectra of the $Li_2B_4O_7$:^{6}Li crystal after fast neutron irradiation to an interaction density of 10^{15} cm^{-3} after x-ray irradiation at 77 K. The magnetic field was aligned near the [001] (top spectrum), and the temperature of the spectrum was 12 K. Two of the four peaks associated with the O vacancy F center are visible at 3310 G and 3425 G. The 7 peak hyperfine structure is not as intense as before x-ray irradiation, and the line positions are shifted slightly. The magnetic field was aligned near [100] in the bottom spectrum. The 7 peak hyperfine structure is again shifted to center at 3325 G, but the spectrum is distorted by the underlying O vacancy F center peak. Additionally, the broad single peak as 3370 G shows some overlying structure. After annealing at room temperature, the 7 peak hyperfine structure in both orientations returned as before x-ray irradiation.

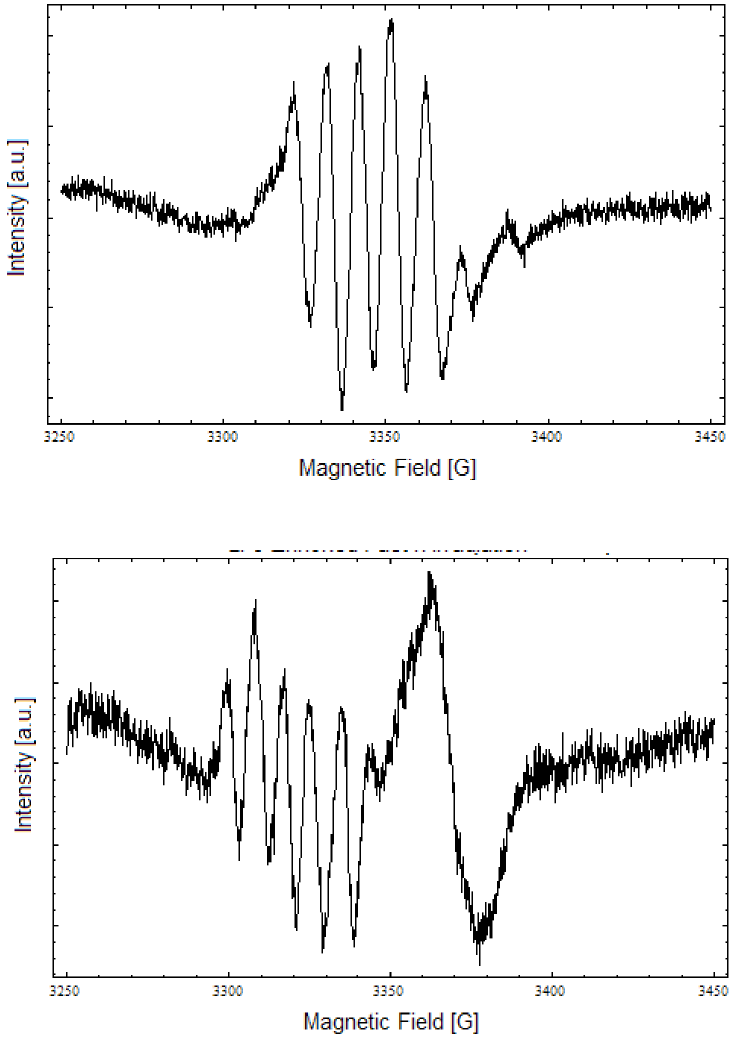

Figure 16. EPR spectra of $Li_2B_4O_7$:^{6}Li fast neutron irradiated to an interaction density of 10^{15} cm^{-3}. The magnetic field is aligned near the [001] top and [100] bottom, the spectra were taken at 12 K.

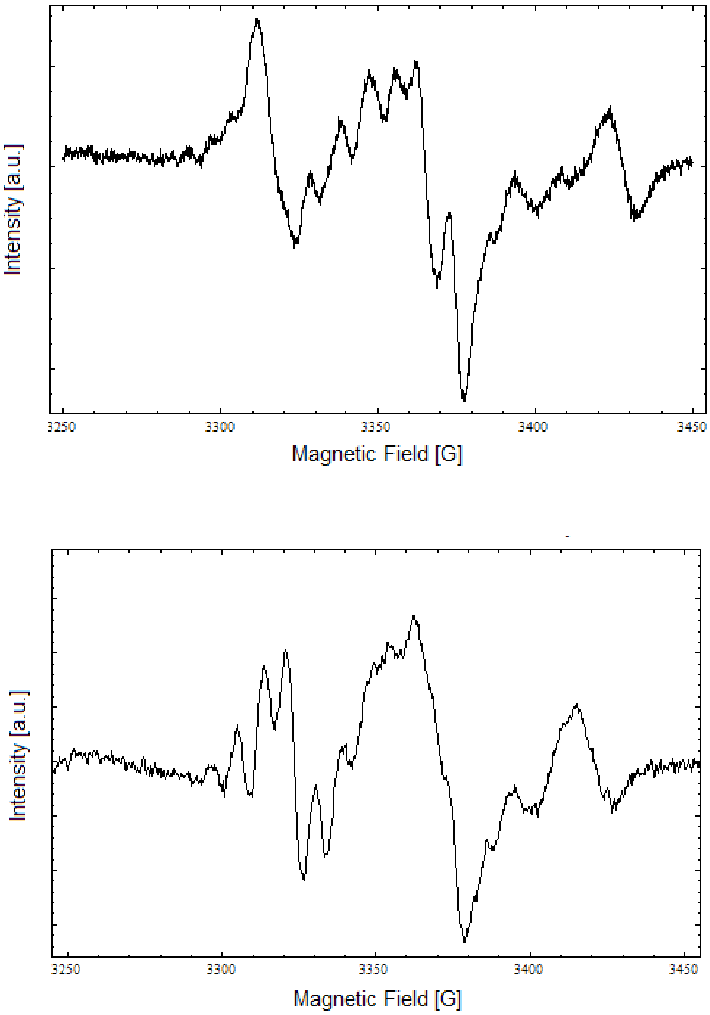

Figure 17. EPR spectra of $Li_2B_4O_7$:^{6}Li fast neutron irradiated to an interaction density of 10^{15} cm^{-3}, x-ray irradiated at 77K The magnetic field is aligned near the [001] (top), [100] (bottom), the spectra were taken at 12 K.

The $Li_2B_4O_7$:^{6}Li crystal neutron irradiated to an interaction density of 10^{17} cm^{-3} with thermal neutrons showed a similar structure at ~3350 G, but other defects present in the same area made the spectrum very challenging to decipher, see Figure 18. There is some temperature dependence to the other structures in that spectrum, and sufficient time with the crystal varying spectra temperature and magnetic field orientations may be able to sort out the nature of those other defects.

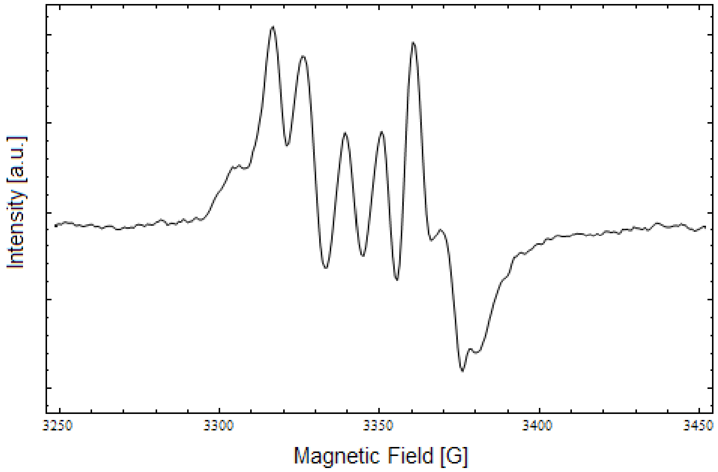

Figure 18. EPR spectra of $Li_2B_4O_7$:^{6}Li thermal neutron irradiated to an interaction density of 10^{17} cm^{-3}. The magnetic field is aligned near the [001], the spectra were taken at 12 K.

Figure 19 shows the EPR spectra of the $Li_2B_4O_7$:^{10}B crystal after thermal neutron irradiation to an interaction density of 10^{17} cm^{-3}. The magnetic field was aligned near the [001], and the temperature of the spectrum was 10 K. The structure is a single broad peak centered at 3365 gauss. The location is not exactly that of the single broad peak on the previous two sets of spectra, but the orientation of this crystal is approximate as well. Of note, the $Li_2B_4O_7$:^{10}B crystal was dark pink to maroon colored after neutron irradiation, where the same crystal was clear and colorless prior to neutron irradiation. Any change in color indicates the production of a new color center, or a new defect type that absorbs all visible light except the noted color.

The $Li_2B_4O_7$ crystal showed a very complex set of overlaid hyperfine structures, and was too complex to unfold. The spectra do suggest that the source of the defects might be discernable with the appropriate amount of time to collect additional EPR spectra. The $Li_2B_4O_7$:Ag crystals that were irradiated in the thermal neutron column to an interaction density of 10^{17} cm^{-3} also showed too much structure to be deconvolved. Understanding of this spectrum could be accomplished with additional experimentation. The $Li_2B_4O_7$:Ag crystals that were irradiated in the 7” tube to an interaction density of 10^{15} cm^{-3} will be discussed with the tertiary research goal.

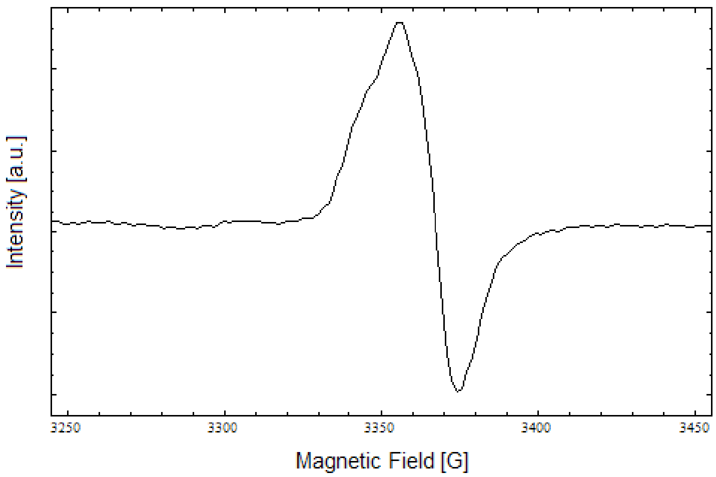

Figure 19. EPR spectrum of $Li_2B_4O_7$:^{10}B thermal neutron irradiated to an interaction density of 10^{17} cm^{-3}. The magnetic field is aligned near the [001], and the spectrum was taken at 10 K.

4.2 Secondary Goal: Thermal Stability of Neutron Induced Defects

TL and limited pulsed anneal were used to determine the thermal stability of EPR identified defects unique to the neutron irradiated crystals. The $Li_2B_4O_7$:Ag with suspected neutron induced defects will be discussed mostly in the section 4.3. The 7 peak hyperfine structure in the $Li_2B_4O_7$:^{6}Li crystal will be presented here. Of note, all defects in undoped crystals after neutron irradiation show significantly different thermal stability than those visible in the EPR spectra of undoped crystals before neutron irradiation. Before neutron irradiation undoped crystals have little to no hyperfine spectra above 90 K. All neutron irradiated crystals were stored at room temperature for several days prior to obtaining EPR spectra.

Post neutron irradiation bulk glow curves were obtained for the $Li_2B_4O_7$:^{6}Li crystal. Figure 33 shows the TL glow curve for the $Li_2B_4O_7$:Ag crystal above room temperature after thermal neutron irradiation to an interaction density of 10^{15} cm^{-3}. Figure 20 shows the TL glow curve for the $Li_2B_4O_7$:^{6}Li above room temperature after thermal neutron irradiation to an interaction density of 10^{15} cm^{-3}. Three glow peaks at 135, 185, 250 and 350 ºC with relative intensities of 1:2:6:3 are observed.

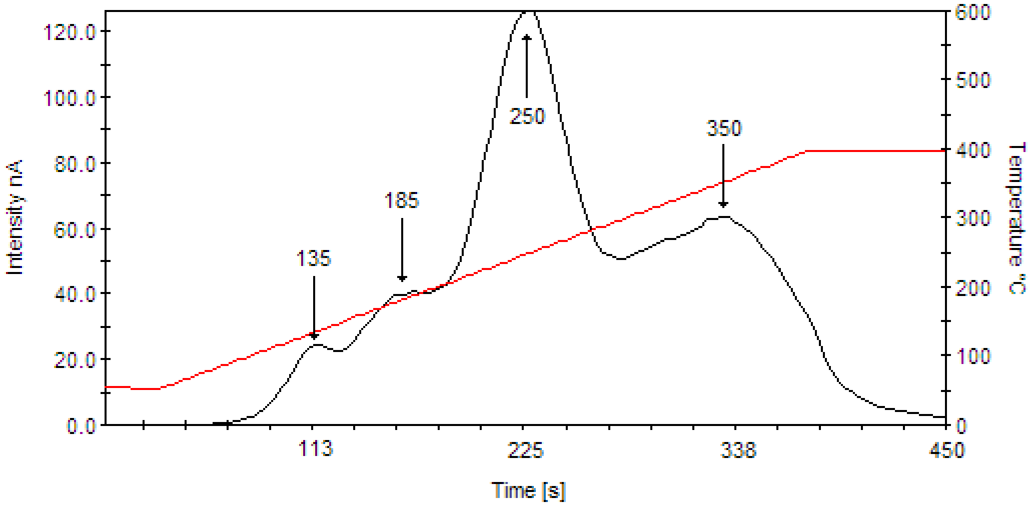

Figure 20. TL glow curve for $Li_2B_4O_7$:^{6}Li above room temperature post thermal-neutron irradiation to a interaction density of 10^{15} cm^{-3}.

Figure 21 shows the TL glow curve for the $Li_2B_4O_7$:^{6}Li above room temperature after fast neutron irradiation to an interaction density of 10^{15} cm^{-3}. Multiple glow peaks are observed at 150, 175, 200, 225, and 250 ºC with multiple smaller peaks at higher temperatures. Furthermore, the 150 ºC peak has a prominent shoulder at lower temperature, and the 200 ºC peak has a prominent shoulder at higher temperature. The relative intensities of the identified peaks are 1:0.9:1.2:0.9:1. Figure 22 shows the TL glow curve for the $Li_2B_4O_7$:^{10}B above room temperature after thermal neutron irradiation to an interaction density of 10^{17} cm^{-3}. Multiple glow peaks are observed at less than 100 ºC, and at 185, 250, 350, and 400 ºC. The relative intensities of the identified peaks greater than 100 ºC are 1:0.66:1.66:5.

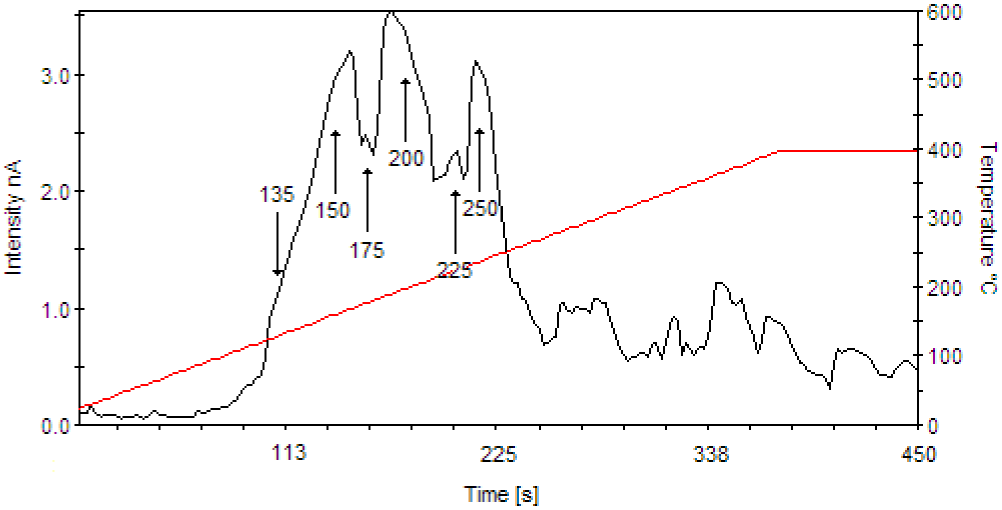

Figure 21. TL glow curve for $Li_2B_4O_7$:^{6}Li above room temperature post fast neutron irradiation to a interaction density of 10^{15} cm^{-3}.

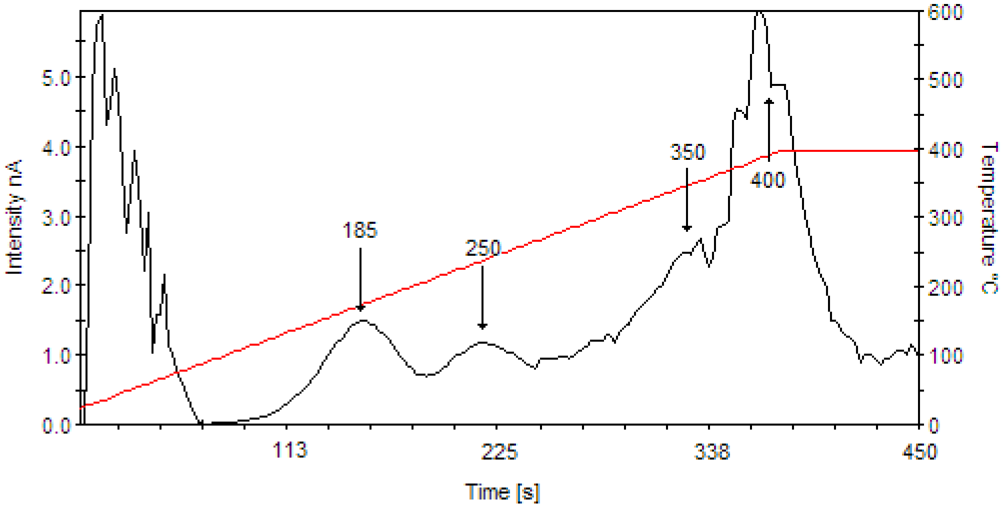

Figure 22. TL glow curve for $Li_2B_4O_7$:^{10}B above room temperature post thermal neutron irradiation to a interaction density of 10^{17} cm^{-3}.

4.3 Tertiary Goal: Ag Doped $Li_2B_4O_7$

The tertiary goal of characterizing the as-grown defects in $Li_2B_4O_7$:Ag was initially begun to characterize as-grown defects, and as a familiarization with the EPR/ENDOR techniques required for completion of the primary research objective. The decision to study neutron irradiated Ag doped crystals was made later. The neutron irradiation of the $Li_2B_4O_7$:Ag crystal was accomplished during irradiation of the isotopically enriched crystals. The results of the neutron irradiation aided in the understanding of the as-grown defects, and will be partially presented here.

4.3.1 Electron Paramagnetic Resonance Pre-Neutron Irradiation

EPR spectra of the pre-neutron irradiated $Li_2B_4O_7$:Ag crystal were obtained at various temperatures, with x-ray irradiation at both 77 K and room temperature, and with multiple magnetic field orientations. Spectra presented here are representative of the multitude of spectra obtained. Figure 23 shows the EPR spectrum for $Li_2B_4O_7$:Ag at 30 K with the magnetic field aligned at [001]. The crystal was x-ray irradiated at room temperature, ~293 K, to populate charge traps prior to obtaining the EPR spectrum.

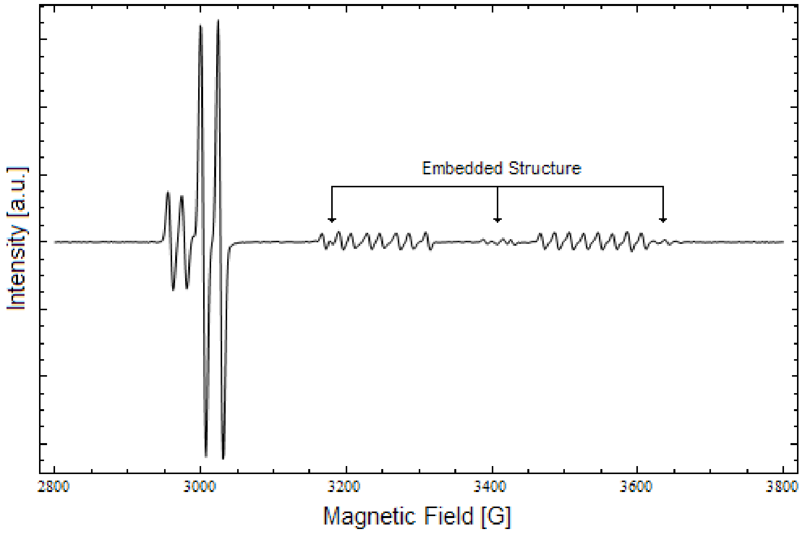

Figure 23. EPR spectrum of $Li_2B_4O_7$:Ag the magnetic field is aligned with the [001]. The spectrum was taken at 30 K. The crystal was x-ray irradiated at room temperature to populate charge traps.

The spectrum shows four hyperfine structures. The first centered at 2960 G is a doublet. The second centered at 3010 G is also a doublet. The peak separation in the first doublet is ~19 G and in the second doublet is ~25 G. The relative intensity of the two doublets is 1:4 (2960 G : 3010 G). The third feature is a 16 peak structure divided in two groups of eight fairly widely spaced centered at 3380 G. The last features are visible between the two eight peak bundles of the 16 peak structure, off the right side of the 16 peak structure, and inside the first and second peak of the 16 peak structure. This embedded structure had low intensity, and could not be characterized.

Figure 24 shows the EPR spectra for $Li_2B_4O_7$:Ag at 45 K (top) and, 15 K (bottom) with the magnetic field aligned at [001]. The crystal was x-ray irradiated at 77 K after a full anneal of trapped charges, 673 K for 20 minutes. The doublet at 2960 G is not in this spectrum. Based on these observations, and PA studies, the doublet at 2960 G is thought to have a competitive relationship with the O vacancy F center. Later discussion will directly address this relationship. The second doublet centered at 3010 G is unchanged. The 16 peak structure centered at 3380 G is unchanged. The unresolved features previously embedded in the 16 peak structure are not visible. There are two structures embedded in the 16 peak structure centered at 3380 G (top spectrum) not visible with room temperature x-rays. These correspond to the Li vacancy V_1 center and the O vacancy F center seen in undoped crystals. The Li vacancy V_1 center is now visible when it was not after room temperature x-ray irradiation because at room temperature, the Li vacancy V_1 center is not stable (M. Swinney March, 2009, 64). The reasons for the appearance of the O vacancy F center are not as simple, and are discussed in conjunction with the PA studies of Li2B4O7:Ag in chapter 5.3. These are more easily seen in the bottom spectrum in which the 16 peak structure centered at 3380 G is microwave power saturated, and not visible. Also note, at 10 K the doublet centered at 3010 G increases in amplitude to off scale; two good examples of the temperature dependence of hyperfine spectra.

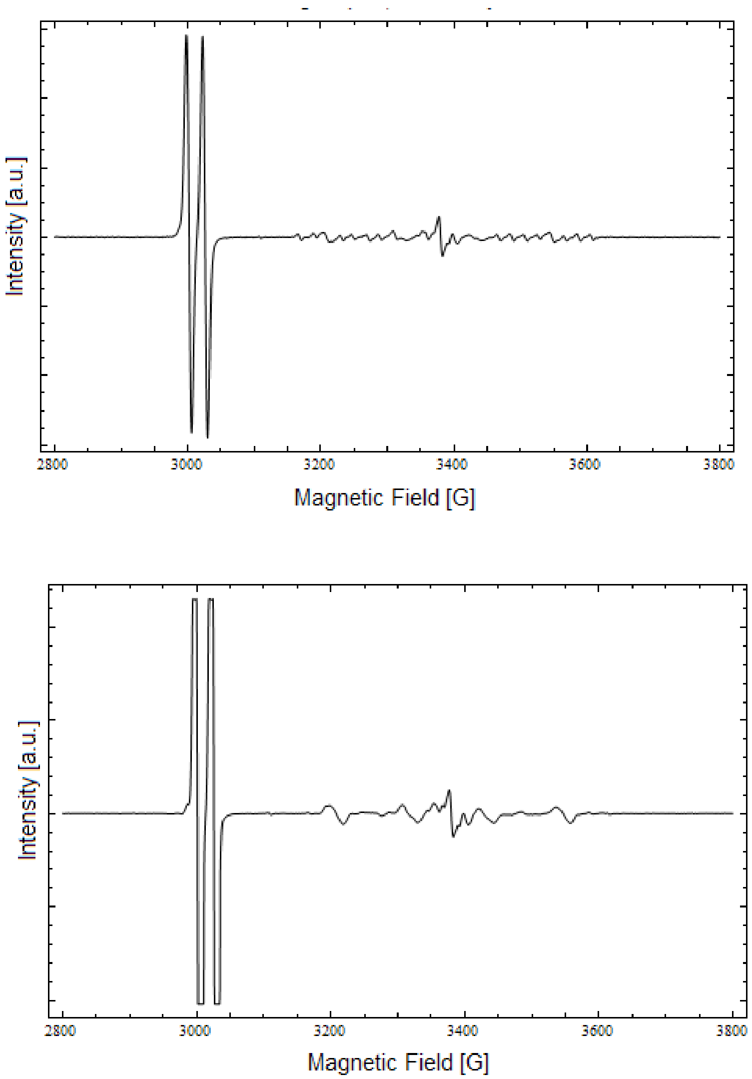

Figure 24. EPR spectra of $Li_2B_4O_7$:Ag the magnetic field is aligned with the [001]. The spectra were taken at 45 K (top), 15 K (bottom). The crystal was x-ray irradiated at 77K after a full anneal of trapped charges.

4.3.2 Electron-Nuclear Double Resonance (ENDOR)

Figure 25 shows the ENDOR spectrum of the pre-neutron irradiated $Li_2B_4O_7$:Ag crystal taken at the position of the lower peak in the doublet located at 3010 G. The spectrum was taken at 15 K with the magnetic field aligned with [001]. The spectrum shows two doublets centered at 35.7 MHz, and 41.3 MHz. Setting these values equal to ½ A gives hyperfine coupling values of

22.9 G and 26.4 G. These values compare favorably with the value of 25 G estimated from the EPR spectrum. The ν_N values for the lower frequency doublet is 0.43 MHz, which compares favorable for the known values of 0.52 MHz for ^{107}Ag. The ν_N values for the upper frequency doublet is 0.49 MHz, which compares favorable for the known values of 0.59 MHz for ^{109}Ag. This agreement confirms that the 3010 G doublet in the EPR spectrum and these two doublets are due to the Ag isotopes.

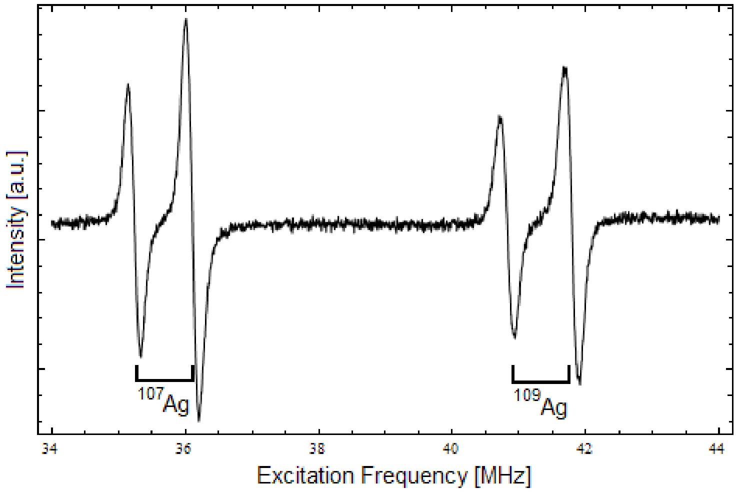

Figure 25. ENDOR spectrum of $Li_2B_4O_7$:Ag the magnetic field is aligned with the [001]. The spectrum was taken at 15 K. The crystal was x-ray irradiated at room temperature. The magnetic field was set to the lower peak of the 3310 G doublet.

4.3.3 Pulsed Anneal Pre-Neutron Irradiation

PA of the $Li_2B_4O_7$:Ag crystals were conducted from room temperature (300 K) to 523 K after room temperature x-ray irradiation, and from 77 K to 523 K, after 77 K x-ray irradiation. The data presented is for PA subsequent to x-ray irradiation at 77 K. PA subsequent to x-ray irradiation at room temperature does not differ significantly. Figure 26 shows the EPR spectra for $Li_2B_4O_7$:Ag at 15 K with the magnetic field aligned at [001]. The crystal was x-ray irradiated at 77K after a full anneal of trapped charges, 673 K for 20 minutes. The top spectrum shows the changes due to 90 K anneal for 3 minutes. Note the Li V_1 center no longer appears, and the O vacancy F center remains unchanged. The Ag related doublet at 3310 G remains unchanged, and the Ag related doublet at 2960 still does not appear. The bottom spectrum shows the same crystal after a subsequent anneal at room temperature for 3 minutes. Note the O vacancy F center is significantly annealed but not completely. The Ag related doublet at 3310 G remains unchanged. The Ag related doublet at 2960 G has appeared in the spectrum, but the ratio 2960 G : 3310 G is only 1:6. The 16 peak Ag related feature at 3380 G has increased in intensity as well.

Also note that the low intensity features that have previously resided between and around the 16 peak Ag related feature are no longer visible. This crystal was repeatedly annealed at 673 K to fully anneal trapped charges between repetitions of the PA study. This has completely annealed the defects responsible for these low intensity features. This indicates that the embedded structure may be due to interstitial defects that anneal at or below 673 K.

Figure 27 shows the relative intensity of the various paramagnetic species in the $Li_2B_4O_7$:Ag crystal during the PA study from 77 K to 523 K. The figure corresponds to the EPR spectra described above. All defects were normalized to a 5 G line width, and each species intensity was presented relative to its own maximum. The Li vacancy V_1 center anneals completely by 90 K. The O vacancy F center begins annealing above 90 K and is completely annealed by 373 K. The O vacancy F center is 50% annealed at ~270 K.

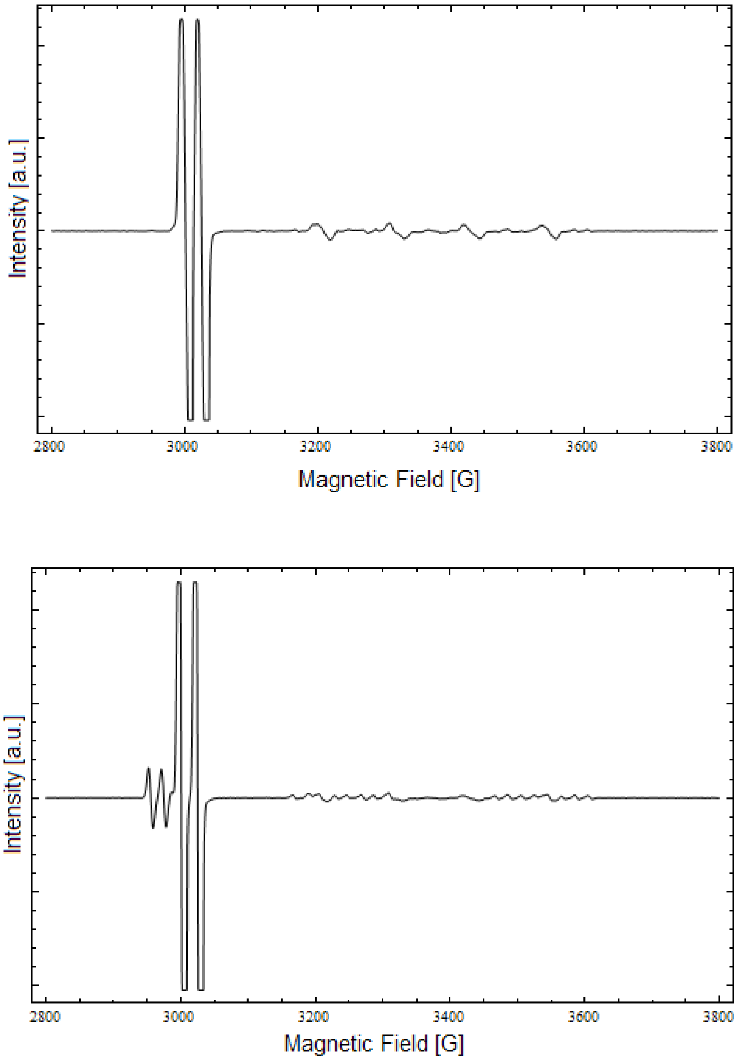

Figure 26. EPR spectra of $Li_2B_4O_7$:Ag the magnetic field is aligned with the [001]. The spectra were taken at 15 K. The crystal was x-ray irradiated at 77 K after a full anneal of trapped charges. The top spectrum shows the EPR spectrum after a 3 min. 90 K anneal. The bottom spectrum shows the EPR spectrum after a 3 min. room temperature anneal.

At this same temperature, the Ag related doublet centered at 2960 G is 50% populated. The 2960 G doublet reaches its maximum intensity at 373 K, the same point the O vacancy F center is 100% annealed. Not shown, the 16 peak Ag related structure centered at 3380 G increases somewhat over this same period. The Ag related doublet centered at 3310 G begins to anneal above 90 K thru 373 K like the O vacancy F center. Above 373 K the doublet anneals at a much higher rate.

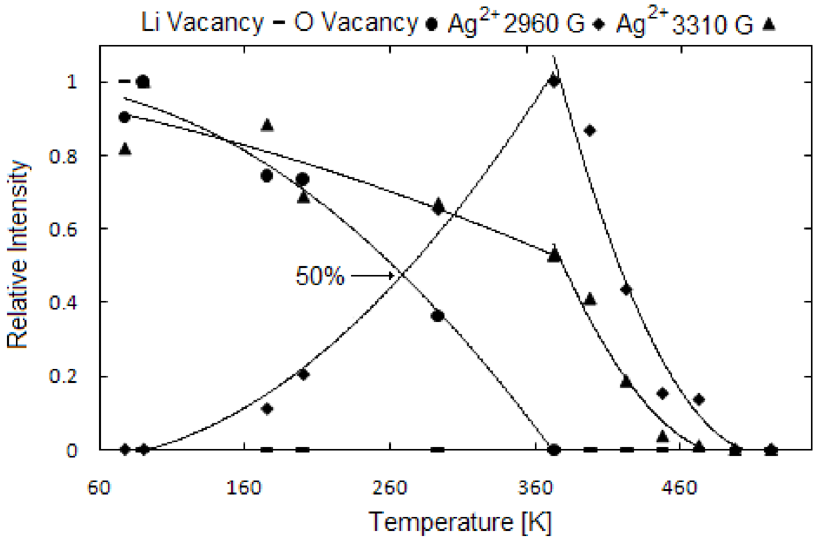

Figure 27. Pulsed anneal of $Li_2B_4O_7$:Ag after 77 K x-ray irradiation. The Li V_1 center anneals by 90 K. Each paramagnetic species was normalized to a 5 G line width, and displayed relative to its own maximum intensity. The 50% comment shows the common point at which the O vacancy F center has annealed 50%, and the Ag related doublet at 2260 G has grown from zero intensity to 50% maximum. Lines are simply references to connect data point of the same species; the shapes of the lines are arbitrary.

Figure 28 shows the same pulsed anneal as shown in Figure 27. However, Figure 28 shows the normalized defects intensity in arbitrary units not relative units. There is no difference in the thermal stability of the paramagnetic species, but this figure allows evaluation of the total number of trapped holes and electrons annealed. Up to 373 K the decrease in the O vacancy F center compares favorably with the sum of the increase of the Ag neutral defects (16 peak Ag related structure centered at 3380 G) and the decrease on the Ag^{2+} defect (Ag related doublet centered at 3310 G). This shows charge balance can be maintained in the crystal throughout this annealing period without invoking a hidden defect. Above 373 K the decrease in the trapped holes is an order of magnitude greater than the decrease in trapped electrons. The charge balancing in this case may be maintained by trapped electrons in the crystal that are not trapped on paramagnetic species.

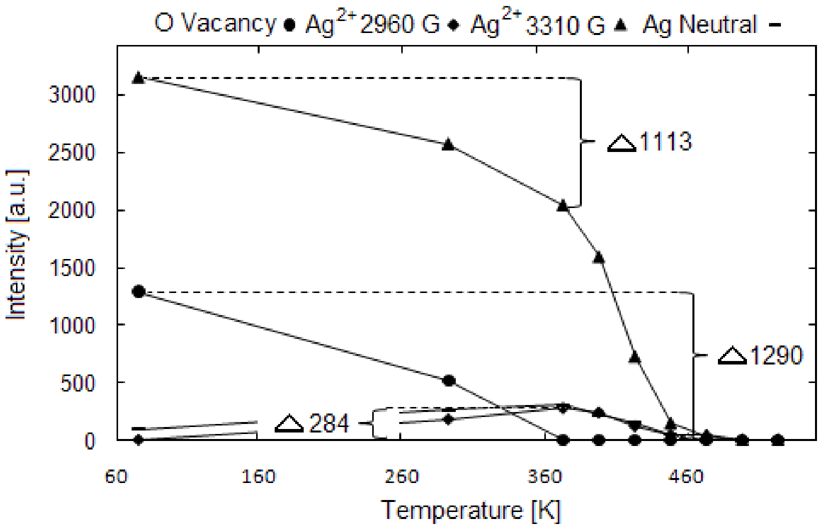

Figure 28. Pulsed anneal of $Li_2B_4O_7$:Ag after 77 K x-ray irradiation. The Li V_1 center intensity is too small to resolve. The Δ comments show the change in intensity for each paramagnetic defect. The intensity of each defect has been normalized to a 5 G line width.

4.3.4 Thermoluminescence Pre-Neutron Irradiation

In 2009 Swinney showed TL emission from the $Li_2B_4O_7$:Ag crystal between 77K and room temperature after x-ray irradiation at 77 K (M. Swinney March, 2009, 60). This TL emission is likely due to the annealing of the O vacancy F center, and the Ag related doublet at 3310 G. The TL glow curve of the $Li_2B_4O_7$:Ag crystal was accomplished with a heating rate of 1 ºC per second. This profile is the slowest heating rate available on the Harshaw TLD reader, but is four times the estimated ¼ ºC heating rate for the pulsed anneal. The increased heating rate should push glow peaks higher in temperature than they would be at the ¼ ºC per second heating rate. This shift in the glow peak is responsible for the slight miss-alignment between the TL glow curve and the PA study.

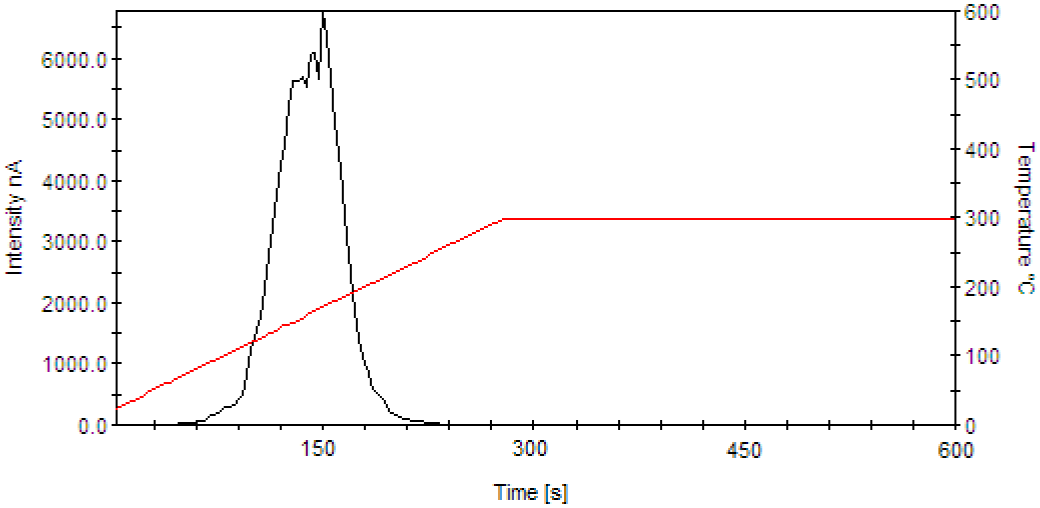

Figure 29. TL glow curve for $Li_2B_4O_7$:Ag above room temperature prior to neutron irradiation. The crystal was exposed to 60keV, 30 mA x-ray radiation at room temperature to populate Ag related charge traps.

Figure 29 shows the above room temperature bulk glow curve for $Li_2B_4O_7$:Ag. The crystal was deliberately exposed to x-ray at room temperature to populate charge traps. There is one bulk glow peak at 150 °C. None of the glow peaks from the $Li_2B_4O_7$:^{6}Li crystals, neutron irradiated or not, are seen in this TL spectrum.

4.3.5 Electron Paramagnetic Resonance Post-Neutron Irradiation

Two $Li_2B_4O_7$:Ag crystals were neutron irradiated with thermal neutrons. The crystals were irradiated to a thermal neutron interaction density of 10^{15} cm^{-3} and 10^{17} cm^{-3}. After irradiation, EPR spectra of the neutron irradiated crystals were obtained at various temperatures with the magnetic field aligned with the [001]. The spectra presented are from the crystal irradiated to an interaction density of 10^{15} cm^{-3}. The spectrum of the other crystal was too complex to deconstruct without further data collection. X-ray irradiation of the crystals at 77 K and room temperature and subsequent EPR spectroscopy has not been completed. If neutron induced defects were particularly unstable, the process of x-ray irradiation and anneal may have annealed neutron induced defects before TL studies were able to be conducted. The x-ray irradiation studies should still be completed to more fully examine the crystals.

Figure 30 shows the EPR spectrum of $Li_2B_4O_7$:Ag with the magnetic field aligned with the [001]. The spectrum was taken at 12 K. The crystal was neutron irradiated to an interaction density of 10^{15} cm^{-3}. The crystal was not x-ray irradiated prior to obtaining the spectrum. The Ag related doublets centered at 2960 G and 3310 G are still visible in the spectrum. Now, however, the intensity ratio of the resonances at 2960 G : 3310 G is only 1:20. The 3310 G doublet is roughly the same intensity; the 2960 G doublet is significantly reduced in intensity. X-ray irradiation studies would be definitive in determining if this observation is significant or simply a function of the crystal temperature during neutron irradiation. The Ag related 16 peak structure centers at 3380 G is still visible in the spectrum, and not significantly changed in intensity. The previously low intensity features in and around the 16 peak structure are much greater in intensity post neutron irradiation.

The bottom spectrum in Figure 30 shows the structure of the previously low intensity features, and one new feature. There is a sharp single peak at 3365 G, a four peak structure centered at 3395 G, a six peak structure composed of two broadly spaced sets of three peaks centered at 3395 G, and a new low intensity feature near 3320 G. Close inspection of Figure 31 shows that all but the new low intensity feature near 3320 G are simply enhanced intensity of the previously low intensity features previously observed amongst the 16 peak structure centered at 3380 G.

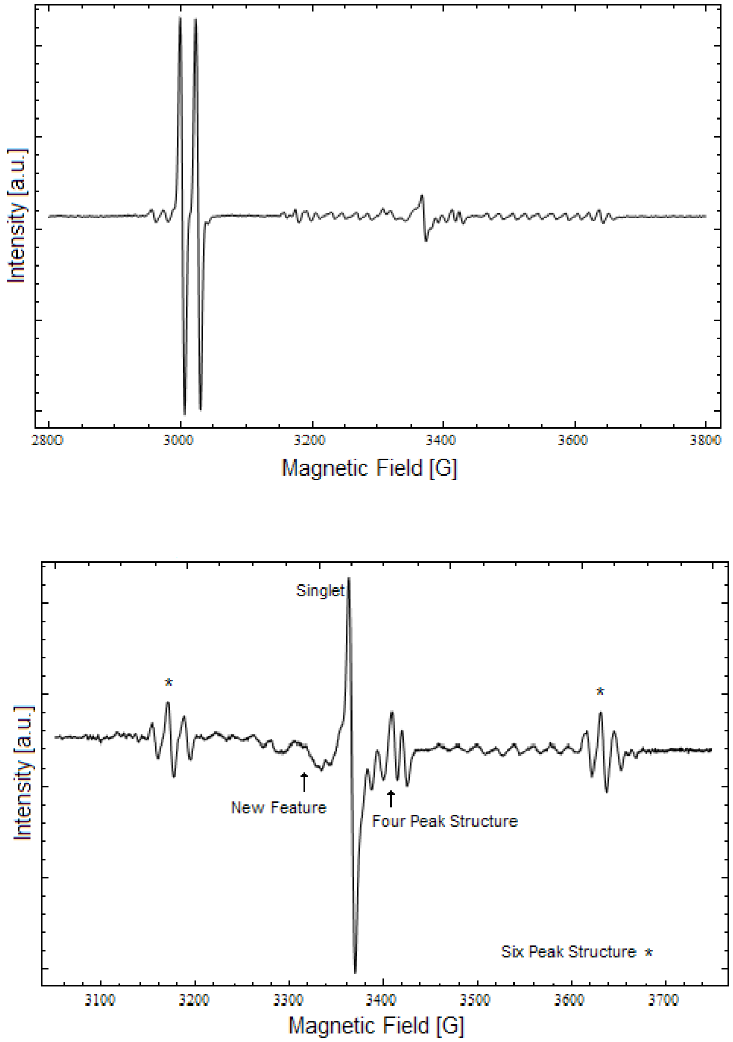

Figure 30. EPR spectrum of $Li_2B_4O_7$:Ag the magnetic field is aligned with the [001]. The spectrum was taken at 12 K. The crystal was neutron irradiated to a defect density of 10^{15} cm^{-3}. Bottom spectrum is an enhancement of the region between 3050 – 3750 G. Bottom spectrum was also annealed at 150 °C for 20 minutes to accentuate the new hyperfine structures.

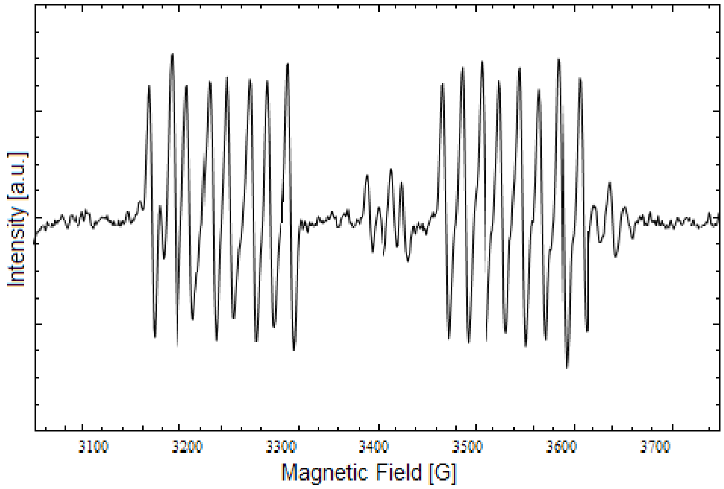

Figure 31. EPR spectrum of $Li_2B_4O_7$:Ag the magnetic field is aligned with the [001]. The spectrum was taken at 30 K. The crystal was x-ray irradiated at room temperature to populate charge traps. Spectrum is an enhancement of the region between 3050 – 3750 G.

4.3.6 Pulsed Anneal Post-Neutron Irradiation

Pulsed anneal of the $Li_2B_4O_7$:Ag showed that the neutron induced paramagnetic defects had greater thermal stability than the as-grown defects. The neutron induced defects remained unchanged in intensity over a 3 minute anneal step at 180 ºC and showed some change over an anneal step at 205 ºC. By 205 ºC all of the as-grown defects in $Li_2B_4O_7$:Ag are significantly annealed. The neutron induced defects showed greater thermal stability. After annealing, the crystal was x-ray irradiated, and all defects were once again populated. Figure 32 shows the hyperfine spectra after annealing steps. Note that as the as-grown defects anneal, the defects induced by neutron irradiation increase in intensity, in particular, the singlet centered at 3365 G.

4.3.7 Thermoluminescence Post-Neutron Irradiation

Post neutron irradiation bulk glow curves were obtained for the $Li_2B_4O_7$:Ag crystal. The $Li_2B_4O_7$:Ag crystal was prepared for TL by undergoing a 150 ºC anneal for 20 minutes. This anneal did not change the intensity of the neutron induced defects noticeably, but almost completely anneal the charges trapped in the as-grown defects.

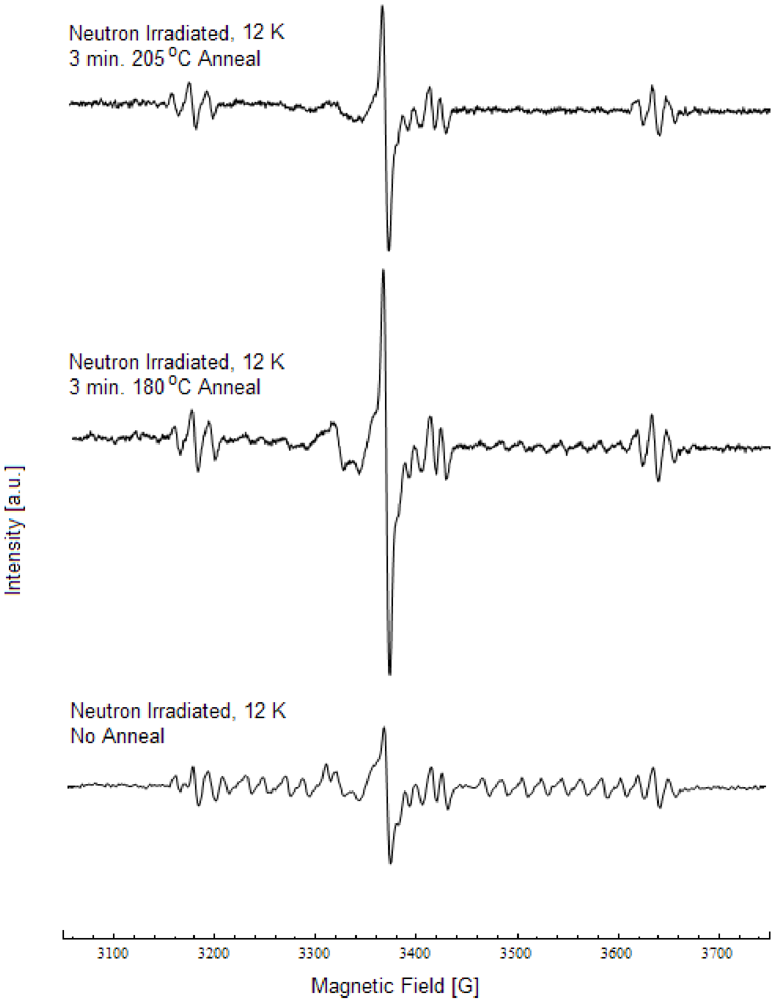

Figure 32. EPR spectra comparison post neutron irradiation $Li_2B_4O_7$:Ag. The bottom spectrum is the crystal prior to any annealing. The center spectrum is after a 3 minute 180 ºC anneal. The top spectrum is after a 3 minute, 180 ºC anneal. The magnetic field is aligned with the [001].

Prior to the 150 ºC anneal, the crystal was green colored which is typical for $Li_2B_4O_7$:Ag crystals after x-ray irradiation. After the 150 ºC anneal the crystal was orange colored. This coloring has not been seen in other crystals to-date. This change in coloration suggests that an absorption measurement might provide additional insight in to the nature of the neutron induced defects. Multiple peaks are observed between 150 and 300 ºC not observed in the pre-neutron irradiation TL bulk glow curve. Additionally, the continuation of the glow curve into the 300 ºC periods, see Figure 33, suggests that the time temperature profile should be adjusted to heat to 350 ºC prior to stopping to fully develop the upper part of the glow curve. Adjustments to the time-temperature profile require x-ray irradiation of the sample crystal and collection of new glow curves not yet complete. Collection of new glow curves at temperatures exceeding 300 ºC might anneal interstitial defects completely making further study of the same defects with EPR impossible. Collection of new glow curves with adjusted time temperature profiles to exceed 300 ºC are expected to show glow peaks at 350 ºC and/or 400 ºC like the undoped crystals.

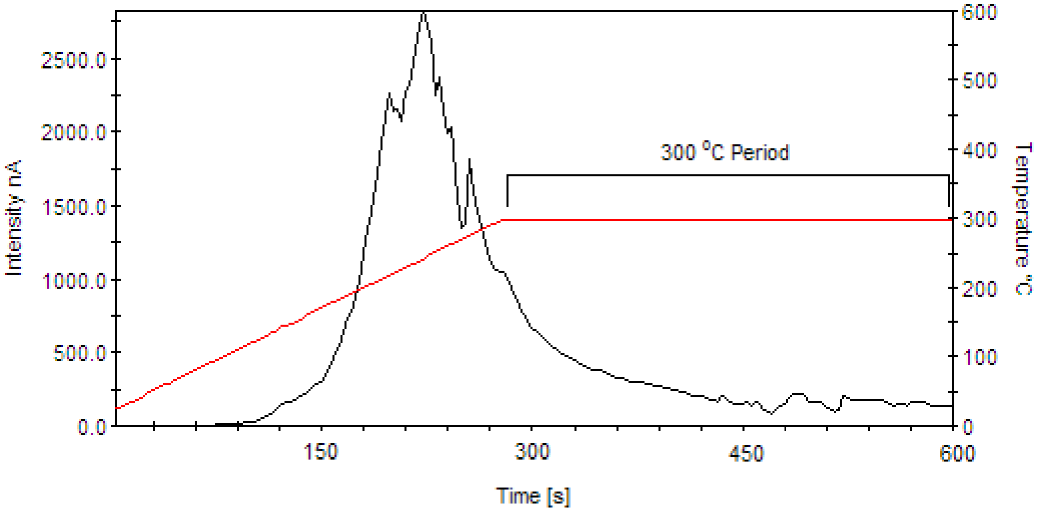

Figure 33. TL glow curve for $Li_2B_4O_7$:Ag above room temperature after neutron irradiation. The crystal was annealed at 150 °C for 20 minutes prior to obtaining TL glow curve to anneal charges trapped on as-grown Ag related defects.

4.3.8 Angular Dependent EPR Spectra

EPR spectra were obtained of the $Li_2B_4O_7$:Ag crystal with the magnetic field aligned along [001], [100], [110], and near [011]. Focus was placed on the Ag related doublet centered at 3310 G.

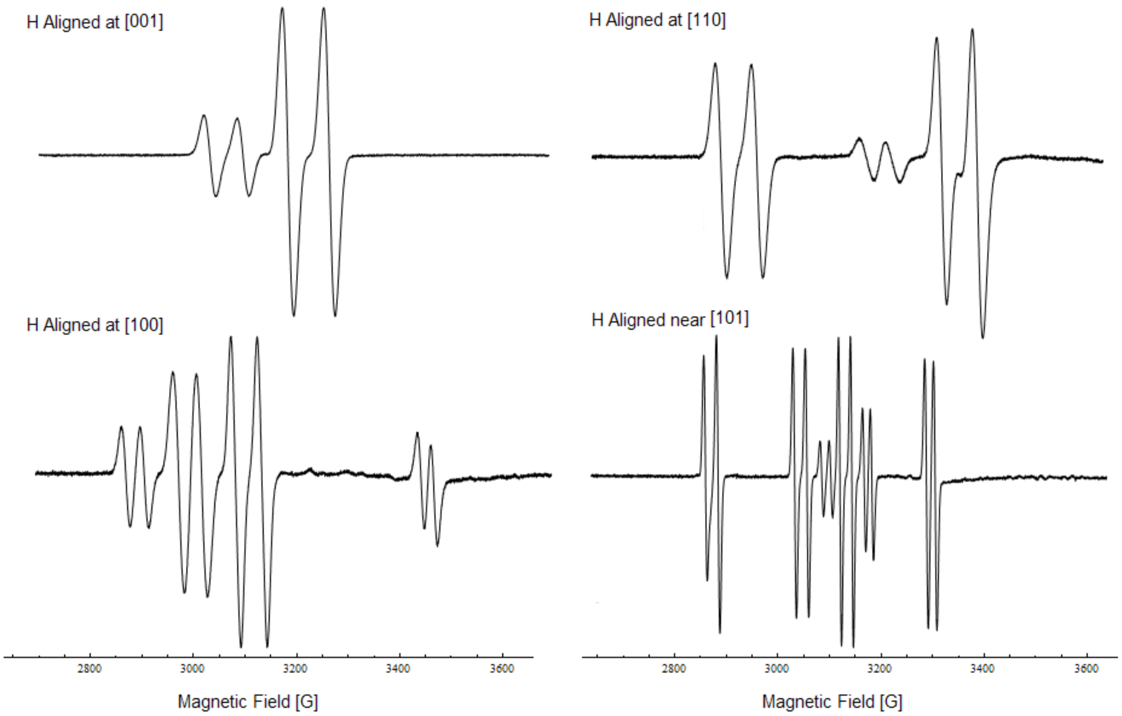

Figure 34. EPR Angular dependence study of the Ag related doublet centered at 3310 G. The EPR spectra were taken at 15 K with magnetic field alignments as noted in the figure.

Figure 34 shows the EPR spectra of the Ag related doublet centered at 3310 G in four magnetic field orientations. In the upper left spectrum, the magnetic field is aligned with the [001] as in all previous spectra. The 3310 G centered doublet is obvious as well as the doublet centered at 2960 G. The [001] is crystallographically the most unique orientation. All Li sites, and substituted Ag, sites are equivalent. In the lower left spectrum, the magnetic field is aligned with the [100]. The [100] is crystallographically unique, but not all Li sites are equivalent in this orientation. There are two possible orientations with respect to the magnetic field at [100], and the doublet centered at 3310 G at [001] is split into two doublets one centered at 3110 G and one centered at 3000 G. Away from the [001], not all Li sites are energetically equivalent, but are equivalent under rotation. In the upper right spectrum, the magnetic field is aligned with the [110]. The [110] direction is a high symmetry direction, and there are two possible orientations for the Li site with respect to the magnetic field. The 3310 G centered doublet from the [001] orientation will again split into two doublets, one centered at 3210 G and one centered at 3080 G. In the lower right spectrum, the magnetic field is aligned near the [101]. The [101] is not a high symmetry direction like the other three, but it is in one of two high symmetry planes. The (001) and the (100) are high symmetry planes. The (010) is equivalent to the (100), and the [010] is equivalent to the [100]. In the high symmetry planes, there are four possible orientations for the Li site to the magnetic field. The 3310 G centered doublet from the [001] is split into four doublets, each centered at 2877 G, 3048 G, 3136 G and 3304 G. Away from one of the high symmetry direction or planes, there are 8 possible orientations of the Li site to the magnetic field, and the doublet will split into 8 doublets.

4.4 Fourth Goal: Positron Annihilation

During the nA studies, a significant amount of 511 keV positron annihilation gamma radiation was noted. Positron emitting isotopes are generally short lived; therefore the annihilation radiation was most likely a result of the neutron irradiation. Outlined in Equations 3, 4, and 5 in chapter 2.2 the production schemes for positron emitting isotopes are a possible explanation for the occurrence of positron annihilation after neutron irradiation. . Pair production resulting from interaction of >1.2 MeV gamma rays in a high Z material might also produce positron annihilation gamma radiation. The source of the >1.2 MeV gamma rays would be the relaxation of excited nuclear states induced by gamma or neutron bombardment in the OSURR or the AFIT pile. This possibility is discounted going forward, because of the apparent half life of the source of the positron annihilation radiation. The half life of nuclear excited states is generally on the femto-second time scale. All excited nuclei should have long decayed prior to the irradiated crystals reaching the HPGe detectors.

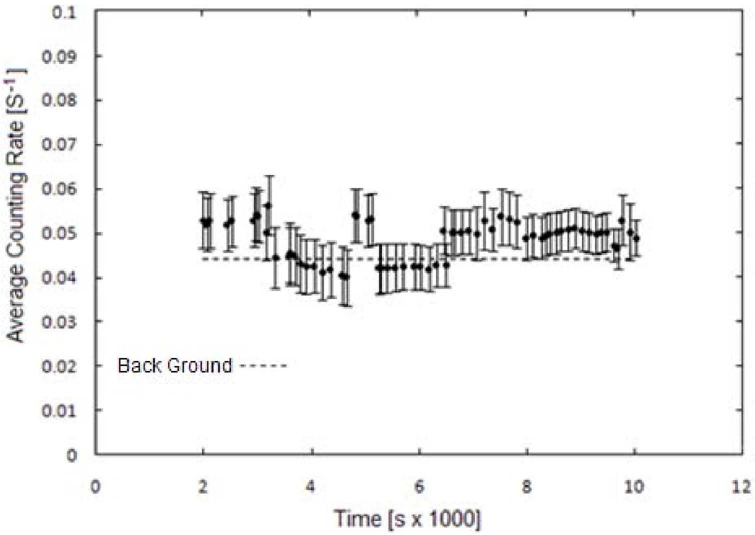

Figure 35. Average 511 keV gamma radiation count rate for $Li_2B_4O_7$:^{10}B after n irradiation in the AFIT pile to secular equilibrium. The dashed line is the average count rate pre-neutron irradiation for 511 keV gamma radiations.

Both $Li_2B_4O_7$:^{6}Li and $Li_2B_4O_7$:^{10}B crystals were neutron irradiated in the AFIT thermal pile drawer three long enough that all positron possible production reactions for positron annihilation radiation would be at secular equilibrium. Each crystal was then removed from the pile and taken to the HPGe detector and the GRS was obtained. The crystal reached the HPGe detector and counting was begun within two minutes of removal from the pile. Peak fitting was conducted at regular intervals to determine the total number of counts at 511 keV with respect to time. From these regular count totals an average activity for the 511-keV-energy-peak was calculated at each measurement time and plotted. This was compared to the average count rate of the same type crystal prior to neutron irradiation, and a theoretical calculation of additional activity produced by the possible positron emitting isotopes. The average activity for an isotope with respect to time was modeled by (Krane 1988, 164),

$$\overline{A}(t) = \frac{N_0\left(1 - e^{\lambda t}\right)}{t} \tag{11}$$

Where $\overline{A}$ is the average count rate, N_0 is the number of atoms of the radioactive isotope at time zero, λ is the decay constant, and t is the time since removal from the pile. By analyzing the average activity with respect to time, the positron emitting species can be determined. The disparity in half life length between ^{15}O and ^{18}F would give very different activity vs. time plots. ^{15}O would produce a curve which decays much more rapidly than that of ^{18}F.

Figure 35 shows the average count rate for 511-keV-gamma-rays after neutron irradiation of the $Li_2B_4O_7$:^{10}B crystal compared with detector 511-keV-gamma-ray background. The AFIT pile produced perhaps a slight increase in the activity throughout the time period. The reason for suppression of the average count rate between 3500 and 6500 seconds is not known.

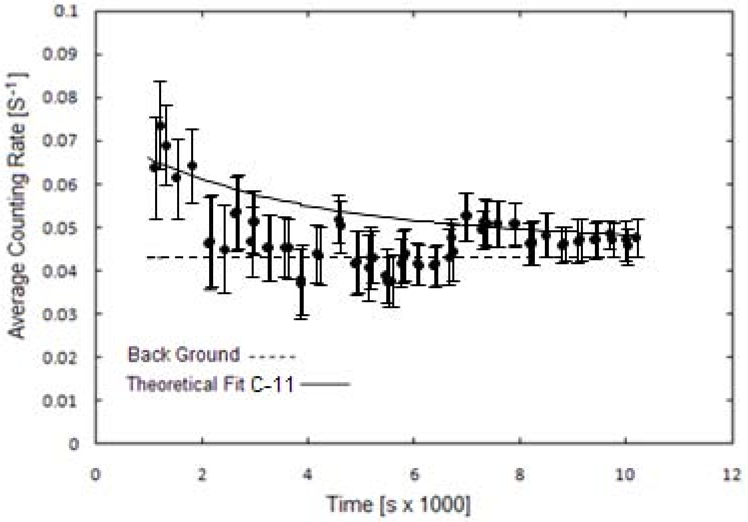

Figure 36. Average 511 keV gamma radiation count rate for $Li_2B_4O_7$:^6Li after n irradiation in the AFIT pile to secular equilibrium. The dashed line is the average count rate pre-neutron irradiation for 511 keV gamma radiations. The solid line is a calculation of the expected average count rate for 511 keV gamma rays given the background counting rate, and a positron emitting isotopes with a half life less than 3 minutes.

Figure 36 shows the average count rate for 511-keV-gamma-rays after neutron irradiation of the $Li_2B_4O_7$:^6Li crystal compared with detector 511-keV-gamma-ray background. The count rate shows, perhaps, a slight increase in count rate over the whole period of counting. The count rate does show an increased average count rate over pre-irradiation up to ~1500 seconds after irradiation. The solid line in the figure is a calculation of the expected average count rate as a linear sum of the pre-irradiation count rate, and one positron emitting isotope with a half-life less of 20.39 minutes. The short lived isotope has the effect of increasing the initial average count rate to fit the time period prior to ~1700 seconds. The short lived isotope will also slightly increase the average count rate thru the whole collection time. Note that the increase in 511-keV-gamma-radiations in the $Li_2B_4O_7$:^{6}Li crystal over the increase in the $Li_2B_4O_7$:^{10}B crystal agrees with the results of the nA study at the OSURR. The 511-keV-gamma-radiation intensity produced in the OSURR is contained in Table 2.

V. Discussion

5.1 Primary Goal: Characterization of Neutron-Induced Defects

Although some spectra obtained after neutron irradiation were too complex to deconstruct, there are three sets of defects that are identifiable and may be neutron induced. The broad single peak in the post neutron irradiated $Li_2B_4O_7$:^{10}B crystal EPR spectrum, Figure 19, is the only feature in the spectrum. In previous work, similar features have been identified as resulting from metallic Li clusters post irradiation (Burak, Padlyak and Shevel 2002, 1103). The cluster would form due to ^{7}Li production in the $^{10}B(n,\alpha)^7Li$ reaction. Heavy neutron irradiation would quickly increase Li beyond the stoichiometric ratio, and a cluster could form. This same feature is evident in spectra from all neutron irradiated crystals. It may not be particularly important in a neutron detection scenario, because it is possible that knock-on type damage could cause the same type of defect, and the detection of low fluences may not be possible with this mechanism.

The seven peak hyperfine structure in the $Li_2B_4O_7$:^{6}Li crystal EPR spectrum, Figure 37, post neutron irradiation shows marked differences form the Li vacancy V_1 center in the as-grown crystal. The neutron irradiated 7 peak hyperfine structure is centered differently than the as-grown Li vacancy Vi center, it has broader line widths compared to the as-grown center, it is more anisotropic than the as-grown center, and it has greater thermal stability than the as-grown center. The as-grown center shows only slight anisotropy, and the neutron irradiated seven peak hyperfine structure shifts down field ~ 30 G moving from [001] to [100].

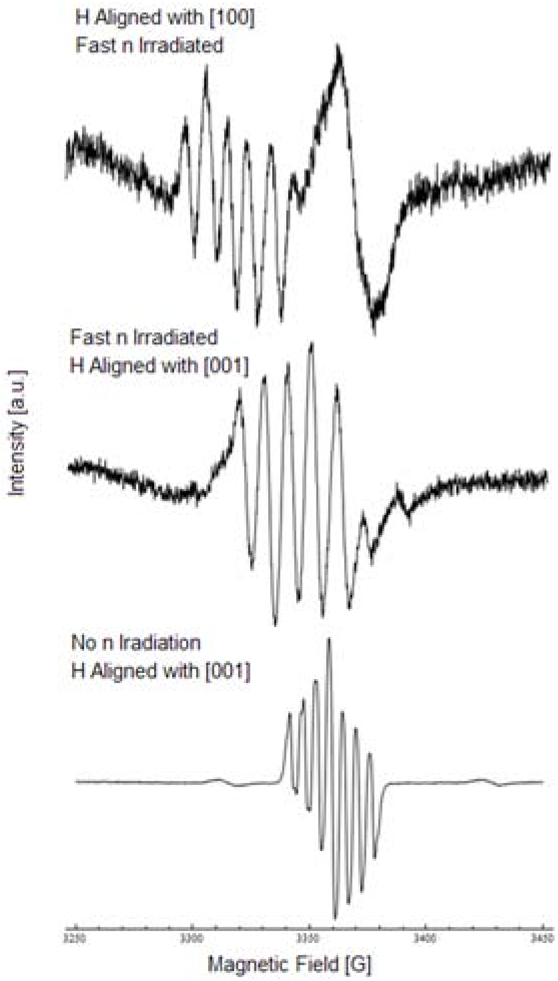

Figure 37. EPR spectra comparison pre and post neutron irradiation for $Li_2B_4O_7$:^{6}Li crystal. EPR spectra for neutron irradiated crystal obtained at 12 K. EPR spectra for pre-neutron irradiated crystal obtained at 77 K.

The as-grown center anneals completely by 90 K, and the neutron irradiated seven peak structure is stable up to at least room temperature. The neutron irradiated seven peak structure is likely a Li vacancy V_1 center perturbed by adjacent defects. In consuming ^{6}Li through nuclear reactions, additional Li vacancy V_1 centers will be produced. The high energy ^{3}H, and α particle produced in the reaction may well induce other defects near the new vacancy. The adjacent defects could stabilize an electron trapped at the defect differently than at an unperturbed site.

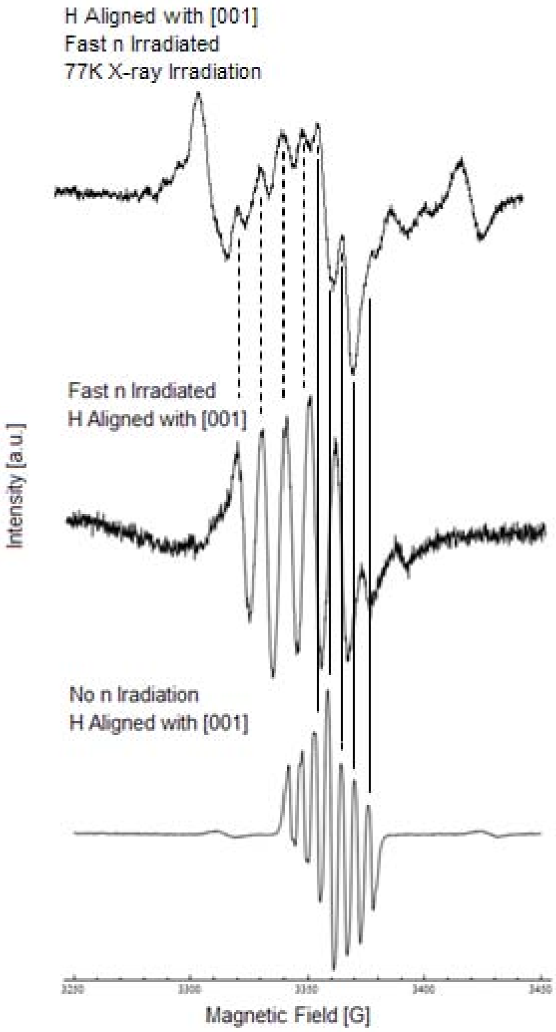

Figure 38. EPR spectra comparison pre and post neutron irradiation for $Li_2B_4O_7$:^{6}Li crystal. EPR spectra for neutron irradiated crystal obtained at 12 K. EPR spectra for pre-neutron irradiated crystal obtained at 77 K. Top spectrum and bottom spectrum were both x-ray irradiated at 77 K. Dashed and solid lines show the position of the combined lines in the top spectrum.

The defects would have the effect of broadening the hyperfine line structure, and the adjacent defect would alter the ligand field near the V_1 center potentially altering the resultant magnetic field at different orientations. In addition, as shown in Figure 38, x-ray irradiation of the neutron irradiated crystal at 77 K populates the as-grown V_1 centers. The as-grown V_1 centers lie roughly between the last few peaks of the perturbed V_1 center, reducing the resolution of the perturbed center by filling the spaces between lines. When the field is then oriented to [001], as shown in Figure 17, greater resolution is regained because the as-grown center is no longer interfering.

Inspection of Figure 37 shows the last two hyperfine lines for the V_1 center in the as-grown crystal have much greater intensity than the perturbed center in the neutron irradiated crystal. At lower temperature, the last two lines in the as-grown crystal show a similar reduction in magnitude. The effect is likely due to the low temperature of the EPR spectra for the neutron irradiated crystals chosen to minimize the broad singlet previously ascribed to Li clusters.

5.2 Secondary Goal: Thermal Stability of Neutron Induced Defects

Considering the TL studies in conjunction with the EPR spectra of the neutron irradiated crystals suggests that neutron irradiation induces defects with unique thermal stability, and yields some probable explanations for the species evident in the TL glow curves. Figure 39 shows a comparison of the TL bulk glow curves of $Li_2B_4O_7{:}^6Li$ pre-neutron irradiation and after thermal neutron irradiation. Note the relative increase in the 250 ºC peak and the appearance of a peak at 350 ºC. The 350 ºC peak is also prominent in the thermal neutron irradiated $Li_2B_4O_7{:}^{10}B$ crystal, as shown in Figure 22. Since the EPR spectrum of this crystal contained only the Li clusters feature, the TL peak at 350 ºC is likely due to annealing of charges trapped at Li clusters. Also, the 250 ºC peak is likely due to Li vacancies adjacent to other defects induced by consumption of ^6Li in neutron reactions, and other defects produced nearby by high energy reaction products.

Although the conclusions are not definitive, the TL glow peak for Li clusters might be a strong indication of neutron interaction in the crystals.

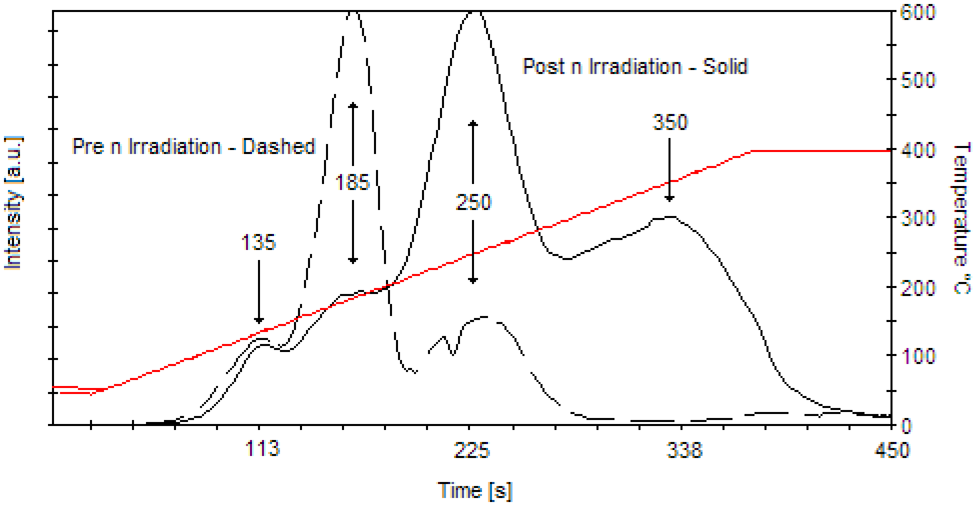

(Post n Irradiation Intensity is 10 X the Pre n Irradiation Intensity)

Figure 39. TL bulk glow curve comparison of $Li_2B_4O_7$:^{6}Li pre- and post-n irradiation, with thermal n interaction density of 10^{15} cm^{-3}.

Table 3. TL Glow Peak Comparison $Li_2B_4O_7$:^{6}Li and $Li_2B_4O_7$:^{10}B

n Energy	Inter. Density	Glow Peaks ºC	Peak Ratio
^{6}Li N/A	N/A	135, 185, 250	1: 4.5: 1.2
Thermal	10^{15} cm^{-3}	135, 185, 250,350	1: 2.0: 6 : 3
Fast	10^{15} cm^{-3}	135,150,185,200,225,250	1:4:3.6:4.8:3.6:4
^{10} B N/A	N/A	185, 250	1 : 11
Thermal	10^{17} cm^{-3}	185, 250,350,400	1 : 0.7:1.7:5

The glow peaks between 150 and 225 ºC are likely due to interstitial defects due to knock-on damage. Knock-on related defects are the only defects not yet identified as corresponding to a TL peak, and the interstitial defects seen in the neutron irradiated $Li_2B_4O_7$:Ag crystal show the same range of stability. The temperature range is the same as the observed TL glow peak in the $Li_2B_4O_7$:Ag neutron irradiated crystal presumed to be from interstitial defects. It is difficult to make a direct comparison because Ag is a very strongly luminescent dopant, and it dominates other defect emissions. A wavelength differentiated TL study would be helpful in identifying the underlying species in the $Li_2B_4O_7$:Ag bulk glow curve, and facilitate comparison to other glow curves. Table 3 shows the peak by peak comparison of the TL glow peaks in the undoped crystals.

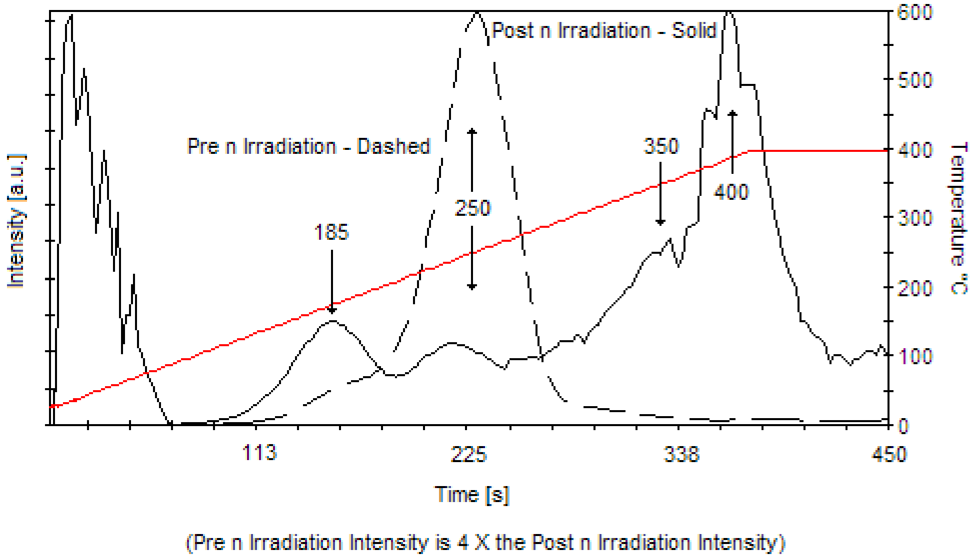

Figure 40. TL bulk glow curve comparison of $Li_2B_4O_7$:^{10}B pre and post n irradiation, thermal n interaction density of 10^{17} cm^{-3}.

Using the method of approximating the thermal activation energy introduced by Randall and Wilkins, the thermal activation energy is approximated by $E \approx 25kT$. Where k is the Boltzmann constant and T is the TL peak temperature (Randall and Wilkins, 1945). The thermal activation energy is the energy at which recombination will be maximized, or peak(s) in the TL bulk glow curves. Table 4 shows the activation energy associated with each TL glow curve peak

Table 4. TL Activation Energies

TL Peak Temperature [K]	Activation Energy [eV]
135	0.29
150	0.32
185	0.40
200	0.43
225	0.48
250	0.54
350	0.75
400	0.86

5.3 Tertiary Goal: Ag Doped $L_2B_4O_7$

The as-grown $Li_2B_4O_7$:Ag crystal shows two Ag^{2+} hole traps and an Ag neutral electron trap. The two doublets centered at 2960 G and 3010 G are Ag^{2+} hole traps, while the 16 peak structure centered at 3380 G is the Ag neutral electron trap. The doublet at 3010 G is formed by a 1/2 spin state unpaired electron interacting with the 1/2 spin state Ag nucleus for a total four energy states or two hyperfine lines. The two isotopes of Ag do not have sufficiently different nuclear magnetic moments be resolved at the low field end. The resolution can be seen in the ENDOR spectrum discussion above. Furthermore, the doublet is on the low field side of the free electron g value indicating it is a trapped hole, Ag^{2+}. The doublet centered at 2960 G is also an Ag^{2+} doublet. In this case, the center is perturbed by some nearby defect. The perturbation is significant enough to completely separate the doublet from the unperturbed spectrum, and slightly change the spacing between peaks. Candidates, seen in Table 2, for the perturbation may be another Ag ion substituting a nearest neighbor Li, or a Na, or Mn ion in the same role. Still another option is an oxygen vacancy in the near vicinity of the Ag^{2+} site. Figure 27 suggests an either/or relationship between the O vacancy F center and the perturbed Ag^{2+} center. When the F center is populated the perturbed Ag^{2+} center is not, and when the F center anneals, the perturbed Ag^{2+} center populates. An electron trapped at a nearby O vacancy may produce a sufficient distortion to the ligand field that holes are unable to trap in the perturbed Ag^{2+} site. As those trapped electrons anneal changes in the ligand field allow trapping of holes on the perturbed Ag^{2+} site, but ligand field perturbation due to the O vacancy remains near the Ag^{2+} site.

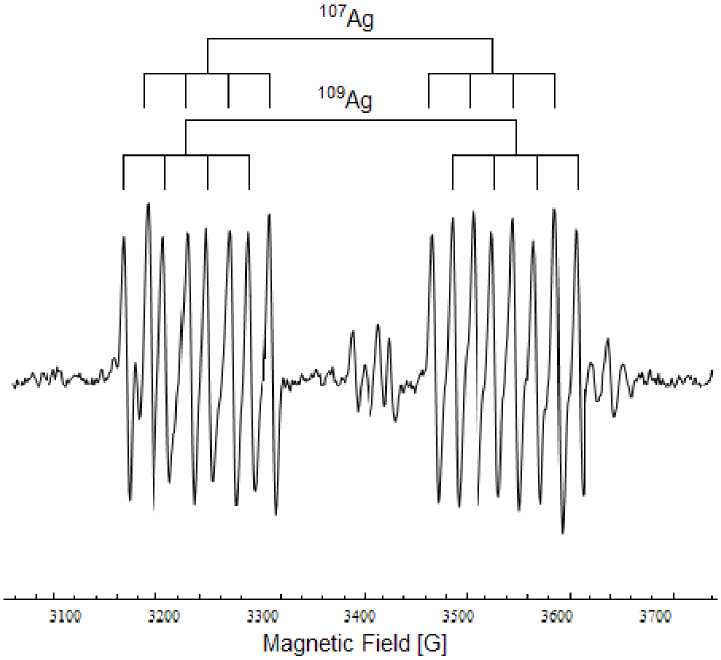

Figure 41. EPR spectrum of $Li_2B_4O_7$:Ag the magnetic field is aligned with the [001]. The spectrum was taken at 30 K. The crystal was x-ray irradiated at room temperature to populate charge traps. The stick diagram shows the resolved isotopes of Ag.

The stick diagram above Figure 41 indicates the relative location of the two isotopes of silver in the 16 peak hyperfine structure centered at 3380 G. At these higher field values, the difference in the nuclear magnetic moments of the two Ag isotopes is sufficient to create resolvable separation. The structure consists of a 1/2 spin unpaired nucleus interacting with a Ag nucleus, spin 1/2 for four energy states, additionally interacting with a nearby 3/2 spin state nucleus for a total of 16 possible energy states, or eight peaks per isotope. Each of the two eight peak spectra are centered at the same magnetic field value, and the difference in separation in the hyperfine spectra is due to the difference in the isotopes nuclear magnetic moment. The ^{107}Ag accounts for every other peak starting at the far right and left sides of the 16 peak structure and working in. ^{109}Ag is accounts for every other peak starting at the inside two peak and working out in both directions. The two ^{107}Ag quartets are centered at 3214 G and 3532 G for a separation of 318 G. The two ^{109}Ag quartets are centered at 3234 G and 3511 G for a separation of 277 G. The ratio of these two separations is 1.148 which compares favorably to the ratio of the two isotopic nuclear g values $\frac{-0.261743}{-0.227249}=1.151$, again indicating the two Ag isotopes.

The thermal stability of the as-grown defects is best determined by comparing the full as-grown pulsed anneal study with the limited pulsed anneal of the neutron irradiated sample. Figure 27 shows clearly that the Li vacancy V_1 center is the most unstable trap. The region from 90 K to 373 K shows the O vacancy F center electron trap annealing while the Ag neutral electron trap is populating. This indicates that the electron trapped at the O vacancy becomes mobile and re-traps at an available Ag neutral site or recombines at an Ag^{2+} site. The O vacancy anneals over a long temperature range. There are crystallographically four different O sites in the crystal. Vacancies at the separate O sites may not have the same thermal stability. This observation was also made by Matkovskii in $Li_2B_4O_7$ crystals (Matkovski, et al. 1994, 374). The perturbed Ag^{2+} site is likely the next trap to anneal. Figure 42 shows the anneal of $Li_2B_4O_7$:Ag crystal x-ray irradiated at room temperature. The perturbed Ag^{2+} center begins to anneal at 343 K; just slightly before the Ag^{2+} center at 348 K. The error bars on this figure are estimates of the error. From 373 K to 473 K, both Ag^{2+} centers anneal at the same rate. It is likely that at 343 K, the hole trapped at the perturbed Ag^{2+} center becomes mobile and begins to recombine at the electron trap sites. When the temperature reaches 373 K, the electron trapped at the Ag neutral center becomes mobile, and recombines at both Ag^{2+} sites, and potentially with mobile holes still annealing from the perturbed Ag^{2+} center. The limited pulsed anneal of the neutron irradiated $Li_2B_4O_7$:Ag crystal suggests that it is trapped electrons that become mobile at 373 K and not holes, because the neutron induced electron traps do not anneal until at least 423 K. A mobile hole will have no preference which trapped electron it recombines with, therefore some of the neutron induced electron traps would anneal if holes were mobile in the crystal. The correspondence between the decrease in the Ag related centers in the PA study and the peaking of the glow curve from the TL study, as in Figure 42, indicates recombination of the as-grown Ag related defects are responsible for the TL emission at 430 K.

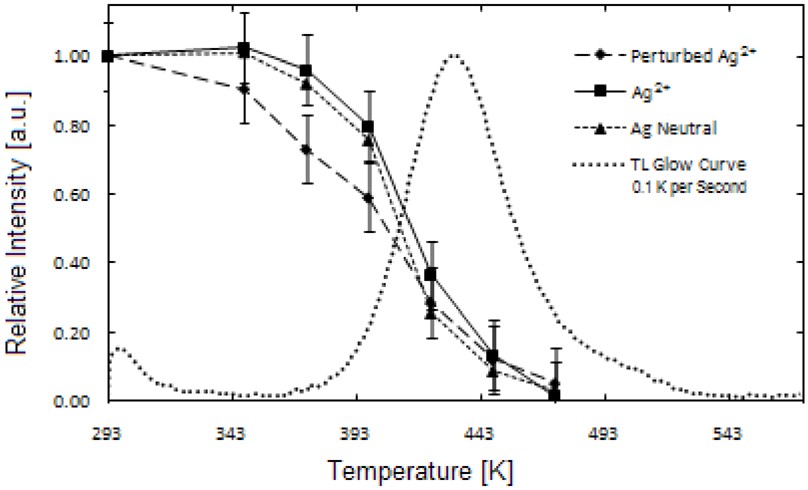

Figure 42. Comparison PA and TL for $Li_2B_4O_7$:Ag above room temperature. The TL glow curve was produced with a heating rate of 0.1 K per second. Error is an estimate. Dr. Larry Halliburton produced the TL glow curve with the assistance of Madhav Krishna Murari (University of Cincinnati, Department of Geology).

Figure 43 shows from bottom to top a comparison of the Ag neutral region of the EPR spectrum from pre-neutron irradiation to post-neutron irradiation to post neutron irradiation with a 20 minute 423 K anneal. Note in the top spectrum there are three separate structures. The sharp single peak centered at 3365 G is likely an interstitial neutral O atom. O is the only atom in the crystal that has a significant isotopic abundance of spin 0 nuclei. O is 99.962% spin 0. A spin 0 nucleus is required to form a sharp single peak. The four-peak structure is likely due to interstitial neutral Li nuclei, since the four peak structure requires a 3/2 spin nucleus. The only other 3/2 spin nucleus in the crystal is ^{11}B, which being a smaller nucleus would likely drift back to a lattice location. If nuclear reactions within the crystal, Li + Li reactions, produce B in excess of the stoichiometric ratio, some B may not have a nearby lattice site to return to. However, there is no hyperfine spectrum evident for ^{10}B which is seen in other instances where B is the responsible 3/2 nucleus in the crystal. It is possible for 3/2 spin Na to cause the same structure, but the trace amount of Na in the crystal is not high enough concentration to cause the strong intensity signals.

Table 5. Thermal Stability of Traps in $Li_2B_4O_7$:Ag

Trap Center	Center Origin	Anneal Temperature
Li Vacancy V_1 Center	As-Grown	90 K
O Vacancy F Center	As-Grown	90-373 K
Perturbed Ag^{2+} Center	As-Grown	348 K
Ag Neutral Center	As-Grown	373 K
Ag^{2+} Center	As-Grown	>373 K
O Interstitial	Neutron Irradiation	>423 K
Li Interstitial	Neutron Irradiation	>423 K
Ag Interstitial	Neutron Irradiation	>423 K

The two widely spaced triplets centered at 3395 G appear to be the result of an interstitial Ag atom split by a nearby Ag nucleus. The three peak structure would be due to overlap in the central peak of the last and first peak of the two Ag isotopes. This would also give the 1:2:1 intensity ratio observed. In this scenario, the difference in doublet spacing between the two isotopes would be due to the difference in the nuclear magnetic moments. This is the same scenario described in Figure 41 for the as-grown neutral Ag defect. The ratio of the splitting in the 3395 G centered six peak structure is 1.07. This does not compare favorably with the expected value of 1.15.

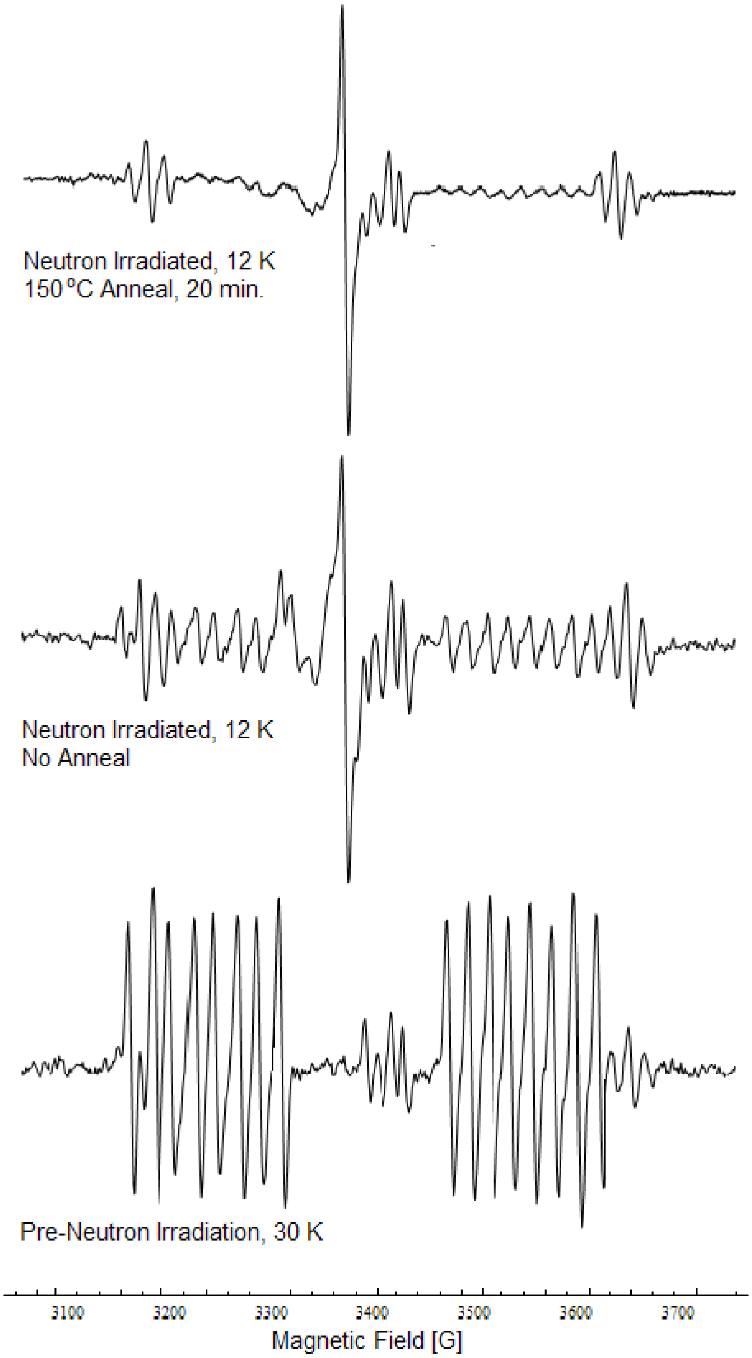

Figure 43. EPR spectra comparison pre- and post-neutron irradiation $Li_2B_4O_7$:Ag. The bottom spectrum is the pre-neutron irradiation spectrum. The center spectrum is the post-neutron irradiation spectrum. The top spectrum is the post-neutron irradiation spectrum after a 150 °C anneal for 20 minutes to suppress the Ag neutral hyperfine structure. The magnetic field is aligned with the [001].

Even more complex Ag-Ag, and Ag-Ag-Ag complexes in which the unpaired charge is able to reorient in the fast limit might give the same shape structure (Weil, Bolton and Wertz 1994, 317). Again the expected ratio of peak splitting would not match the observed 1.07; the expected ratio would increase above 1.15.

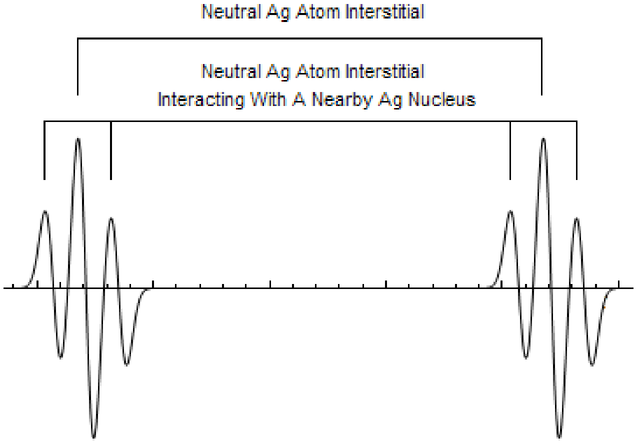

Figure 44. Model of the six peak structure centered at 3395 G in neutron irradiated $Li_2B_4O_7$:Ag. The model is a sum of the first derivative of Gaussian functions. The large central peaks model an isolated interstitial Ag^{1+} ion, while the surrounding doublets model an interstitial Ag^{1+} ion interacting with a nearby Ag nucleus.

Interstitial Ag atoms created in a knock-on process might also be responsible for the six peak structures. In this scenario, an isolated interstitial Ag atom would be responsible for the large central peak in both triplet structure, and an interstitial Ag ion interacting with a nearby Ag nucleus would yield the doublets surrounding both central peaks. Each central peak is split into two peaks, and the resulting doublet must remain centered at the same magnetic field value.

Figure 44 shows the resulting structure and the location of constituent doublet and singlet structures. The present observation suggests a ratio of isolated to interacting interstitials of 2:1. In this scenario, the Ag isotopes are unresolved, and the spacing problems with the previous models are avoided. This model might be validated by careful ENDOR measurements of the central and surrounding peaks of the two triplet structures to resolve the contributions by each Ag isotope.

If the additional structures present in the EPR spectrum of neutron irradiated $Li_2B_4O_7$:Ag are due to knock-on damage creating interstitial defects, sufficient annealing at a reasonably high temperature should repair these defects. After repair, the interstitial atoms would have returned to their lattice positions, and no longer be visible in the EPR spectrum. This effect is seen in $Li_2B_4O_7$:Ag crystals prior to neutron irradiation. Note in the bottom spectrum of Figure 43 the interstitial Li and Ag hyperfine spectra are visible. These hyperfine spectra are low intensity when compared to the middle spectrum of Figure 43 in which the crystal has been neutron irradiated, but the features are present as-grown. These hyperfine structures are not observed in the as-grown crystal after multiple anneals at 400 ºC for 20 minutes. The multiple anneals were executed as a part of the PA studies of the as-grown crystal.

Figure 45 shows a comparison of the TL bulk glow curves of $Li_2B_4O_7$:Ag pre-neutron irradiation and post neutron irradiation. The inset dotted line is a TL bulk glow reported by Kelemen for $Li_2B_4O_7$:Ag irradiated with β^- radiation. The correspondence between the sets of data is remarkable. β^- radiation is expected to cause knock-on type defects like the ones proposed for the neutron irradiated $Li_2B_4O_7$:Ag crystals. Fast neutrons have the potential to cause knock on damage, and the high energy charged particle emission from the ^{10}B,n and ^{6}Li,n reactions could certainly cause knock-on damage.

Skvortsova concurs with the knock on damage mechanism based on optical absorption measurements on neutron irradiated $Li_2B_4O_7$ crystals (Skvortsova 2000, 287). Knock-on damage would not, however, cause concentrations of Li beyond the stoichiometric ratio. This increased Li is seen in all crystals, and is a proposed thermal neutron induced defect. In addition to TL correspondence between neutron and electron irradiated $Li_2B_4O_7$:Ag crystals, optical absorption measurements by Kelemen also suggest that knock-on damage causes multi-Ag atom complexes in electron irradiated crystals (Kelemen et al. 2007, 1533).

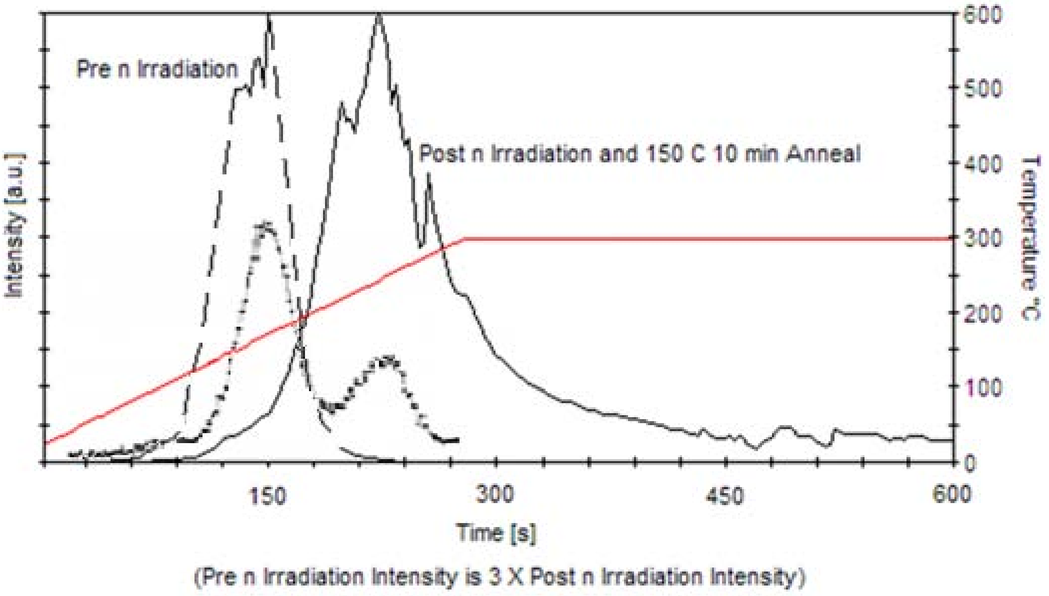

Figure 45. TL bulk glow curve comparison of $Li_2B_4O_7$:Ag pre and post n irradiation, thermal neutron interaction density 10^{15} cm^{-3}. The pre-neutron irradiation glow curve is dashed. The post neutron irradiation glow curve is solid. Prior to obtaining the post neutron irradiation glow curve, the crystal was annealed at 150 °C for 20 minutes to facilitate EPR spectroscopy. The inset dotted line is the TL bulk glow curve of $Li_2B_4O_7$:Ag after β^- irradiation. The dotted curve was adapted from the source (Kelemen, Holovey and Ignatovych 2008, 377).

5.4 Fourth Goal: Positron Annihilation

The intensity in positron annihilation gamma radiations emitted from $Li_2B_4O_7$:^{6}Li compared to other crystal after neutron activation indicates the source of positron annihilation radiation must be dependent on either ^{6}Li or the ^{3}H reaction product of the ^{6}Li,n reaction. The measureable increase in positron annihilation radiation for the same crystal in the first few minutes after neutron activation in the AFIT thermal pile confirms this dependence. Furthermore, the short half-life observed for the positron emitting isotope subsequent to the neutron irradiation in the AFIT thermal pile suggests a half-life less than 25 minutes, but long enough to allow for the time required to move the sample form the pile to the HPGe detector in bldg. 470 (~2 min.). The ^{6}Li(^{7}Li,2n)^{11}C reaction fulfills these requirements. The positive Q value suggests energetic feasibility, and the ^{11}C reaction product has a 20.39 minute half life.

The ^{6}Li(^{7}Li,2n)^{11}C reaction has been observed by bombarding Li targets with Li ions. Berkowitz produced the reaction using 2.6 and 3.6 MeV bombarding particles (Berkowitz, et al. 1962, 251). One obstacle to the formation of ^{11}C in this reaction is the 2.4 MeV Coulomb barrier suggested by Kibler for ^{6}Li + ^{7}Li reactions (Kibler 1967, 1111). The ^{7}Li particle ejected from the ^{10}B(n,α)^{7}Li reaction is not energetic enough to surmount this barrier. Quantum mechanical tunneling may be responsible for surmounting the energy barrier. Lastly, the observed ^{6}Li + ^{7}Li cross-sections observed by Kibler for higher energy reactions producing ^{10,11,12}B and ^{9}Be are in the range of 1 to 10 µb (Kibler 1967, 1115). Larger reaction cross-sections would be needed to produce the observed intensity of positron annihilation radiation from the relatively small flux in the AFIT thermal pile, but Kibler's experiments were conducted at much higher energies. If the reaction cross-section has a 1/V character, similar to thermal neutron induced fission cross-sections, this may not be an obstacle.

Figure 46 shows the possible reaction pathways for the ^{6}Li + ^{7}Li reaction. The various reaction products, reaction Q values, and reaction product half lives and nuclear spins are displayed. The bottom image in the same figure shows the gamma ray spectrum obtained by Bertkowitz while he studied the ^{6}Li + ^{7}Li reaction. Note that ^{11}C was identified by the presence of the 1.99 MeV gamma ray resulting from relaxation of ^{11}C from a nuclear excited state to the ground state (Brookhaven National Laboratory 2006). ^{11}C is produced in a nuclear excited state in ^{6}Li + ^{7}Li reaction (Berkowitz, et al. 1962, 251). Detection of this or other nuclear relaxation gamma radiation may be a more efficient method of detecting neutron interaction in $Li_2B_4O_7$ than detecting 511 keV gamma rays. Furthermore, inspection of the top table in the figure shows that the only detectable gamma ray from all of the possible nuclear reaction pathways of ^{6}Li + ^{7}Li is the 511 keV positron annihilation gamma ray. All of the nuclear excited states would have decayed long before the crystal was able to be moved from the OSURR or the AFIT thermal pile to the HPGe detector. With the exception of ^{11}C, all of the radioactive reaction products would have either long since decayed before being detected, or half lives are too long to be detected in this experiment. Neutrons born at high energies will likely exit the crystal, and those born at thermal energies will likely exit the crystal or be absorbed by ^{10}B or ^{6}Li prior to decay.

In addition to investigating the ^{6}Li + ^{7}Li reaction, Berkowitz also investigated the ^{6}Li + ^{6}Li and ^{7}Li + ^{7}Li reactions. The ^{6}Li + ^{6}Li reaction is not probable in $Li_2B_4O_7$, because ^{6}Li is not produced in the ^{10}B,n reaction. However, the ^{7}Li + ^{7}Li reaction should be expected if the ^{6}Li + ^{7}Li reaction is possible. Furthermore, in crystals with natural abundance of ^{6}Li, the ^{7}Li + ^{7}Li reaction should be favored. Figure 47 is a mirror of Figure 46, but for the ^{7}Li + ^{7}Li reaction pathways. Note there are no reaction products of ^{7}Li + ^{7}Li that are detectable in the present experiment. ^{11}C is not a reaction product for the ^{7}Li + ^{7}Li reaction. Particular attention should be paid in future EPR studies of neutron irradiated Li2B4O7 to determine if Li + Li reaction products or reaction product daughter nuclei are present in the hyperfine spectrum.

Reaction	Q Value[MeV]	Product Decay	Half Life or Nuclear Spin	Product Decay	Half Life or Nuclear Spin
^{6}Li(^{7}Li,^{5}He)^{8}Be	12.6675	^{8}Be: α	0.07 fs	^{5}He: n,α	7.6*10^{-22} s
^{6}Li(^{7}Li,α)^{9}Be	15.2198	^{9}Be: Stable	3/2$^-$	^{4}He: Stable	0$^+$
^{6}Li(^{7}Li, ^{3}He)^{10}Be	4.25138	^{10}Be: β$^-$	1.6*10^6 y	^{3}He: Stable	1/2$^+$
^{6}Li(^{7}Li,^{3}H)^{10}B	1.99155	^{10}B: Stable	3$^+$	^{3}H: β$^-$	12.3 y
^{6}Li(^{7}Li,^{2}H)^{11}B	7.1884	^{11}B: Stable	3/2$^-$	^{2}H: Stable	1$^+$
^{6}Li(^{7}Li,^{1}H)^{12}B	8.33322	^{12}B: β$^-$	20.4 ms	^{1}H: Stable	1/2$^+$
^{6}Li(^{7}Li,2n)^{11}C	**2.19928**	**^{11}C: β$^+$**	**20.4 m**	n: β$^-$	10 m
^{6}Li(^{7}Li,n)^{12}C	20.9206	^{12}C: Stable	0$^+$	n: β$^-$	10 m
^{6}Li(^{7}Li,*)^{13}C	25.8669	^{13}C: Stable	1/2$^-$		
Decay Reaction	Half Life	Product Decay	Half Life or Nuclear Spin	Long Lived Isotopes	Nuclear Spin
n(β$^-$)^{1}H	10 m	^{1}H: Stable	1/2$^+$	^{3}H	1/2$^-$
^{3}H(β$^-$)^{3}He	12.30 y	^{3}He: Stable	1/2$^+$	^{10}Be	0$^+$
^{10}Be(β$^-$)^{10}B	1.6*10^6 y	^{10}B: Stable	3$^+$		
^{12}B(β$^-$)^{12}C	20.4 ms	^{12}C: Stable	0$^+$		
^{11}C(β$^+$)^{11}B	20.4 m	^{11}B: Stable	3/2$^-$		

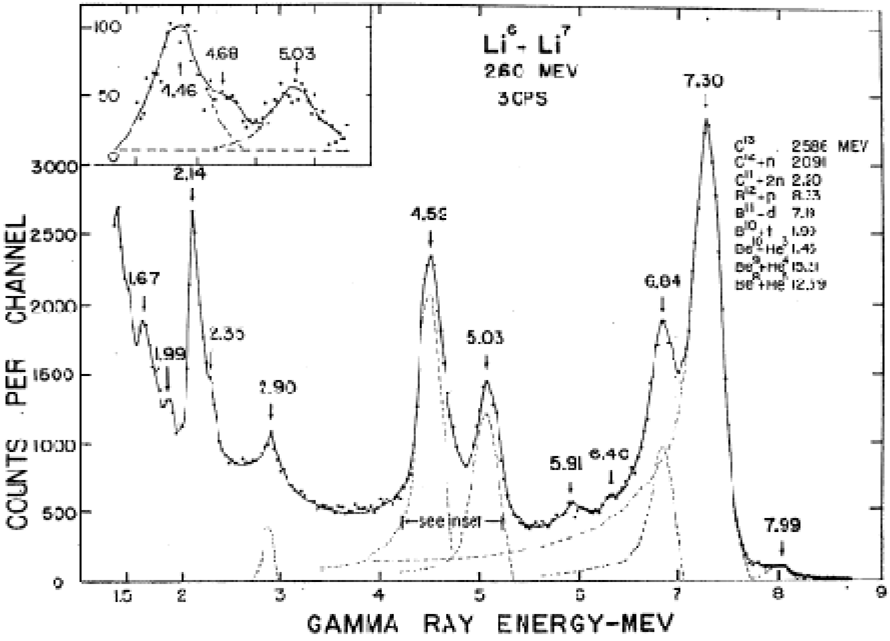

Figure 46. ^{6}Li + ^{7}Li reaction products. The top table shows the possible reaction products, reaction Q values, and reaction product stability and nuclear spin. The bottom figure shows the gamma ray spectrum observed by Berkowitz for the ^{6}Li + ^{7}Li reaction (Berkowitz, et al. 1962, 250).

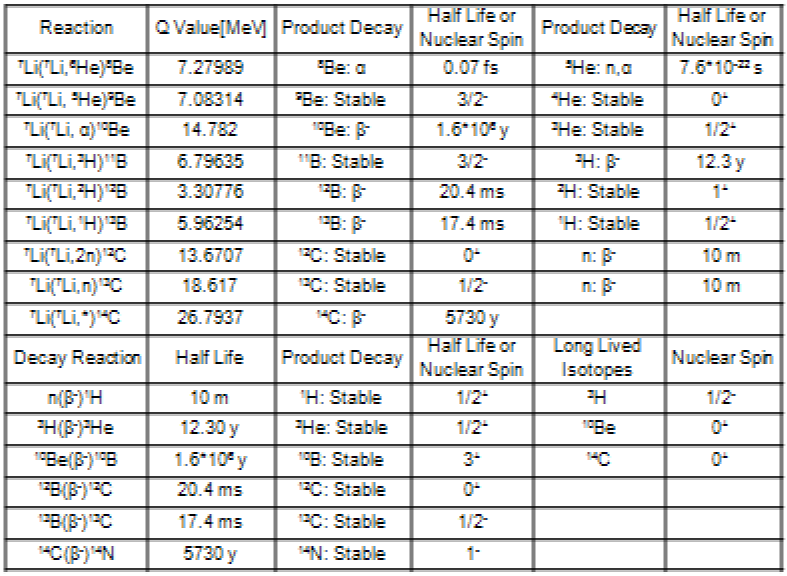

Reaction	Q Value[MeV]	Product Decay	Half Life or Nuclear Spin	Product Decay	Half Life or Nuclear Spin
$^{7}Li(^{7}Li,^{6}He)^{8}Be$	7.27989	^{8}Be: α	0.07 fs	^{5}He: n,α	$7.6*10^{-22}$ s
$^{7}Li(^{7}Li,^{5}He)^{9}Be$	7.08314	^{9}Be: Stable	$3/2^{-}$	^{4}He: Stable	0^{+}
$^{7}Li(^{7}Li,α)^{10}Be$	14.782	^{10}Be: $β^{-}$	$1.6*10^{6}$ y	^{3}He: Stable	$1/2^{+}$
$^{7}Li(^{7}Li,^{3}H)^{11}B$	6.79635	^{11}B: Stable	$3/2^{-}$	^{3}H: $β^{-}$	12.3 y
$^{7}Li(^{7}Li,^{2}H)^{12}B$	3.30776	^{12}B: $β^{-}$	20.4 ms	^{2}H: Stable	1^{+}
$^{7}Li(^{7}Li,^{1}H)^{13}B$	5.96254	^{13}B: $β^{-}$	17.4 ms	^{1}H: Stable	$1/2^{+}$
$^{7}Li(^{7}Li,2n)^{12}C$	13.6707	^{12}C: Stable	0^{+}	n: $β^{-}$	10 m
$^{7}Li(^{7}Li,n)^{13}C$	18.617	^{13}C: Stable	$1/2^{-}$	n: $β^{-}$	10 m
$^{7}Li(^{7}Li,*)^{14}C$	26.7937	^{14}C: $β^{-}$	5730 y		
Decay Reaction	Half Life	Product Decay	Half Life or Nuclear Spin	Long Lived Isotopes	Nuclear Spin
$n(β^{-})^{1}H$	10 m	^{1}H: Stable	$1/2^{+}$	^{3}H	$1/2^{-}$
$^{3}H(β^{-})^{3}He$	12.30 y	^{3}He: Stable	$1/2^{+}$	^{10}Be	0^{+}
$^{10}Be(β^{-})^{10}B$	$1.6*10^{6}$ y	^{10}B: Stable	3^{+}	^{14}C	0^{+}
$^{12}B(β^{-})^{12}C$	20.4 ms	^{12}C: Stable	0^{+}		
$^{13}B(β^{-})^{13}C$	17.4 ms	^{13}C: Stable	$1/2^{-}$		
$^{14}C(β^{-})^{14}N$	5730 y	^{14}N: Stable	1^{-}		

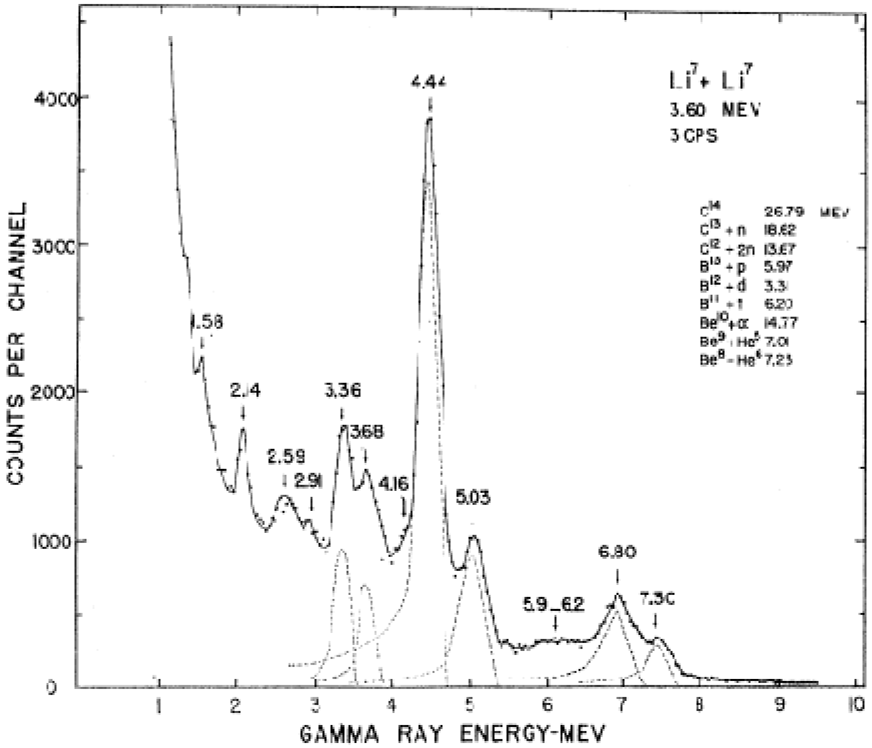

Figure 47. $^{7}Li + ^{7}Li$ reaction products. The top table shows the possible reaction products, reaction Q values, and reaction product stability and nuclear spin. The bottom figure shows the gamma ray spectrum observed by Berkowitz for the $^{7}Li + ^{7}Li$ reaction (Berkowitz, et al. 1962, 250).

VI. Conclusion

6.1 Primary Findings

Neutron irradiation of isotopically enriched $Li_2B_4O_7$ indicates that thermal neutrons and fast neutron produce different point defects within the crystal lattice that are of significantly different thermal stability. The Li vacancy perturbed by a nearby defect observed in the $Li_2B_4O_7$:^{6}Li crystal is present in the crystal as-grown; indicated by a corresponding thermoluminescent peak existing prior to neutron irradiation. However, the relative intensity of the corresponding peak increases significantly after thermal and neutron irradiation which produced more perturbed Li vacancies. Fast neutron fluxes might also be able to cause similar defects through knock on damage. The possible interstitial Li clusters observed in all crystals was not present in the crystals prior to thermal neutron irradiation; there was no intensity at the corresponding themoluminescent peak. If confirmed, Li beyond the stoichiometric ratio forming Li clusters could only be produced by the ^{10}B,n reaction. Furthermore, the thermoluminescent peaks of the perturbed Li vacancy and the Li clusters are significantly separated, and can be readily distinguished.

Electron paramagnetic resonance, electron-nuclear double resonance, pulsed anneal, and thermoluminescent studies demonstrated the nature of and thermal stability of as-grown defects in $Li_2B_4O_7$:Ag. As-grown crystals contain Ag^{2+} and perturbed Ag^{2+} hole traps, as well as neutral Ag electron traps beyond those defects already noted in undoped crystals. The perturbed Ag^{2+} hole trap appears to be the least stable defect, and the as-grown neutral Ag electron traps are less stable than the knock-on related electron traps formed by neutron or possibly electron irradiation. Neutron irradiation of the $Li_2B_4O_7$:Ag crystals produced four types of knock-on related defects, as well as possible Li clusters. The knock-on related defects are suggested to be: isolated O interstitials, isolated Li interstitials, isolated Ag interstitials, and Ag interstitials nearby another

Ag nucleus. All knock-on related interstitial defects trap electrons. The knock-on related interstitial defects are also significantly more stable than the as-grown defects. Lastly, the knock-on related defects are significantly less thermally stable than the Li clusters, and might be used to differentiate thermal and fast neutron fluxes interacting in the Ag doped crystal.

It is suggested that the ^{6}Li(^{7}Li,2n)^{11}C reaction is responsible for the significant positron annihilation presence in all types of $Li_2B_4O_7$ crystals subsequent to neutron irradiation. Observation of the 511 keV gamma rays from the decay of ^{11}C may give a delayed indication of neutron interaction in the crystal. This reaction mechanism has been observed before, but not at the relatively low energies available in the present studies. The reaction of ^{6}Li + ^{7}Li produces multiple different isotopes, and multiple excited states of many of those isotopes. Observation of the relaxation gamma rays from these excited isotopes may give a mechanism to observe neutron interaction in $Li_2B_4O_7$ crystals in real time. In this fashion, $Li_2B_4O_7$ may be able to be utilized as a thin gamma blind conversion layer to other well known detectors.

6.2 Recommendations

The presence of neutron irradiation damage in $Li_2B_4O_7$ crystals should be confirmed by eliminating the possibility that high energy γ radiation is responsible for the observed defects. EPR, ENDOR, PA, TL and optical absorption (OA) studies of γ radiated crystals should be conducted. Irradiation of $Li_2B_4O_7$ crystals in the gamma irradiation facility at the OSURR with follow on defect characterization should be sufficient.

Further EPR, ENDOR, PA, TL and OA studies should be conducted on the neutron irradiated crystals to better understand the identified defects as well as begin to understand the as yet unidentified defects. Specifically, ENDOR study of the knock-on related interstitials in the $Li_2B_4O_7$:Ag crystal should be conducted to confirm the proposed defect models. EPR and ENDOR studies should be conducted on the $Li_2B_4O_7$ crystals subsequent to β^- irradiation to confirm the knock-on type interstitial defect models. Irradiation of crystals in the Dynamitron electron accelerator at Wright State University might suffice for this study. The studies subsequent to β^- irradiation and γ irradiation may also help de-convolve the complex spectra observed after neutron irradiation. If the suggested thermal and fast neutron induced defects can be confirmed, studies should be conducted to determine the lower and upper bounds of sensitivity to these defects in the crystals. This study would determine the feasibility of TL as a mechanism for detection of neutron interaction in the $Li_2B_4O_7$ crystal.

Wave length differentiated TL should be conducted on all crystals to better understand the defects responsible for the bulk TL glow curves. Wavelength differentiated TL would enable the deconvolution of defects annealing at the same temperature, thus producing a single peak in the TL glow curve. A CCD spectrometer would need to be coupled to an existing TLD reader, or an entirely new device constructed for this purpose.

Further study of the possible $^{6}Li(^{7}Li,2n)^{11}C$ reaction subsequent to neutron irradiation of $^{6}Li(^{7}Li,2n)^{11}C$ crystals should be conducted to confirm the reaction mechanism. Gamma ray spectroscopy during neutron irradiation could definitively confirm the reaction mechanism, and perhaps propose alternate ^{6}Li + ^{7}Li reaction pathways useful for detection of thermal neutrons.

Appendix A

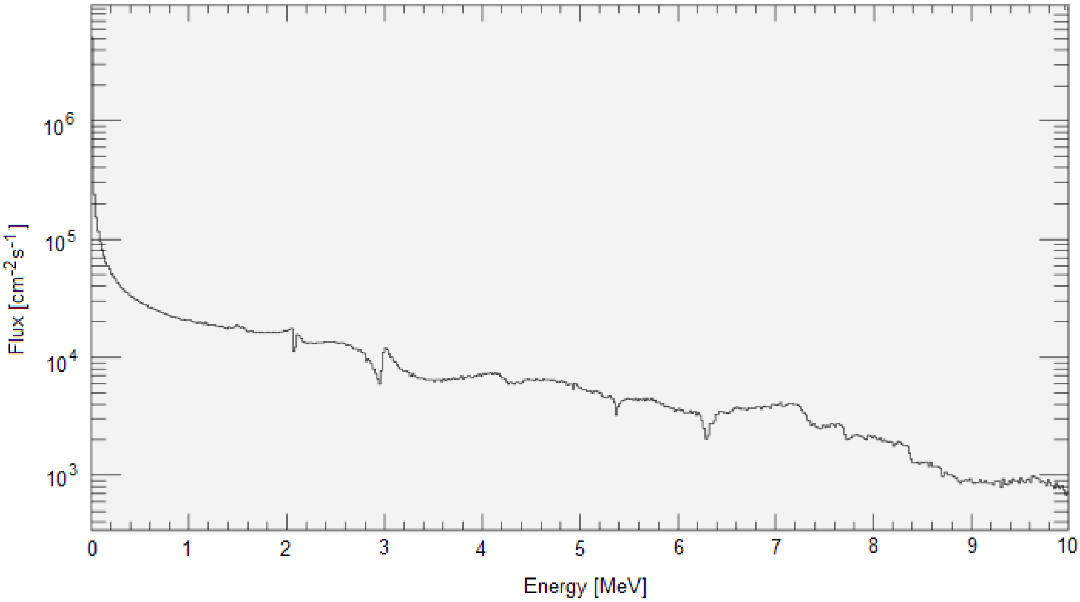

Figure 48. Neutron energy spectrum for the drawer three position in the AFIT subcritical pile.

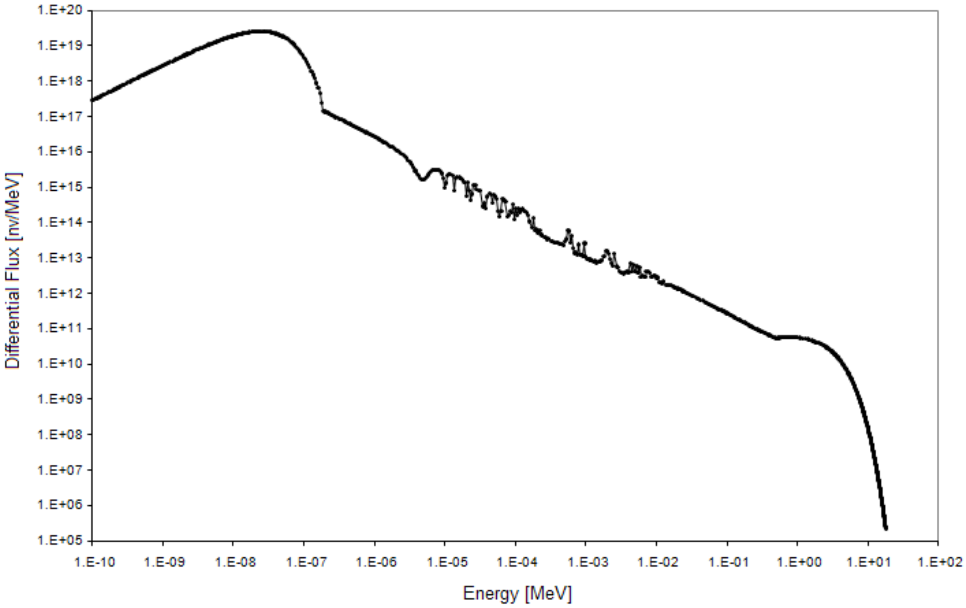

Figure 49. Neutron energy spectrum for the "rabbit tube" position in the OSURR. Data for this image provided by Mr. Joe Talnagi (Talnagi 2010).

Bibliography

Abragam, A., and B. Bleaney. *Electron Paramagnetic Resonance of Transition Ions.* New York: Dover Publications, Inc., 1970.

Adamiv, V.T., Ya.V. Burak, and I.M. Teslyuk. "The Crystal Structure of Li2B4O7 Compound In The Temperature Range 10–290K." *Journal of Alloys and Compounds, 475*, 2009: 869-873.

Berkowitz, E., S. Bashkin, R. R. Carlson, S. A. Coon, and E. Norbeck. "Gamma Radaition from Lithium-Lithium Nuclear Reactions." *Physical Review, 128, 1,* 1962: 247-251.

Brookhaven National Laboratory. *Evaluated Nuclear Data File.* December 15, 2006. http://www.nndc.bnl.gov/exfor/endf00.jsp (accessed January 18, 2011).

Bruker Corporation. *EPR/ENDOR Frequency Table.* Table, Billerica, MA: Bruker Daltonics Inc.

Burak, Ya. V., B. V. Padlyak, and V. M. Shevel. "Neutron Induced Defects in the Lithium Tetraborate Single Crystals." *Radiation Effect & Defects in Solids, vol. 157*, 2002: 1101-1109.

Burak, Ya. V., V. T. Adamiv, I. M. Teslyuk, and V. M. Shevel. "Optical Absorption of Isotopically Enriched Li2B4O7 Crystals Irradiated by Thermal Neutrons." *Radiation Measurements, 38*, 2004: 681-684.

Glascock, Michael D. "Overview of Neutron Activation Analysis." *University of Missouri - Columbia.* 10 6, 2010. http://archaeometry.missouri.edu/naa_overview.html (accessed 12 30, 2010).

Ignatovych, M., V. Holovey, P. Vidoczy, P. Baranyai, A. Kelemen, and O. Chuiko. "Spectrascopy of Cu and Ag Doped Single Crystal and Glassy Lithium Tetraborate: Luminescence, Optical Absorption and ESR Study." *Functional Materials, 12, 2*, 2005: 313-317.

Ignatovych, M., V. Holovey, T. Vidoczy, P. Baranyai, and A. Kelemen. "Phosphors, Spectral Study on Manganese and Silver Doped Lithium Tetraborate." *Radiation Physics and Chemistry, 76*, 2007: 1527-1530.

Kelemen, A., A. Holovey, and M. Ignatovych. "Realtive yields of radioluminescence and Thermoluminescence in Manganese and Silver Doped Lithium Tetraborate Phosphors." *Radaition Measurements, 43*, 2008: 375-378.

Kelemen, A., M. Ignatovuch, V. Holovey, and T. Vido' czyd. "Effect of Irradiation on Photoluminescence and Optical Absorption." *Radiation Physics and Chemistry, 76*, 2007: 1531-1534.

Kibler, K.G. "Differential and Total Cross Sections of Reaction Products from Li6+Li7 between 3.78 and 5.95 MeV." *Physical Review, vol. 155, no. 4*, 1967: 1110-1118.

Krane, Kenneth S. *Introductory Nuclear Physics.* New York: John Wiley & Sons, Inc., 1988.
Lipinski, I. E. "A Correlation Between EPR and Dielectric Studies for LBO Doped with Manganese." *Rev.Adv.Mater.Sci.12*, 2006: 150-153.

Matkovski, A. O., D. Yu. Sugak, Ya. V. Burak, G. I. Malkovichko, and V. G. Grachov. "Radiation Defect Formation in Lithium Tetraborate Single Crystals." *Radiation Effects and Defects in Solids, vol. 132*, 1994: 371-376.

Podgorska, D., Kascmarek, S. M., Drozdowski, W., Wabia. M., Kwasny, M., Warchol, S. and Rizak, V. M. Charging Processes of Mn Ions in $Li_2B_4O_7$:Mn Single Crystal and Glass Samples Under the Influence of γ-Irradiation and Annealing. *Molecular Physics Reports, vol. 39*, 2004: 199-222.

Parrington, Joseph R. *Nuclides and Isotopes 15th Ed.* San Jose: General Electric Co. and KAPL, Inc., 1996.

Randall, J.T. and Wilkins, M. H. F. *Proceedings of the Royal Society of London. Series A, Mathematical and Physical Sciences Vol. 184, No. 999*, 1945: 365-389.

Skvortsova, V., N. Mironova-Ulmane, U. Ulmanis and A. Matkovskii. "Radiation Effects in Li2B4O7." *Nuclear Instrumentation and Methods in Physics REsearch Section B: Beam Interactions with Materials and Atoms, 166-167*, 2000: 284-288.

Swinney, M.W., personal communication.

Swinney, M.W., J.W. McClory, J.C. Petrosky, Shan Yang, A.T. Brant, V.T. Adamiv, Ya. V. Burak, P.A. Dowben, and L.E. Halliburton. "Indentification of Electron and Hole Traps in Lithium Tetraborate Crystals: Oxygen Vacancies and Lithium Vacancies." *Journal of Applied Physics, 107, 113715*, 2010: 1-9.

TUNL Nuclear Data Project. 12 16, 2010. http://www.tunl.duke.edu/nucldata/index.shtml (accessed 1 6, 2010).

Weil, John A., James R. Bolton, and John E. Wertz. *Electron Paramagnetic Resonance Elemental Theory and Practical Applications.* New York: John Wiley & Sons, Inc., 1994.

REPORT DOCUMENTATION PAGE

Form Approved
OMB No. 074-0188

1. REPORT DATE *(DD-MM-YYYY)*

2. REPORT TYPE
Master's Thesis

3. DATES COVERED *(From – To)*

4. TITLE AND SUBTITLE

CHARACTERIZATION OF NEUTRON-INDUCED DEFECTS IN
ISOTOPICALLY ENRICHED LITHIUM TETRABORATE

5a. CONTRACT NUMBER

5b. GRANT NUMBER

5c. PROGRAM ELEMENT NUMBER

6. AUTHOR(S)

Kananen, Brant E., Major, USA

5d. PROJECT NUMBER

5e. TASK NUMBER

5f. WORK UNIT NUMBER

7. PERFORMING ORGANIZATION NAMES(S) AND ADDRESS(S)

Air Force Institute of Technology
Graduate School of Engineering and Management (AFIT/EN)
2950 Hobson Way
WPAFB OH 45433-7765

8. PERFORMING ORGANIZATION REPORT NUMBER

AFIT/GNE/ENP/11-M12

9. SPONSORING/MONITORING AGENCY NAME(S) AND ADDRESS(ES)
Defense Threat Reduction Agency
COL Mark Mattox
1900 Wyoming Blvd SE
Kirtland AFB, NM 87117-5669

10. SPONSOR/MONITOR'S ACRONYM(S)
DTRA/OPS-CSU

11. SPONSOR/MONITOR'S REPORT NUMBER(S)

12. DISTRIBUTION/AVAILABILITY STATEMENT
APPROVED FOR PUBLIC RELEASE; DISTRIBUTION UNLIMITED

13. SUPPLEMENTARY NOTES

14. ABSTRACT
Lithium Tetraborate (LTB) is assessed for use as a material for neutron detection. LTB isotopically enriched in either Li-6 or B-10 provides a medium that efficiently captures and transmutes neutrons into more readily detected forms of material or energy. Neutron detection is desirable to detect elicit movement of special nuclear material or nuclear weapons. Single crystals of LTB, Li-6 or B-10 enriched, were neutron irradiated, and electron paramagnetic resonance was used to detect point defects induced by the neutrons. Multiple defects were noted in the irradiated crystals. Two particular defects, perturbed lithium vacancies and lithium clusters are proposed as induced by thermal neutrons. Parallel experiments on silver doped LTB indicated that fast neutrons induce interstitial defects including interstitial oxygen, lithium, and silver atoms in silver doped crystals. Electron paramagnetic resonance, electron-nuclear double resonance, pulsed anneal, and thermo luminescence studies prior to neutron irradiation concluded that silver doped LTB crystals contain silver point defects that trap both electrons and holes. Pulsed anneal and thermo luminescence studies of all crystal types prior to neutron irradiation suggest neutron induced defects are significantly more stable that as grown defects. Thermo luminescence may be a viable technique to detect neutron interactions in the crystals. Lastly, 511 keV gamma radiation observed after neutron irradiation of all crystals is attributed to positron annihilation in the crystals. The Li-6(Li-7,2n)C-11 reaction is suggested as the responsible mechanism for positron production. The resulting C-11 nucleus radio actively decays via emission of a positron with a half life of 20.39 minutes.

15. SUBJECT TERMS
Lithium Tetraborate, Electron Paramagnetic Resonance, Neutron Detection, Thermo Luminescence

16. SECURITY CLASSIFICATION OF:			**17. LIMITATION OF ABSTRACT**	**18. NUMBER OF PAGES**	**19a. NAME OF RESPONSIBLE PERSON**
a. REPORT	**b. ABSTRACT**	**c. THIS PAGE**			LTC John W. McClory (AFIT/ENP)
U	U	U	UU	97	**19b. TELEPHONE NUMBER** *(Include area code)* 785-3636 x7308

Standard Form 298 (Rev. 8-98)
Prescribed by ANSI Std. Z39-18